Engineering Journal

Smarter.
Stronger.
Steel.

Engineering Journal

American Institute of Steel Construction

Dedicated to the development and improvement of steel construction, through the interchange of ideas, experiences and data.

Subscriptions: subscriptions@aisc.org, 312.670.2400

Archives: Search at **aisc.org/ej**. Article downloads are free for current members and are avaialable for a nominal fee for non-members.

Design of Simple Steel Connections under Fire Temperatures

ELIE G. HANTOUCHE, KARIM K. AL KHATIB, and HAGOP V. JABOTIAN

ABSTRACT

A methodology is developed for designing simple steel connections (shear tab and double angle) subjected to fire. The proposed methodology is based on quantifying the strength and stiffness of steel framed simple connections at elevated temperatures. To achieve this, first, a stiffness-based model that characterizes the rotational stiffness of simple steel connections when subjected to fire temperatures is developed. The model is capable of predicting the behavior of two widely used simple steel connections (shear tab and double angle) when subjected to fire temperatures. It incorporates the connection rotation of key component elements and the nonlinear behavior of both bolts and base materials at elevated temperatures. The model is validated against experimental results available in the literature under steady-state temperature analysis. The model covers all possible limit states and governing failure modes under different loading and temperature conditions. It can be considered a practical tool for designing simple steel connections for professional structural fire engineers in the United States. Step-by-step design examples of simple steel connections in an isolated frame are provided to illustrate the incorporation of the developed stiffness model in a fire design procedure. The presented design procedure accounts for the additional load demand on the connection during fire. This includes the load demand due to thermal expansion and beam sagging.

Keywords: Stiffness-based model, steady-state temperature, fire, simple connections, fire design.

INTRODUCTION

Steel connections play an important role in maintaining the stability and integrity of steel building frames especially when exposed to fire temperatures. Failure of steel connections under fire loading can lead to total structural collapse. This was confirmed through the investigation of many fire disasters (Sunder, 2005) which reported that progressive structural collapse is mainly initiated by connection failure. In fire events, the behavior of steel connections is more complex due to geometrical and material nonlinearities. Almost no structural design guideline can be found that provides an adequate performance of steel connections in fire from a structural perspective. Instead, the available U.S. standards rely on the applied insulation to reduce the exposure of steel connections to fire temperatures, mitigating fire risks to an acceptable level.

Simple steel connections are extensively used in steel structures for their ease of use and low fabrication cost. The two commonly used simple steel connections in the United States are the shear tab and the double-angle connections. They are ideally designed as pin connections that resist shear forces resulting from gravity loads only. However, in fire events, these connections are subjected to higher load demands due to the thermal expansion and sagging of the steel beam, in addition to the degradation of the steel properties at high temperatures. Therefore, it is of paramount importance to find reliable and practical tools that can predict the changes in the stiffness and behavior of these connections at elevated temperatures. That is, understanding the behavior of steel connections in such severe conditions is necessary for the fire design of steel connections to prevent any structural instability.

Characterizing the connection performance and behavior at elevated temperatures forms the basis for fire design of steel connections. Experimental research programs have been conducted in the past few years to investigate the robustness of simple steel connections in fire (Hu and Engelhardt, 2012; University of Sheffield, 2007; Wald et al., 2006; Wang et al., 2011). Experimental work was conducted by Wald et al. (2006) to examine the global structural behavior of an eight-story composite steel–concrete building under fire. Two types of simple steel connections—flexible end plate and shear tab connections—were tested. The results showed that the structure did not lose its global stability when subjected to fire. Note that the beams and the connections were not protected against fire temperatures. Similar findings were observed in the experimental program conducted by

Elie G. Hantouche, Associate Professor, Department of Civil and Environmental Engineering, American University of Beirut, Beirut, Lebanon. Email: eh12@aub.edu.lb (corresponding)

Karim K. Al Khatib, Graduate Student, Department of Civil and Environmental Engineering, American University of Beirut, Beirut, Lebanon. Email: kka05@mail.aub.edu

Hagop V. Jabotian, Graduate Student, Department of Civil and Environmental Engineering, American University of Beirut, Beirut, Lebanon. Email: hvj00@mail.aub.edu

Wang et al. (2011) that investigated the robustness of different types of steel connections in restrained steel frames subjected to fire. The results showed that simple connections, specifically double angle, performed well in fire by providing high ductility and rotational capacity. The fire resilience of the double-angle connection, when subjected to thermally induced loading, was also experimentally tested by Pakala et al. (2012). Owing to its inherent rotational ductility, the double-angle connection was able to survive the fire test without experiencing any failure.

Numerical investigations were also conducted previously to study the behavior of simple steel connections under fire (Garlock and Selamet, 2010; Hantouche et al., 2016; Wuwer et al., 2012; Selamet and Garlock, 2010). Selamet and Garlock (2010) proposed, based on finite element (FE) studies, simple modifications on the shear tab connection detailing that improves the performance of such connections during fire scenarios. Furthermore, Hantouche et al. (2016) performed FE simulations to identify the key parameters affecting the behavior of double-angle connections at elevated temperatures. The results showed that the main factors affecting the connection behavior are load ratio, initial cooling temperature, location of the double angle, and gap distance. It was also concluded that double-angle connections have better performance at elevated temperatures when compared with shear tab connections. Seif et al. (2013; 2016) conducted an extensive numerical investigation to examine the effect of elevated temperature on simple shear tab connections. It was found that the change in failure modes is not only caused by the degradation of the steel material when subjected to fire, but also on the deformations that can be accommodated prior to fracture due to restraint thermal expansion or contraction. Over the past few years, several studies were conducted to develop mechanical (stiffness) models capable of predicting the load-deformation response of steel connections at ambient and elevated temperatures. As an example, Yu et al. (2009a; 2009b; 2009c) developed a mechanical (stiffness) model based on numerical and experimental studies for shear tab and double-angle connections under fire temperatures.

Previous studies showed that the survival of unprotected steel beams depends on the ability of the steel connections to withstand the additional fire loadings, especially at late stages of fire. Very limited research, however, focused on developing a design-oriented guideline that quantifies the load demand on simple steel connections under transient-state conditions of fire. To address this shortcoming, this study combines the characterization of simple steel connection behavior at elevated temperatures with fire design procedures. First, the study proposes a stiffness-based model that can be considered as a practical and simple tool to be used by structural fire designers. The proposed model is capable of predicting the overall rotational stiffness and strength of shear tab and double-angle connections under steady-state temperature conditions. The developed stiffness model is used in a step-by-step connection design procedure to predict the moment demand caused by the beam sagging in fire. Moreover, the additional fire loadings are incorporated in the calculation of stresses to reach a robust fire design of simple steel connections to withstand the fire temperatures.

STIFFNESS-BASED MODEL

A stiffness-based model is developed to predict the force-rotation characteristics of shear tab and double-angle connections at elevated temperatures. The proposed stiffness model consists of a series of linear and nonlinear springs that are combined together to predict the rotational stiffness and capacity of the whole connection. The following equations are based on ambient temperature formulations while considering the material properties as temperature-dependent. The retention factors incorporated in the stiffness-based model for steel materials, bolts, and welds are proposed by Lee et al. (2013), Hu et al. (2007), and Eurocode 3 (CEN, 2005a), respectively.

Joint Component Stiffness Coefficients

The stiffness coefficients of the springs that are incorporated in the proposed stiffness model are defined based on equations available in the literature. The stiffness components for each bolt row are presented below.

Web Angle in Bending

The stiffness of the web angle in bending, k_{ab}, is determined using this equation from Eurocode 3 (CEN, 2005b), Section 6.3.2:

$$k_{ab} = K_E E \frac{0.9 l_{eff,ab} t^3}{m^3} \tag{1}$$

where K_E is the temperature-dependent retention factor for the stiffness of the base materials; E is the elastic modulus of the steel material at ambient temperature; $l_{eff,ab}$ is the effective length of the double angles in bending in each bolt-row, using the same approach in calculating the effective length of the equivalent T-stub in bending as proposed by Eurocode 3 (CEN, 2005b); t is the thickness (of the angle leg); and m is the distance from the center of the bolt to the fillet of the angle leg.

Bolt in Tension

The stiffness of the bolt in tension, k_{bt}, can be calculated as proposed by Eurocode 3 (CEN, 2005b), Section 6.3.2:

$$k_{bt} = K_E E \frac{1.6 A_b}{L_b} \tag{2}$$

where A_b is the effective area of the bolt shank in tension, and L_b is the elongation length of the bolt shank, which consists of the grip length (thickness of material and washers) of the bolt and half the sum of the height of the bolt head and the height of the nut.

Beam Web/Angle Leg in Bearing

The stiffness of beam web or angle leg in bearing, k_{pb}, is taken from Eurocode 3 (CEN, 2005b), Section 6.3.2:

$$k_{pb} = 12 n_b k_b k_t d_b K_{ut} F_{ut} \qquad (3)$$

where n_b is the number of bolt columns, while k_b and k_t are defined as:

$$k_b = \min\left\{0.25\frac{e_b}{d_b} + 0.5; \; 0.25\frac{p_b}{d_b} + 0.375; \; 1.25\right\} \qquad (4)$$

$$k_t = \min\left\{1.5\frac{t}{d_{M16}}; \; 2.5\right\} \qquad (5)$$

where e_b is the distance from the bolt to the free edge of the plate in the direction of the load transfer, d_b is the diameter of the bolt shank, p_b is the spacing of the bolt in the direction of the load transfer, and d_{M16} is the diameter of an M16 bolt. K_{ut} is the temperature-dependent retention factor for the ultimate strength of the base material, and F_{ut} is the ultimate strength of the steel base material at ambient temperature.

Shear Tab Plate in Bearing

The bearing stiffness of the shear tab plate, k_{tb}, is computed using this equation from Yu et al. (2009b):

$$k_{tb} = \Omega t K_{yt} F_{yt} \left(\frac{d_b}{25.4}\right)^{0.8} \qquad (6)$$

where Ω is a temperature-dependent parameter defined in Yu et al. (2009b), K_{yt} is the temperature-dependent retention factor for the yield strength of the steel base material, and F_{yt} is the material yield strength of the steel base material at ambient temperature.

Bolt in Shear

The shear bolt stiffness, k_{bs}, is defined in Wuwer et al. (2012) as:

$$k_{bs} = \frac{8 n_b d_b^2 K_{bt} F_{ub}}{d_{M16}} \qquad (7)$$

where K_{bt} is the temperature-dependent retention factor for the bolt strength, and F_{ub} is the ultimate strength of the bolt material at ambient temperature.

Beam Flange in Contact with Column

The stiffness of the beam flange in contact with the column, k_{bcc}, is modeled using the axial stiffness of a beam element:

$$k_{bcc} = \frac{K_E E A_f}{L} \qquad (8)$$

where A_f represents the effective area of the beam lower web and the beam bottom flange in contact with the face of the column, and L is the length of the beam. This spring is activated only when the beam comes in contact with the column after a specific degree of connection rotation.

Equivalent Stiffness of Simple Connections

The equivalent stiffness of the shear tab and double angle connections can be defined by assembling the stiffness of each component as presented in Figures 1(a) and 1(b), respectively. As seen in Figures 1(a) and 1(b), the equivalent stiffness of each of the shear tab and double-angle connections is presented by a group of bolt-rows composed of many component springs. The stiffness component of a single bolt-row of the shear tab connection can be expressed by:

$$\frac{1}{k_{bolt\,row}} = \frac{1}{k_{tb}} + \frac{1}{k_{bs}} + \frac{1}{k_{pb,beam}} \qquad (9)$$

The stiffness component of a single bolt-row of the double angle connection can be expressed by:

$$\frac{1}{k_{bolt\,row}} = \frac{1}{k_{bt}} + \frac{1}{k_{ab}} + \frac{1}{k_{beam\text{-}angle\,lapjoint}} \qquad (10)$$

where $k_{beam\text{-}angle\,lapjoint}$ represents the stiffness of a double-lap joint and is calculated by the following equation:

$$\frac{1}{k_{beam\text{-}angle\,lapjoint}} = \frac{2}{\left(\dfrac{1}{k_{pb,angle}} + \dfrac{1}{k_{bs}}\right)} + \frac{1}{k_{pb,beam}} \qquad (11)$$

Rotational Stiffness of Simple Connections

To predict the connection rotation, the equivalent rotational stiffness of the connection, k_r, needs to be calculated and is defined as:

$$k_r = k_{bolt\,row} h^2 \qquad (12)$$

where h is the distance between the end components connecting the shear tab plate or double-angle leg to the column, as shown in Figures 1(a) and 1(b), respectively. The connection rotation, θ_c, of the shear tab or double-angle connections can be calculated as follows:

$$\theta_c = \frac{M}{k_r} \qquad (13)$$
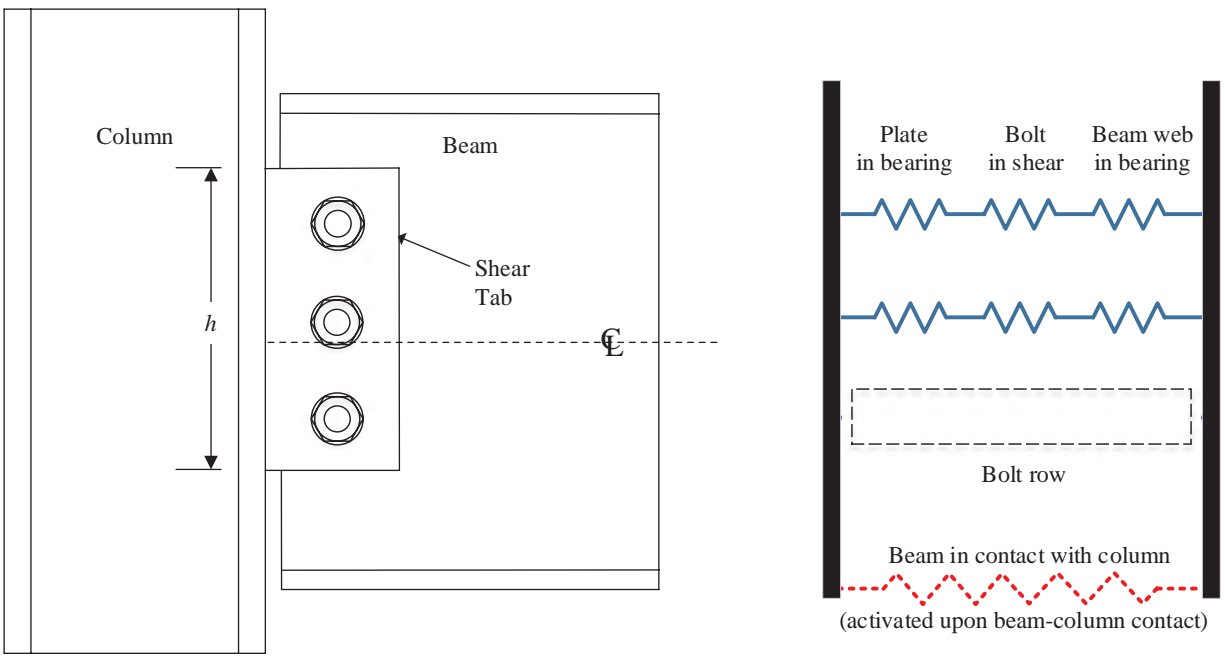
(a) Shear tab connection
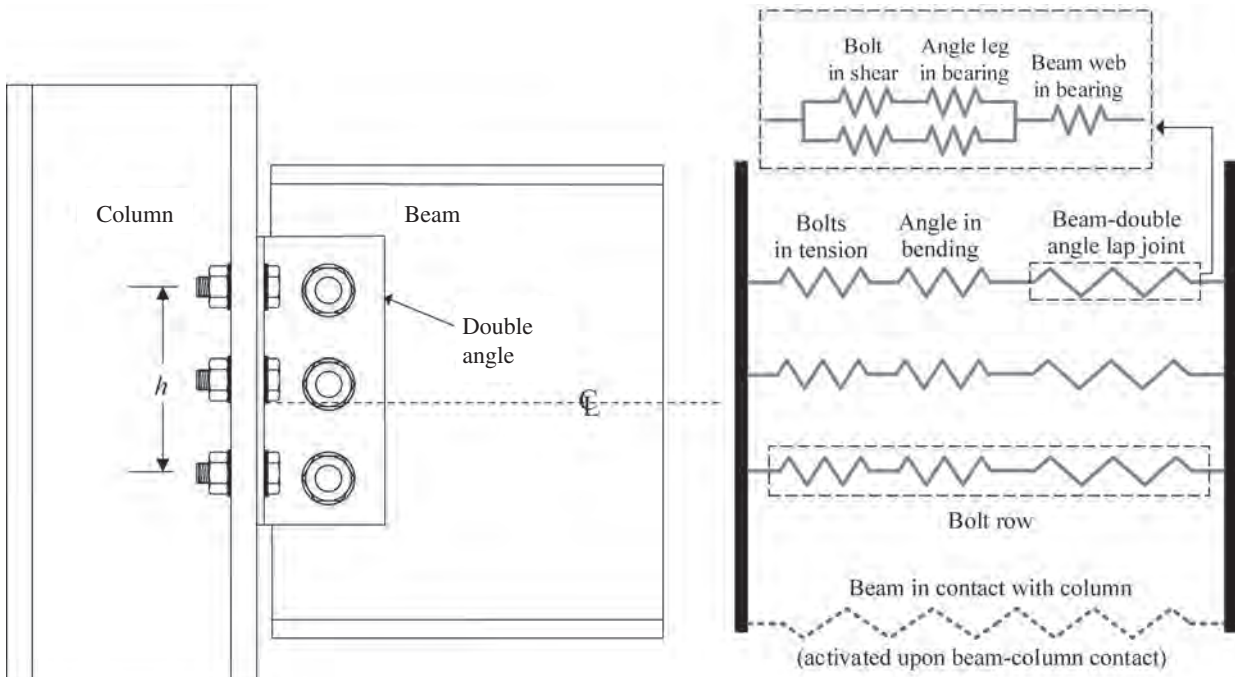
(b) Double-angle connection

Fig. 1. Connection configuration and stiffness model.

where M is the moment resulted from the shear and tension forces applied on the beam and is affected by the location of the center of rotation.

LIMIT STATES AND FAILURE MODES

The ultimate capacity of each spring component is incorporated in the stiffness model by identifying all limit states and failure modes in simple steel connections. The potential limit states of the shear tab and the double-angle connections are presented below.

Weld Strength

The weld available strength, R_{nw}, can be calculated using AISC *Specification* (2016) Section J2.4:

$$R_{nw} = 0.6F_{EXX}K_{wt}(1 + 0.5\sin^{1.5}\theta)A_{we} \qquad (14)$$

where K_{wt} is the temperature-dependent retention factor for the strength of the weld material, F_{EXX} is the filler metal classification strength at ambient temperature, θ is the angle between the line of action of the required force and the weld longitudinal axis, and A_{we} is the effective area of the weld.

Bolt Slip Resistance

To represent the inherent friction strength between steel plates due to the normal force exerted by bolt tightening, the bolt slip resistance, R_s, is calculated using AISC *Specification* Section J3.8:

$$R_s = \mu D_u h_f T_b n \qquad (15)$$

where μ is the mean slip coefficient, D_u is the ratio of the mean installed bolt pretension to the specified minimum bolt pretension, T_b is the minimum pretension force applied on the bolt, h_f is a factor of fillers, and n is the number of slip/shear planes.

Bolt Shear Strength

To determine the shear resistance per shear plane of a bolt, R_v, AISC *Specification* Section J3.6 is used:

$$R_v = 0.625K_{bt}F_{ub}A_b \qquad (16)$$

Bolt Tensile Strength

To predict the tensile strength of a bolt, R_t, subjected to a combined tensile and shear forces, the following equation is used from AISC *Specification* Section J3.6:

$$R_t = 0.83K_{bt}F_{ub}A_b \qquad (17)$$

Plate or Angle Leg Bearing and Tearout Resistance

To define the available strength of the plate or angle leg in bearing and tearout, R_{br}, the following equation is used from AISC *Specification* Section J3.10:

$$R_{br} = 3.0K_{ut}F_{ut}d_b t \le 1.5l_c tK_{ut}F_{ut} \qquad (18)$$

where l_c is the clear distance between the edge of the hole and the edge of the adjacent hole or edge of the material.

Punching Shear Resistance

The shear resistance of the plate against bolt punching, R_{pn}, can be determined using the following equation from Eurocode 3 (CEN, 2005b), Section 3.6:

$$R_{pn} = 0.6\pi d_m tK_{ut}F_{ut} \qquad (19)$$

where d_m is the mean of the across points and across flats dimensions of the bolt head or the nut, whichever is smaller.

Shear Yielding of Plate or Angle Leg

The available shear strength for shear yielding of the element, R_{vy}, is determined using AISC *Specification* Section J4.2:

$$R_{vy} = 0.6K_{yt}F_{yt}A_s \qquad (20)$$

where A_s is the gross area subject to shear.

Shear Rupture of Plate or Angle Leg

The available shear strength for shear rupture of the element, R_{vu}, is determined using AISC *Specification* Section J4.2:

$$R_{vu} = 0.6K_{ut}F_{ut}A_{s,net} \qquad (21)$$

where $A_{s,net}$ is the net area subject to shear.

Block Shear Rupture of Plate or Angle Leg

The available strength for block shear of the plate, R_{bs}, can be calculated using AISC *Specification* Section J4.3:

$$R_{bs} = U_{bs}K_{ut}F_{ut}A_{nt} + \min\left\{ \begin{array}{c} 0.6K_{ut}F_{ut}A_{nv} \\ 0.6K_{yt}F_{yt}A_{gv} \end{array} \right\} \qquad (22)$$

where U_{bs} is the tension stress distribution factor, A_{nt} is the net area subject to tension, A_{nv} is the net area subject to shear, and A_{gv} is the gross area subject to shear.

Angle Leg in Bending

The bending behavior of the bolted connections is similar to that of the T-stub during tension. Consequently, the capacity of the angle leg in bending is similar to that of an equivalent T-stub in tension. Therefore, the bending capacity of the

angle leg, R_b, for each bolt-row is represented by the following equation from Eurocode 3, Section 6.2.4:

$$R_b = \frac{4M_p}{m} \tag{23}$$

where M_p is the plastic moment capacity and can be calculated using the following equation:

$$M_p = 0.25 l_{eff,ab} t^2 K_{yt} F_{yt} \tag{24}$$

Flexural Yielding of Plate or Angle Leg

The available flexural strength in flexural yielding of the plate and the web angle leg, M_y, is determined using AISC *Specification* Section J.4.5:

$$M_y = K_{yt} F_{yt} Z_x \tag{25}$$

where Z_x is the plastic section modulus of the plate or angle leg.

Flexural Rupture of Plate or Angle Leg

The available flexural strength in flexural rupture, M_u, of the plate and the web angle leg is determined using AISC *Specification* Section J.4.5:

$$M_u = K_{ut} F_{ut} Z_{net} \tag{26}$$

where Z_{net} is the net plastic section modulus of the plate or angle leg.

BEHAVIOR OF SIMPLE CONNECTIONS IN FIRE

In this section, the general behavior of simple connections (shear tab and double angle) is divided into several phases shown in Figure 2. The phases are as follows:

Phase 1: Pre-Slip

During the initial phase, the bolts are pretensioned and the loading is applied. The response of the connection at this phase is linear and has a relatively high stiffness until the forces applied on the bolts reach the value of the slip-resistance force (Equation 15).

Phase 2: Slip

During the slip phase, the applied force on the bolts reached the bolt-slip resistance force, and slippage of the shear bolts starts having a value of $s_{slip} = d_h - d_b$ where s_{slip} is the horizontal distance that allows the bolt to slip freely before having contact with the edge of the bolt hole, and d_h is the diameter of the bolt hole. The angle at which the bolt is in contact with the bolt hole, $\theta_{bolt\text{-}contact}$, can be calculated using the following equation:

$$\theta_{bolt\text{-}contact} = \frac{s_{slip}}{p}\left(\frac{180}{\pi}\right) \tag{27}$$

where p is the vertical distance between the center of rotation and the farthest bolt-row of the connection.
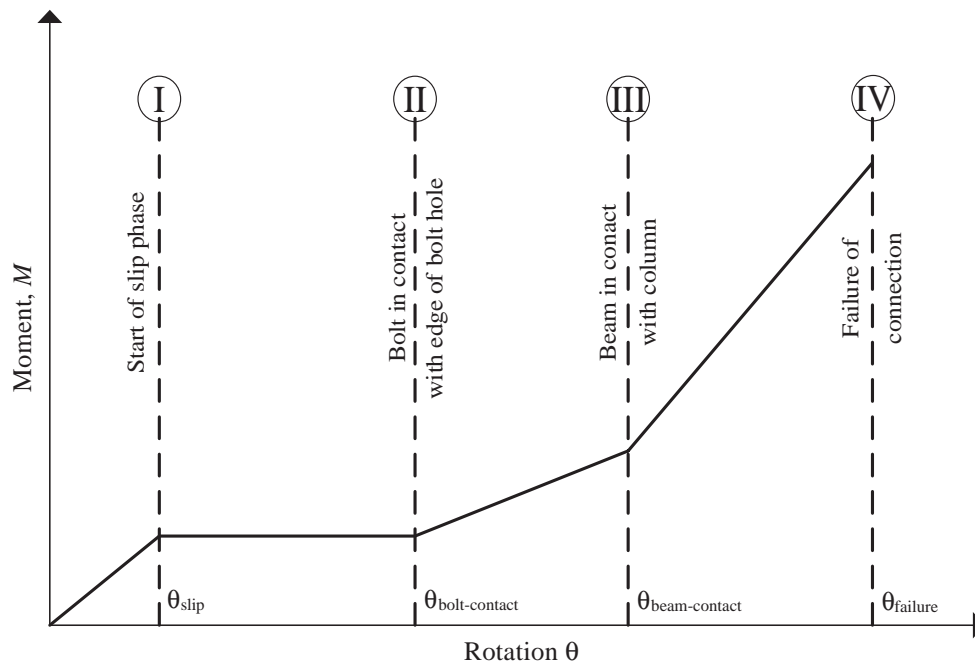
Fig. 2. Idealized behavior of shear tab and double-angle connections.

Phase 3: Bolt Contact

During this phase, the top and bottom bolts are in contact with the bolt holes, and the stiffness of the connection decreases gradually up to a degree of rotation where the contact occurs between the beam and the column flange. The angle at which the contact occurs between the beam and column can be calculated by the following equation:

$$\theta_{beam\text{-}contact} = \frac{s + s_{slip}}{D}\left(\frac{180}{\pi}\right) \tag{28}$$

where s is the setback distance between the beam and the column, and D is the distance between the beam bottom flange and the center of rotation of the connection before contact.

Phase 4: Beam Contact

Once the beam is in contact with the column, the stiffness of the connection increases and the center of rotation shifts from the middle bolt to the contact between the beam flange and the column. Moreover, the major differences in the behavior of the connection before and after beam-column contact are illustrated in Figure 3.

(a) Connection force distribution and center of rotation

(b) Stiffness model assembly and lever arm, h

Fig. 3. *Simple connections response before and after beam-column contact.*

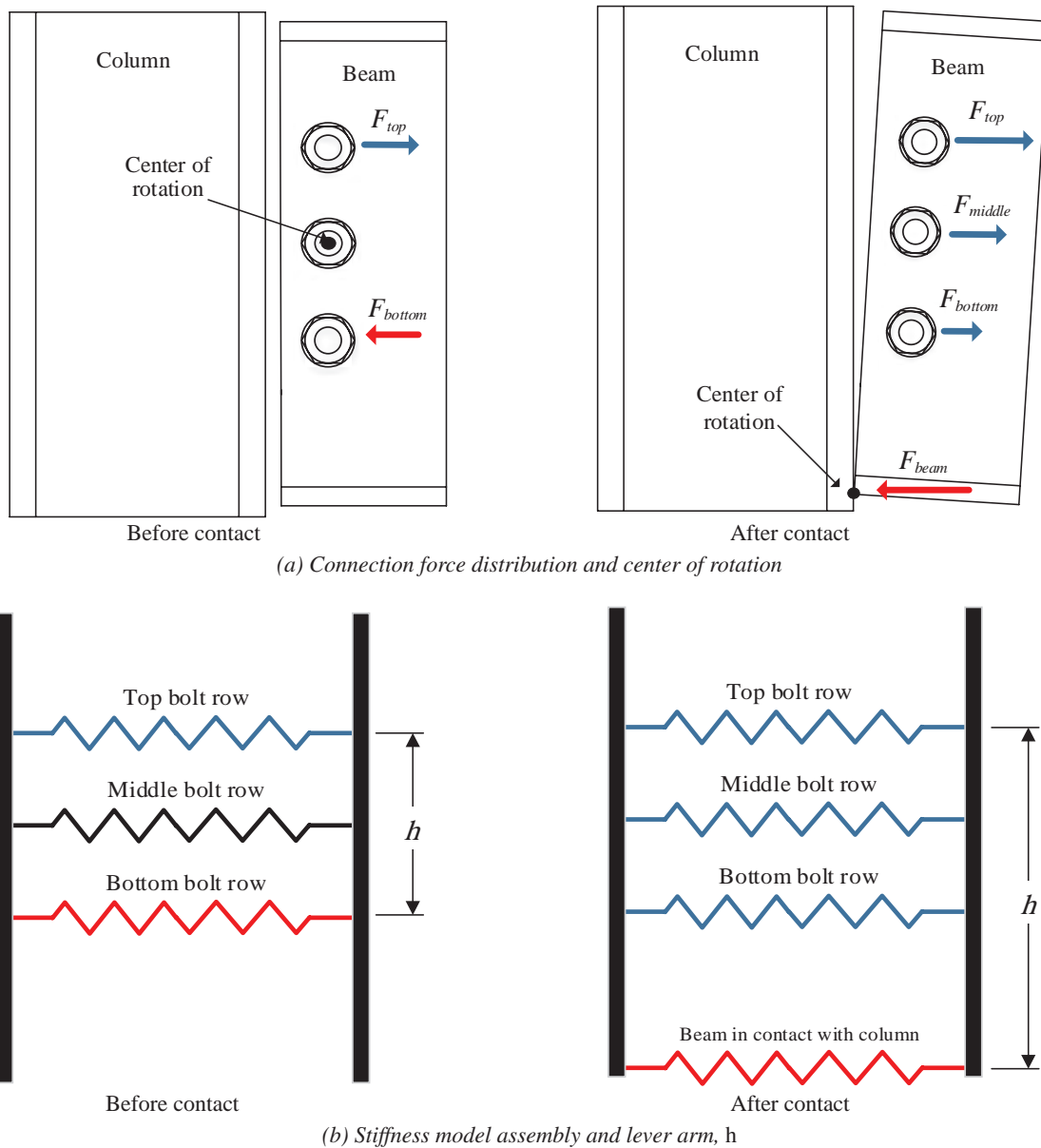| Table 1. Failure Modes of Simple Connections at Different Temperatures (Experiment vs. Stiffness Model)									
Type of Connection	Temperature		Failure Mode		Capacity				% Error
	°C	°F	Experiment	Stiffness Model	Experiment		Stiffness Model		
					kN	kips	kN	kips	
Double angle	20	68	Bolt punching the angle leg followed by block shear	Bolt punching the angle leg	243	54.6	179	40.2	26.3
	450	842	Flexural rupture of angle leg	Flexural rupture of angle leg	113	25.4	108	24.3	4.4
	550	1020	Flexural rupture of angle leg	Flexural rupture of angle leg	59.7	13.4	57.5	12.9	3.7
	650	1200	Shear bolt failure	Shear bolt failure	31.6	7.10	39.6	8.90	25.3
Shear tab	20	68	Shear bolt failure	Shear bolt failure	185	41.6	142	31.9	23.2
	450	842	Shear bolt failure	Shear bolt failure	84.0	18.9	72.3	16.3	13.9
	550	1020	Shear bolt failure	Shear bolt failure	38.5	8.66	42.9	9.64	11.4
	650	1200	Shear bolt failure	Shear bolt failure	19.3	4.34	19.1	4.29	1.04

Incremental Technique

The load-rotation response of the connections is predicted using an incremental analysis technique. The connection rotation is computed at an increment of 1.5 kN (0.34 kip) from the total applied force; thus force control is used in the analysis. The increment size is chosen to be small in order to obtain accurate results specifically when the center of rotation shifts from the middle of the shear bolts to the center of the bottom flange (contact phases). In this case, the lever arm h increases, and consequently the bolt forces are redistributed as shown in Figure 3. The connection is considered to fail when one of the connection components reaches its maximum capacity. Note that the tangent modulus is used in the components' material properties to account for material yielding.

Comparing Results

The two sets of experiments performed at the University of Sheffield (Yu et al., 2009a, 2009c) are used to examine the ability of the proposed model to predict the behavior of the shear tab and the double-angle connections. The details of the connections used in the experiment are shown in Figures 4(a) and 4(b). Figures 5(a) and 5(b) show that the proposed stiffness models are in good agreement with the experimental results of shear tab and double-angle connections, respectively, at ambient and elevated temperatures. Furthermore, the stiffness models are able to predict the ultimate strength, failure modes, and rotational capacities of the isolated simple connections.

Table 1 summarizes the comparison of failure capacities observed in the experiments and predicted using the stiffness model for each connection at ambient and elevated

temperatures. It can be seen that the stiffness model can predict the failure modes and capacities when compared with experimental tests performed at elevated temperatures on the shear tab and double-angle connections (University of Sheffield, 2007).

Limitations and Assumptions of the Proposed Stiffness Model

• The excessive ovalization of the shear bolt holes was not taken into consideration in the proposed model, which underpredicts the full strength and ductility of the shear tab and the double-angle connections at ambient temperature as shown in Figures 5(a) and 5(b) and Table 1.

• The proposed stiffness model is able to predict the behavior of the simple connections up to the first component failure. The following fracture mechanism was not included in the proposed model. However, failure was predicted as the steel material reaches its ultimate strength.

• The stiffness model is developed for fast heating cases, thus the time-dependent properties of steel (thermal creep effect) are not considered.

FIRE DESIGN EXAMPLES OF SIMPLE CONNECTIONS

A step-by-step procedure that incorporates the developed stiffness model in the fire design of steel connections is presented. The procedure is thoroughly explained in the two examples: shear tab and double-angle connections in an isolated frame. Some assumptions are made to propose a simple and conservative fire design guideline. The examples
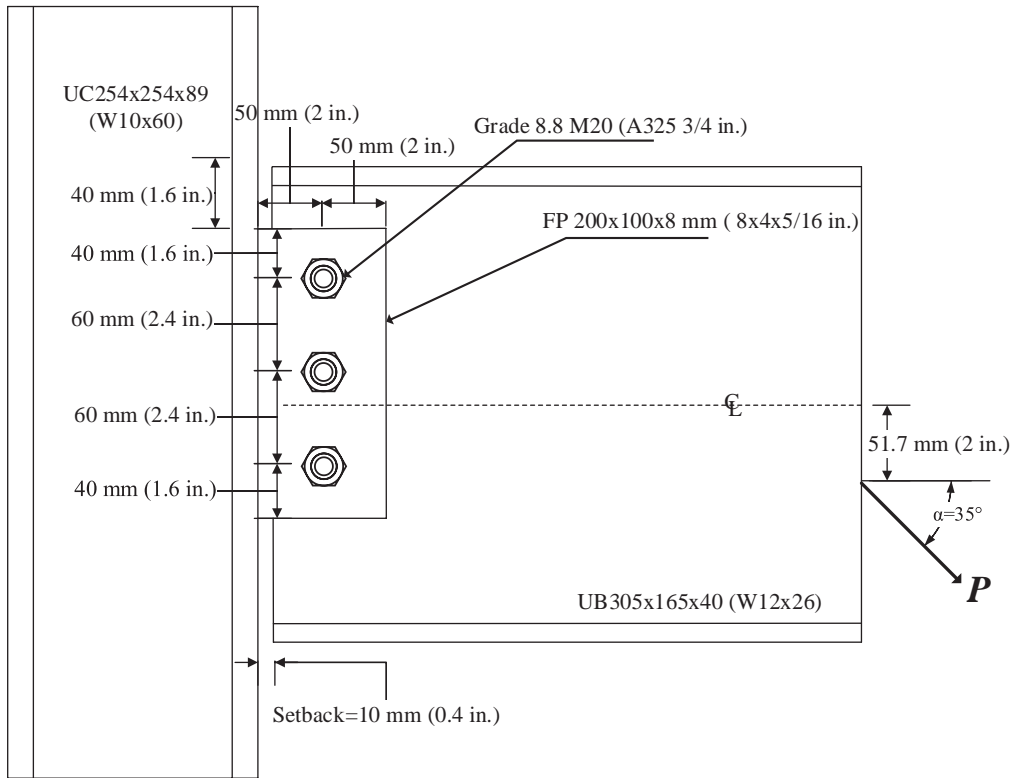
(a) Shear tab connection
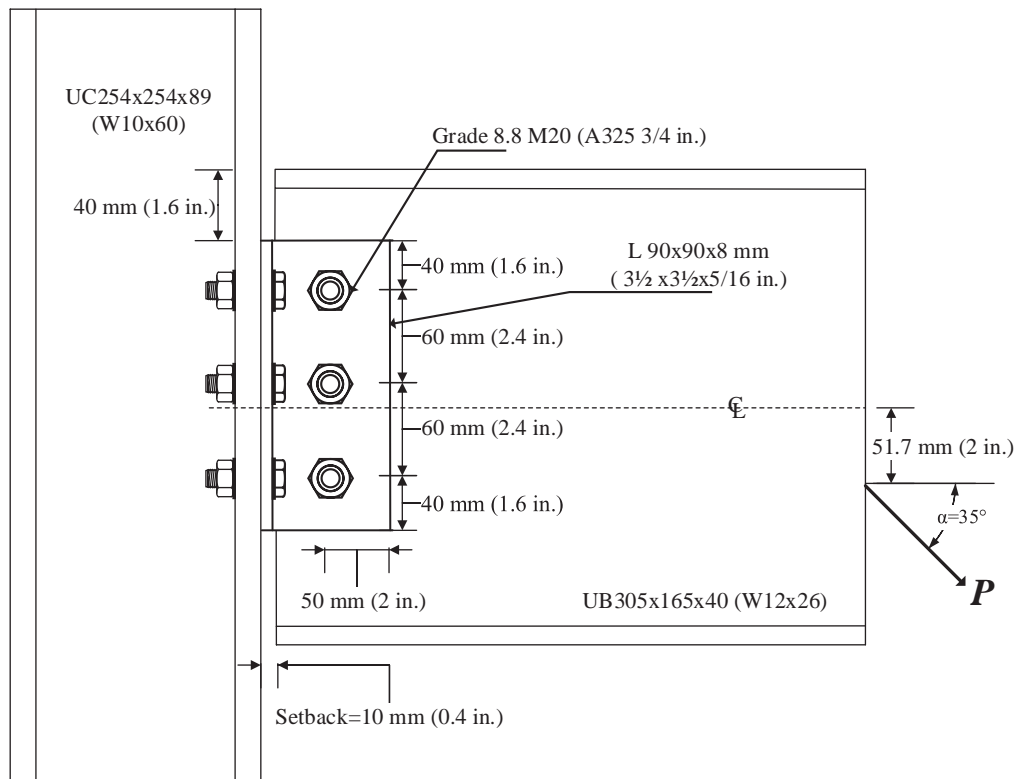
(b) Double-angle connection

Fig. 4. Details of the isolated connections (University of Sheffield, 2007).

illustrate the different key aspects in designing both shear tab and double-angle connections when subjected to fire. Afterward, a comparison between the two connections' design is duly made based on the results and conclusions are drawn.

Design Criteria

The primary goal of the presented study, which is illustrated in the following two examples, is to design the shear connection to maintain the load transfer between the beam and the column at least before the failure of the steel beam in fire events. The beam failure in most cases resembles the beam catenary action initiation (formation of plastic hinges), which occurs at very high fire temperatures. Consequently, and due to excessive beam sagging, tensile forces are exerted on the connections, causing them to fail. However, the study focuses on designing the connection to maintain the load transfer as long as the beam remains intact. This will prevent or at least delay the failure of the system; allowing more time for occupants to evacuate the building.

Three factors need to be taken into consideration when designing simple steel connections under fire conditions: gravity loads, induced axial load due to thermal expansion, and moment demand exerted by the beam on the connection. It is worth mentioning that transient-state conditions of fire are considered. The temperature is increased from ambient temperature, 20°C (68°F), up to the target temperature. The slip of shear planes is implicitly included in the stiffness model. The connection and the beam are uniformly heated.

In many fire tests, the columns were observed to remain in the elastic region during fire. As the primary structural
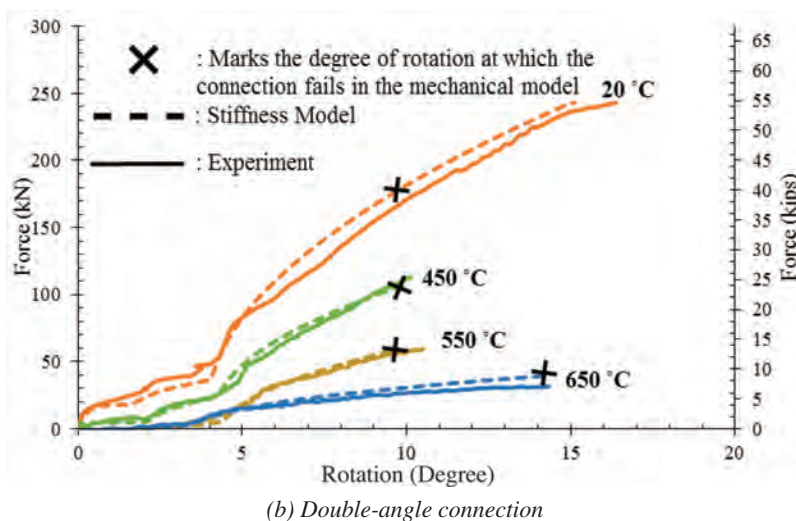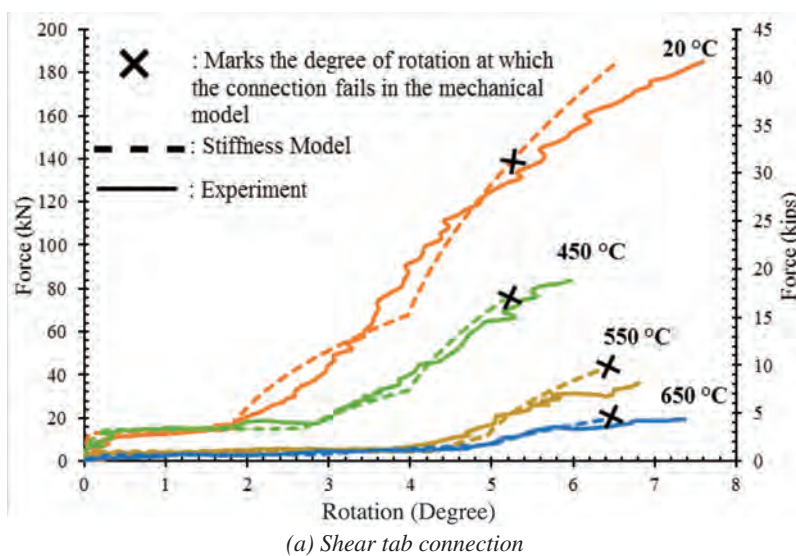

(a) Shear tab connection

(b) Double-angle connection

Fig. 5. Comparison between results from experiments and stiffness model.

Table 2. Material Properties Retention Factors at Different Temperatures							
Retention Factor	Reference	Temperature (°C)				
		20	400	500	600	700
Modulus of elasticity, K_E	Lee et al. (2013)	1.0	0.89	0.77	0.57	0.26
Base material yield strength, K_{yt}	Lee et al. (2013)	1.0	0.72	0.66	0.44	0.21
Base material ultimate strength, K_{ut}	Lee et al. (2013)	1.0	0.97	0.64	0.37	0.18
Bolt ultimate strength, K_{bt}	Hu et al. (2007)	1.0	0.66	0.379	0.19	0.06
Weld ultimate strength, K_{wt}	Eurocode 3 (CEN, 2005a)	1.0	0.876	0.627	0.378	0.13

element in steel structures, columns are usually protected using insulating material to reduce the column temperature increase during fire. Thus, the columns are assumed to be insulated, and the column temperature can be roughly estimated to reach 60% of the (unprotected) beam temperature as shown in previous studies (Zhang and Usmani, 2015). Columns are assumed to be fixed from both ends against rotation and translation. The frame is perfectly symmetrical in loading and geometry.

Design Steps

First, the connection is designed to meet both serviceability and strength requirements prescribed in the structural design codes at ambient temperature and under gravity loads only. The applied loads, due to fire, are calculated, and the stresses on each component of the connection are obtained. These additional stresses are the induced axial forces due to the restrained thermal expansion and the moment demand on the connection due to beam sagging and rotation. It is well known that the column stiffness is the controlling factor in determining the magnitude of the induced axial force in the beam by providing the beam end axial restraint (Wang et

al., 2011). Therefore, when calculating the thermal induced axial forces, only the column flexural stiffness is considered for simplicity. This assumption is valid and considered conservative because the beam axial stiffness is relatively high when compared with the column flexural stiffness. The induced axial force is calculated first by quantifying the change of the beam length due to thermal expansion and including it as an imposed horizontal deflection at the midspan of the column. Then, by knowing the column stiffness, the induced axial force can be easily calculated.

The moment applied on the connection is obtained by a simple graphical solution, where the beam end rotational stiffness (beam-line) and the connection rotational stiffness (based on the developed stiffness model) are plotted and the moment demand (intersection between the two curves) is obtained. After obtaining the new stresses, all the connection limit states are checked, while multiplying each equation by its corresponding retention factor. These retention factors are in function of temperature and they are summarized in Table 2. The connection is redesigned accordingly. These steps are repeated until reaching a final connection configuration that can withstand the additional stresses while considering strength degradation.

DESIGN EXAMPLE 1— SINGLE-PLATE SHEAR CONNECTION IN FIRE

Given:

Check the single-plate shear connection shown in Figure 6 when subjected to fire conditions. The beam is an ASTM A992 W16×40 with a length of $L = 20$ ft. The column is an ASTM A992 W10×49 with a height of $H = 20$ ft. The column is assumed to be fixed at both ends with a floor height of 10 ft. The beam and connection are unprotected; the column is protected.

The beam is connected to the column using an ASTM A572 Grade 50 single plate with one column of three ¾-in.-diameter Group A bolts. The threads are not included in the shear plane (thread condition X). The beam setback is 0.4 in.

The beam and the connection are uniformly heated from an ambient temperature of 20°C (68°F) up to 500°C (932°F). The beam is assumed to carry a maximum of half its plastic moment strength at ambient temperature. The beam top flange is laterally supported along its length. Thermal creep effect is not included.

Solution:

From AISC *Manual* (2017) Tables 2-4 and 2-5, the material properties are as follows:

Beam and column
ASTM A992
$F_y = 50$ ksi
$F_u = 65$ ksi

Plate
ASTM 572, Grade 50
$F_y = 50$ ksi
$F_u = 65$ ksi

From AISC *Manual* Table 1-1, the geometric properties are as follows:

Beam
W16×40
d = 16.0 in.
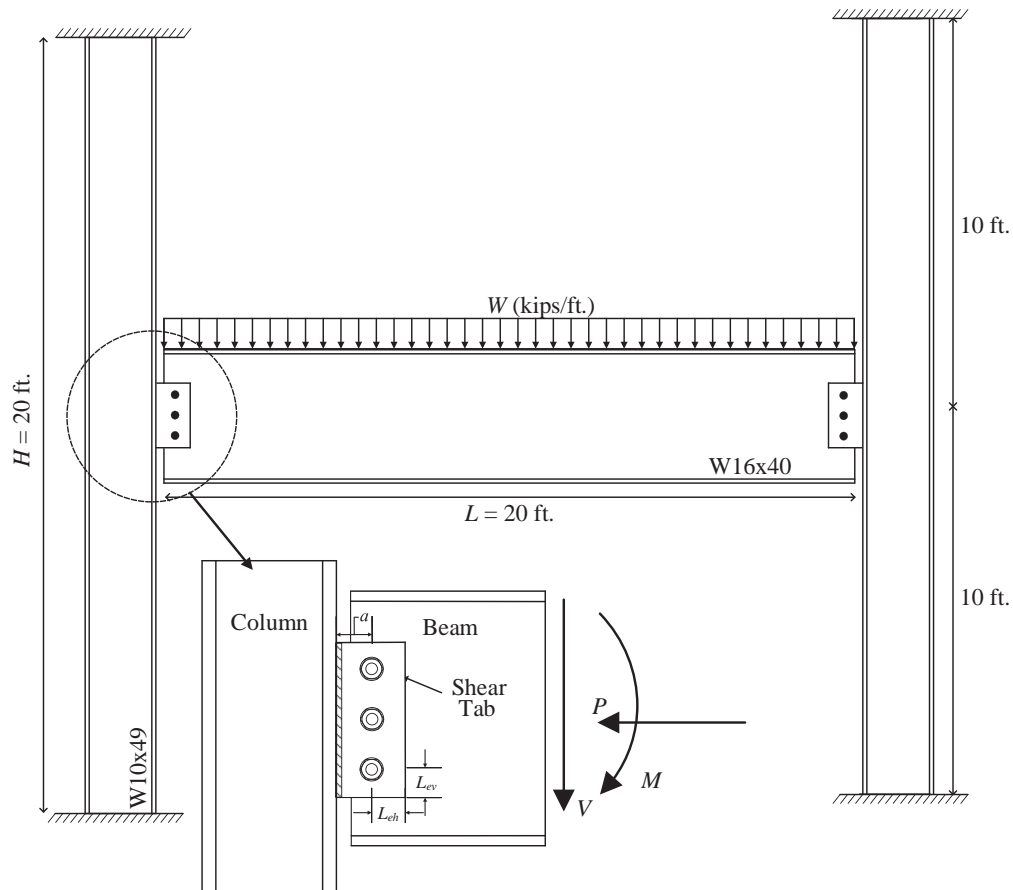t_w = 0.305 in.
S_x = 64.7 in.^{3}
Z_x = 73.0 in.^{4}

Fig. 6. Example 1 configuration of column-beam frame system connected with a single plate.

Column
W10×49
$I_x = 272$ in.^{4}

From Table 2, the material property retention factors at 500°C (932°F) are:

$K_E = 0.77$
$K_{yt} = 0.66$
$K_{ut} = 0.64$
$K_{bt} = 0.379$
$K_{wt} = 0.627$

Step 1—Compute the Applied Distributed Load

The maximum moment developed at mid-span of the beam is determined using AISC *Manual* Table 3-23, Case 1:

$$M_{max} = \frac{wL^2}{8}$$

The beam plastic moment is determined from AISC *Specification* Equation F2-1:

$$M_p = Z_x F_y \qquad\qquad\qquad\qquad (\textit{Spec.} \text{ Eq. F2-1})$$

$$= \frac{(73.0 \text{ in.}^3)(50 \text{ ksi})}{12 \text{ in./ft}}$$

$$= 304 \text{ kip-ft}$$

The applied load should exert a maximum moment of 50% of the beam plastic moment capacity at ambient temperature; therefore:

$$w = \frac{8(0.5M_p)}{L^2}$$

$$= \frac{8(0.5)(304 \text{ kip-ft})}{(20 \text{ ft})^2}$$

$$= 3.04 \text{ kip/ft}$$

Use $w = 3$ kip/ft

Step 2—Single-Plate Shear Connection Configuration

The single-plate shear connection is designed following the AISC *Manual* Part 10, Single-Plate Shear Connections—Conventional Configuration. Try a ⅜-in.-thick plate with $l_{ev} = 1\frac{1}{2}$ in., $l_{eh} = 2$ in. and $s = 2\frac{1}{2}$ in.

From AISC *Specification* Table J3.4, the minimum vertical edge distance, for a ¾-in.-diameter bolt is 1 in.:

$l_{ev} = 1\frac{1}{2}$ in. > 1 in.   **o.k.**

From AISC *Manual* Part 10, the minimum horizontal edge distance is: $2d = 2(¾ \text{ in.}) = 1\frac{1}{2}$ in.

$l_{ev} = 2$ in. $> 1\frac{1}{2}$ in.   **o.k.**

The maximum plate thickness is determined using AISC *Manual* Table 10-9. For three bolts in STD holes:

$$t_{p,max} = \frac{d}{2} + \frac{1}{16} \text{ in.}$$

$$= \frac{¾ \text{ in.}}{2} + \frac{1}{16} \text{ in.}$$

$$= 0.438 \text{ in.} > ⅜ \text{ in.}\quad \textbf{o.k.}$$

With a setback distance equal to 0.4 in., use $a = 2\frac{1}{2}$ in. From AISC *Manual* Table 10-9, with three bolts in STD holes, the eccentricity is:

$$e = \frac{a}{2}$$
$$= \frac{2\frac{1}{2} \text{ in.}}{2}$$
$$= 1.25 \text{ in.}$$

The minimum length of the plate should be greater than half the depth of the beam. The minimum bolt spacing is determined as follows:

$$s = \left(\frac{1}{n-1}\right)\left(\frac{d}{2} - 2l_{ev}\right)$$
$$= \left(\frac{1}{3-1}\right)\left[\frac{16.0 \text{ in.}}{2} - 2(1\frac{1}{2} \text{ in.})\right]$$
$$= 2\frac{1}{2} \text{ in.}$$

From AISC *Manual* Part 10, the required fillet weld size for a $\frac{3}{8}$-in.-thick plate is:

$$\frac{5}{8}t_p = (\frac{5}{8})(\frac{3}{8} \text{ in.})$$
$$= 0.234 \text{ in.}$$

Use $\frac{1}{4}$-in. fillet welds.

Step 3—Check the Beam Strength

  Step 3a—Check for beam catenary action

  The maximum moment in the beam (at mid-span) is determined using AISC *Manual* Table 3-23, Case 1:

$$\frac{wL^2}{8} = \frac{(3 \text{ kip/ft})(20 \text{ ft})^2}{8}$$
$$= 150 \text{ kip-ft}$$

  The beam elastic moment capacity is:

$$K_{yt}F_{yt}S_x = \frac{0.66(50 \text{ ksi})(64.7 \text{ in.}^3)}{12 \text{ in./ft}}$$
$$= 178 \text{ kip-ft} > 150 \text{ kip-ft}$$

  The beam will remain in the elastic zone; no catenary action will occur.

  Step 3b—Check beam shear strength

  The maximum shear applied on the beam (at the support) is determend using AISC *Manual* Table 3-23, Case 1:

$$V = \frac{wL}{2}$$
$$= \frac{(3 \text{ kip/ft})(20 \text{ ft})}{2}$$
$$= 30.0 \text{ kips}$$

The shear yielding strength of the beam is determined as follows:

$$A_s = dt_w$$
$$= (16.0 \text{ in.})(0.305 \text{ in.})$$
$$= 4.88 \text{ in.}^2$$

$$0.6K_{yt}F_{yt}A_s = 0.6(0.66)(50 \text{ ksi})(4.88 \text{ in.}^2)$$
$$= 96.6 \text{ kips} > 30.0 \text{ kips} \quad \textbf{o.k.}$$

Step 4—Determine the Forces on the Connection

Step 4a—Shear force on the connection due to gravity load

The shear force at the connection is determend using AISC *Manual* Table 3-23, Case 1:

$$V = \frac{wL}{2}$$
$$= \frac{(3 \text{ kip/ft})(20 \text{ ft})}{2}$$
$$= 30.0 \text{ kips}$$

Step 4b—Compressive force on the connection due to thermal expansion of the beam

The coefficient of thermal expansion coefficient is:

$$\alpha = 1.2(10^{-5})/°\text{C}$$
$$= 6.67(10^{-6})/°\text{F}$$

The elongation of the beam due to thermal expansion is:

$$\Delta l = L(\Delta T)(\alpha)$$
$$= (20 \text{ ft})(932°\text{F} - 68°\text{F})(6.67/°\text{F})(10^{-6})(12 \text{ in./ft})$$
$$= 1.38 \text{ in.}$$

Because the frame is symmetrical, the horizontal displacement at the column mid-span is:

$$\Delta = \frac{\Delta l}{2}$$
$$= \frac{1.38 \text{ in.}}{2}$$
$$= 0.690 \text{ in.}$$

The column temperature is roughly estimated to be 300°C (572°F), which is 60% of the beam temperature. From Table 3, the K_E at 300°C (572°F) is estimated at 0.90. Thus, the thermal compressive force applied to the connection is:

$$\Delta = \frac{PH^3}{48K_E EI_x}$$

Solving for P:

$$P = \frac{48 \Delta K_E E I_x}{H^3}$$

$$= \frac{48(0.690 \text{ in.})(0.90)(29{,}000 \text{ ksi})(272 \text{ in.}^4)}{(20 \text{ ft})^3 (12 \text{ in/ft})^3}$$

$$= 17.0 \text{ kips}$$

Step 4c—Moment applied at the connection

At ambient temperatures, designers consider the shear tab connection an ideally pinned connection where its moment demand is negligible. However, as temperature increases, the flexural stiffness of the connected beam decreases, and thus an increase in the connection rotation can be observed. Due to this excessive rotation, the bending moment applied on the shear plate cannot be ignored, and it is important to take it into consideration in fire design. A simple way to calculate the applied moment is by getting the intersection between the beam line (also called load line) and the connection stiffness by which the moment and end rotation are obtained. The beam line is a straight line that can be plotted from the moment and end rotation for a fixed-end beam and simply supported beam.

For a simply supported beam:

$$\theta_c = \frac{wL^3}{24 K_E E I_x}$$

$$= \frac{(3 \text{ kip/ft})(20 \text{ ft})^3 (12 \text{ in./ft})^2}{24(0.771)(29{,}000 \text{ ksi})(518 \text{ in.}^4)}$$

$$= 0.0124 \text{ rad}$$

$$M = 0 \text{ kip-in.}$$

For a fixed-end beam:

$$\theta_c = 0 \text{ rad}$$

$$M = \frac{wL^2}{12}$$

$$= \frac{(3 \text{ kip/ft})(20 \text{ ft})^2 (12 \text{ in./ft})}{12}$$

$$= 1{,}220 \text{ kip-in.}$$

The beam-line and moment-rotation characteristics (using stiffness model) of the connection are plotted in Figure 7. The moment applied to the connection is determined at the intersection of these two lines. Use $M = 17.7$ kip-in.

M is used to check the strength of the shear tab connection when subjected to beam-end moments.

Step 5—Compute the Applied Shear Force on the Bolts

Step 5a—Bolt shear force due to gravity load

$$V_v = \frac{V}{n}$$

$$= \frac{30.0 \text{ kips}}{3 \text{ bolts}}$$

$$= 10.0 \text{ kips/bolt}$$

Step 5b—Bolt shear force due to thermal expansion

$$V_p = \frac{P}{n}$$
$$= \frac{17.0 \text{ kips}}{3 \text{ bolts}}$$
$$= 5.67 \text{ kips/bolt}$$

Step 5c—Bolt shear force due to the applied moment on the connection

$$V_m = \frac{M}{(n-1)s}$$
$$= \frac{17.7 \text{ kip-in.}}{(3-1)(2\frac{1}{2} \text{ in.})}$$
$$= 3.54 \text{ kips/bolt}$$

Step 5d—Applied shear force on each bolt

$$V_{top} = \sqrt{(V_m - V_p)^2 + (V_v)^2}$$
$$= \sqrt{(3.54 \text{ kips} - 5.67 \text{ kips})^2 + (10.0 \text{ kips})^2}$$
$$= 10.2 \text{ kips}$$

$$V_{middle} = \sqrt{(V_p)^2 + (V_v)^2}$$
$$= \sqrt{(5.67 \text{ kips})^2 + (10.0 \text{ kips})^2}$$
$$= 11.5 \text{ kips}$$

$$V_{bottom} = \sqrt{(V_p + V_m)^2 + (V_v)^2}$$
$$= \sqrt{(3.54 \text{ kips} + 5.67 \text{ kips})^2 + (10.0 \text{ kips})^2}$$
$$= 13.6 \text{ kips}$$
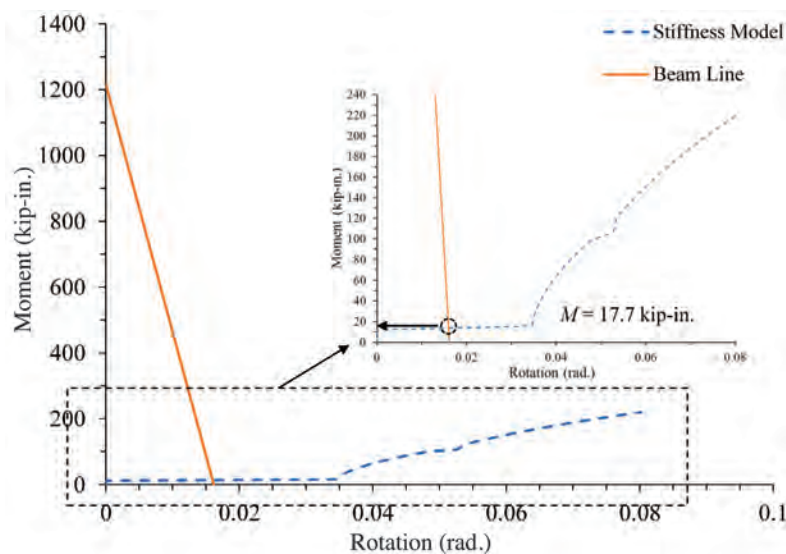
Fig. 7. Moment demand on the shear tab connection using beam-line theory.

Step 6—Determine the Strength of the Plate

Step 6a—Shear yielding

$$A_s = lt_p$$
$$= (8.00 \text{ in.})(\tfrac{3}{8} \text{ in.})$$
$$= 3.00 \text{ in.}^2$$

$$R_{vy} = 0.6K_{yt}F_{yt}A_s$$
$$= 0.6(0.66)(50 \text{ ksi})(3.00 \text{ in.}^2)$$
$$= 59.4 \text{ kips} > 30.0 \text{ kips} \quad \textbf{o.k.}$$

Step 6b—Shear rupture

$$A_n = \left[l - n(d + \tfrac{1}{16} \text{ in.})\right]t_p$$
$$= \left[8.00 \text{ in.} - 3(\tfrac{13}{16} \text{ in.} + \tfrac{1}{16} \text{ in.})\right](\tfrac{3}{8} \text{ in.})$$
$$= 2.02 \text{ in.}^2$$

$$R_{vu} = 0.6K_{ut}F_{ut}A_n$$
$$= 0.6(0.64)(65 \text{ ksi})(2.02 \text{ in.}^2)$$
$$= 50.4 \text{ kips} > 30.0 \text{ kips} \quad \textbf{o.k.}$$

Step 6c—Flexural yielding

$$Z_x = \frac{t_p l^2}{4}$$
$$= \frac{(\tfrac{3}{8} \text{ in.})(8.00 \text{ in.})^2}{4}$$
$$= 6.00 \text{ in.}^3$$

$$M_y = K_{yt}F_{yt}Z_x$$
$$= 0.66(50 \text{ ksi})(6.00 \text{ in.}^3)$$
$$= 198 \text{ kip-in.} > 17.7 \text{ kip-in.} \quad \textbf{o.k.}$$

Step 6d—Flexural rupture

The net plastic section modulus is not calculated here. Use $Z_{net} = 3.56 \text{ in.}^3$

$$M_u = K_{ut}F_{ut}Z_{net}$$
$$= 0.64(65 \text{ ksi})(3.56 \text{ in.}^3)$$
$$= 148 \text{ kip-in.} > 17.7 \text{ kip-in.} \quad \textbf{o.k.}$$

Step 6e—Block shear rupture

$$R_n = 0.60A_{nv}K_{ut}F_{ut} + U_{bs}A_{nt}K_{ut}F_{ut} \le 0.60A_{gv}K_{yt}F_{yt} + U_{bs}A_{nt}K_{ut}F_{ut}$$

where

$$A_{nt} = \left[2.00 \text{ in.} - 0.5(\tfrac{13}{16} \text{ in.} + \tfrac{1}{16} \text{ in.})\right](\tfrac{3}{8} \text{ in.})$$
$$= 0.586 \text{ in.}^2$$

$$A_{gv} = (5.00 \text{ in.} + 1\tfrac{1}{2} \text{ in.})(\tfrac{3}{8} \text{ in.})$$
$$= 2.44 \text{ in.}^2$$

$$A_{nv} = \left[(5.00 \text{ in.} + 1\tfrac{1}{2} \text{ in.}) - 2.5(\tfrac{13}{16} \text{ in.} + \tfrac{1}{16} \text{ in.})\right](\tfrac{3}{8} \text{ in.})$$
$$= 1.62 \text{ in.}^2$$

$$U_{bs} = 1.0$$

$$0.60 A_{nv} K_{ut} F_{ut} = 0.60(1.62 \text{ in.}^2)(0.64)(65 \text{ ksi})$$
$$= 40.4 \text{ kips}$$

$$0.60 A_{gv} K_{yt} F_{yt} = 0.60(2.44 \text{ in.}^2)(0.66)(50 \text{ ksi})$$
$$= 48.3 \text{ kips}$$

$$U_{bs} A_{nt} K_{ut} F_{ut} = 1.0(0.586 \text{ in.}^2)(0.64)(65 \text{ ksi})$$
$$= 24.4 \text{ kips}$$

$$R_n = 0.60 A_{nv} K_{ut} F_{ut} + U_{bs} A_{nt} K_{ut} F_{ut} \le 0.60 A_{gv} K_{yt} F_{yt} + U_{bs} A_{nt} K_{ut} F_{ut}$$
$$= 40.4 \text{ kips} + 24.4 \text{ kips} < 48.3 \text{ kips} + 24.4 \text{ kips}$$
$$= 64.8 \text{ kips} > 30.0 \text{ kips} \quad \textbf{o.k.}$$

Step 7—Weld Strength

$$f_v = \frac{V}{2l}$$
$$= \frac{30.0 \text{ kips}}{2(8.00 \text{ in.})}$$
$$= 1.88 \text{ kip/in.}$$

The moment applied to the weld is:

$$M + Ve = 17.7 \text{ kip-in.} + (30 \text{ kips})(1.25 \text{ in.})$$
$$= 55.2 \text{ kip-in.}$$

Maximum stress perpendicular to the weld is:

$$f_t = \frac{(M + Ve)l}{4(I_{weld})}$$
$$= \frac{12(55.2 \text{ kip-in.})(8.00 \text{ in.})}{4(8.00 \text{ in.})^3}$$
$$= 2.59 \text{ kip/in.}$$

Therefore, the maximum resultant force is:

$$\sqrt{f_t^2 + f_v^2} = \sqrt{(2.59 \text{ kips/in.})^2 + (1.88 \text{ kips/in.})^2}$$
$$= 3.20 \text{ kip/in.}$$

$$\theta = \tan^{-1}\left(\frac{f_t}{f_v}\right)$$
$$= \tan^{-1}\left(\frac{2.59 \text{ kips/in.}}{1.88 \text{ kips/in.}}\right)$$
$$= 54.0°$$

Table 3. Summary of the Limit State Avalable Strength of a Single-Plate Shear Connection in Fire [500°C (932°F)]	
Mode	**Available Strength**
Shear yielding of plate =	59.4 kips
Shear rupture of plate =	50.4 kips
Flexural yielding of plate =	198 kip-in.
Flexural rupture of plate =	148 kip-in.
Block shear of plate =	64.8 kips
Weld strength =	6.35 kip/in.
Bolt shear strength =	12.6 kips/bolt
Shear plate bearing and tearout strength =	24.8 kips/bolt
Beam bearing and tearout strength =	28.5 kips/bolt

$$R_{nw} = 0.6K_{wt}F_{EXX}\left(1+0.5\sin^{1.5}\theta\right)A_{we}$$

$$= 0.6(0.627)(70 \text{ ksi})\left[1+0.5\sin^{1.5}(54.0°)\right](0.707)(\text{¼ in.})$$

$$= 6.35 \text{ kip/in.} > 3.20 \text{ kip/in.} \quad \textbf{o.k.}$$

Step 8—Check Shear Transfer at Bolts

Step 8a—Bolt shear strength

$$R_v = 0.625nK_{bt}F_{ub}A_s$$

$$= 0.625(1)(0.379)(120 \text{ ksi})\left[\frac{\pi(\text{¾ in.})^2}{4}\right]$$

$$= 12.6 \text{ kips/bolt}$$

Step 8b—Plate bearing and tearout strength

$$R_{br} = 3.0K_{ut}F_{ut}d_bt \le 1.5l_ctK_{ut}F_{ut}$$

$$= 3.0(0.64)(65 \text{ ksi})(\text{¾ in.})(\text{⅜ in.}) \le 1.5(1.06 \text{ in.})(\text{⅜ in.})(0.64)(65 \text{ ksi})$$

$$= 24.8 \text{ kips/bolt}$$

Step 8c—Beam web bearing and tearout strength

$$R_{br} = 3.0K_{ut}F_{ut}d_bt \le 1.5l_ctK_{ut}F_{ut}$$

$$= 3.0(0.64)(65 \text{ ksi})(\text{¾ in.})(0.305 \text{ in.}) \le 1.5(1.66 \text{ in.})(0.305 \text{ in.})(0.64)(65 \text{ ksi})$$

$$= 28.5 \text{ kips/bolt}$$

Step 8d—Shear transfer at bolts

The shear transfer strength at the bolts is the minimum of the bolt shear strength, bearing and tearout strength at the plate, and bearing and tearout strength of the beam web.

$$R_v = \min\{12.6 \text{ kips/bolt}, 24.8 \text{ kips/bolt}, 28.5 \text{ kips/bolt}\}$$

$$= 12.6 \text{ kips/bolt}$$

$$V_{top} = 10.2 \text{ kips} < 12.6 \text{ kips} \quad \textbf{o.k.}$$

$V_{middle} = 11.5 \text{ kips} < 12.6 \text{ kips}$ **o.k.**

$V_{bottom} = 13.6 \text{ kips} > 12.6 \text{ kips}$ **n.g.**

The connection will fail by shear rupture of the bottom bolt. Neglecting the thermal compressive forces, generated due to the expansion of the beam, and the moment demand leads to unsafe design. Increasing the bolt diameter or using a stronger bolt grade will produce a safe design.

A summary of the limit state capacities is presented in Table 3. The final design of the shear plate connection is shown Figure 8.

DESIGN EXAMPLE 2—DOUBLE-ANGLE CONNECTION IN FIRE

Given:

Check the double-angle shear connection shown in Figure 9 when subjected to fire conditions. The beam is an ASTM A992 W16×40 with a length of $L = 20$ ft. The column is an ASTM A992 W10×49 with a height of $H = 20$ ft. The column is assumed to be fixed at both ends with a floor height of 10 ft. The beam and connection are unprotected; the column is protected.

The beam is connected to the column using an ASTM A572 Grade 50 double angle. The beam is connected to the double angle through a single column of three bolts, and the double angle is connected to the column through two columns of three bolts. Bolts are ¾-in.-diameter Group A with the threads not included in the shear plane (thread condition X). The beam setback is 0.4 in.

The beam and the connection are uniformly heated from an ambient temperature of 20°C (68°F) up to 500°C (932°F). The beam is assumed to carry a maximum of half its plastic moment strength at ambient temperature. The beam top flange is laterally supported along its length. Thermal creep effect is not included.

Solution:

From AISC *Manual* Tables 2-4 and 2-5, the material properties are as follows:

Beam and column
ASTM A992
$F_y = 50$ ksi
$F_u = 65$ ksi
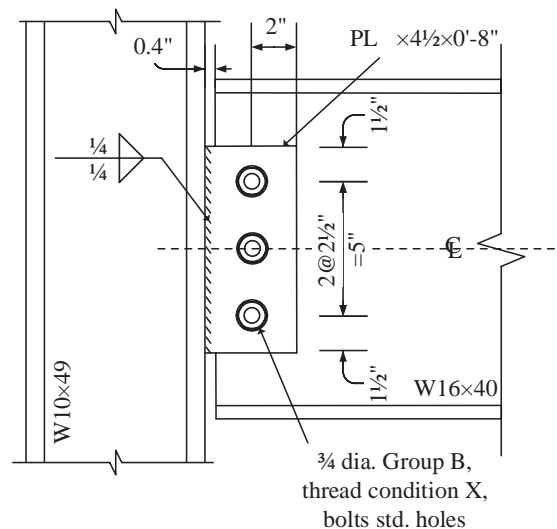
Fig. 8. Detailed design for W16×40 beam connected to W10×49 column through a single-plate connection.

Angle
ASTM 572, Grade 50
$F_y = 50$ ksi
$F_u = 65$ ksi

From AISC *Manual* Table 1-1, the geometric properties are as follows:

Beam
W16×40
$d = 16.0$ in.
$t_w = 0.305$ in.
$S_x = 64.7$ in.^{3}
$Z_x = 73.0$ in.^{3}

Column
W10×49
$I_x = 272$ in.^{4}

From Table 2, the material property retention factors at 500°C (932°F) are:

$K_E = 0.77$
$K_{yt} = 0.66$
$K_{ut} = 0.64$
$K_{bt} = 0.379$
$K_{wt} = 0.627$
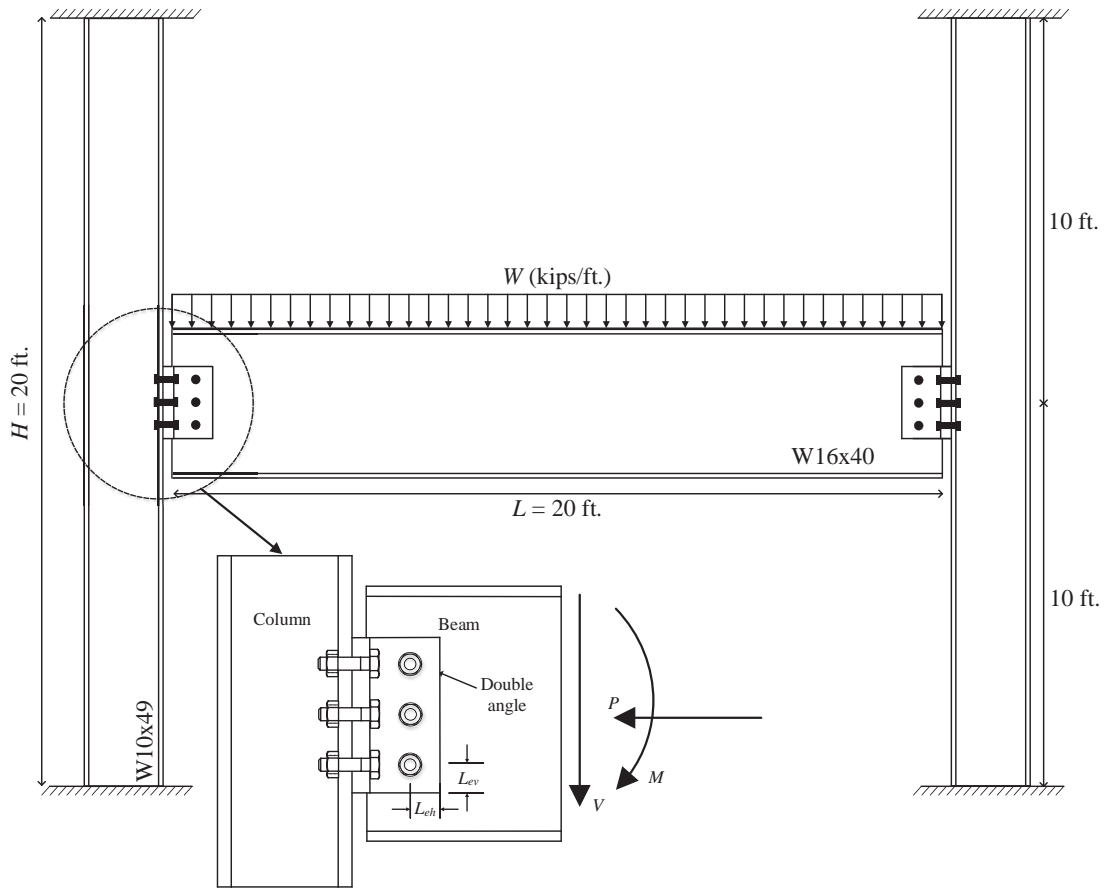
Fig. 9. Example 2 configuration of column-beam frame system connected with a double angle.

Step 1—Compute the Applied Distributed Load

The maximum moment developed at mid-span of the beam is determined using AISC *Manual* Table 3-23, Case 1:

$$M_{max} = \frac{wL^2}{8}$$

The beam plastic moment is determined from AISC *Specification* Equation F2-1:

$$M_p = Z_x F_y \qquad\qquad\qquad\qquad\qquad\qquad\qquad\qquad\qquad\qquad (\textit{Spec.}\ Eq.\ F2\text{-}1)$$

$$= \frac{(73.0\ \text{in.}^3)(50\ \text{ksi})}{12\ \text{in./ft}}$$

$$= 304\ \text{kip-ft}$$

The applied load should exert a maximum moment of 50% of the beam plastic moment capacity at ambient temperature; therefore:

$$w = \frac{8(0.5M_p)}{L^2}$$

$$= \frac{8(0.5)(304\ \text{kip-ft})}{(20\ \text{ft})^2}$$

$$= 3.04\ \text{kip/ft}$$

Use $w = 3$ kip/ft

Step 2—Double-Angle Connection Configuration

Try L5×3½×⅜ angles with $l_{ev} = 1\frac{1}{2}$ in., $l_{eh} = 1\frac{1}{2}$ in. and $s = 2\frac{1}{2}$ in.

From AISC *Specification* Table J3.4, the minimum edge distance, for a ¾-in.-diameter bolts is 1 in.:

$$l_{ev} = 1\frac{1}{2}\ \text{in.} > 1\ \text{in.} \quad \textbf{o.k.}$$

The minimum length of the angles should be greater than half the depth of the beam. The minumum bolt spacing is determined as follows:

$$s = \left(\frac{1}{n-1}\right)\left(\frac{d}{2} - 2l_{ev}\right)$$

$$= \left(\frac{1}{3-1}\right)\left[\frac{16.0\ \text{in.}}{2} - 2(1\frac{1}{2}\ \text{in.})\right]$$

$$= 2\frac{1}{2}\ \text{in.}$$

The horizontal edge distance of the beam is:

$$5\ \text{in.} - 1\frac{1}{2}\ \text{in.} - 0.4\ \text{in.} = 3.10\ \text{in.}$$

Step 3—Check the Beam Strength

Step 3a—Check for beam catenary action

The maximum moment in the beam (at mid-span) is determined using AISC *Manual* Table 3-23, Case 1:

$$\frac{wL^2}{8} = \frac{(3\ \text{kip/ft})(20\ \text{ft})^2}{8}$$

$$= 150\ \text{kip-ft}$$

The beam elastic moment capacity is:

$$K_{yt}F_{yt}S_x = \frac{0.66(50\text{ ksi})(64.7\text{ in.}^3)}{12\text{ in./ft}}$$
$$= 178\text{ kip-ft} > 150\text{ kip-ft}$$

The beam will remain in the elastic zone; no catenary action will occur.

Step 3b—Check beam shear strength

The maximum shear applied on the beam (at the support) is determend using AISC *Manual* Table 3-23, Case 1:

$$V = \frac{wL}{2}$$
$$= \frac{(3\text{ kip/ft})(20\text{ ft})}{2}$$
$$= 30.0\text{ kips}$$

The shear yielding strength of the beam is determined as follows:

$$A_s = dt_w$$
$$= (16.0\text{ in.})(0.305\text{ in.})$$
$$= 4.88\text{ in.}^2$$

$$0.6K_{yt}F_{yt}A_s = 0.6(0.66)(50\text{ ksi})(4.88\text{ in.}^2)$$
$$= 96.6\text{ kips} > 30.0\text{ kips} \quad \textbf{o.k.}$$

Step 4—Determine the Forces on the Connection

Step 4a—Shear force on the connection due to gravity load

The shear force at the connection is determend using AISC *Manual* Table 3-23, Case 1:

$$V = \frac{wL}{2}$$
$$= \frac{(3\text{ kip/ft})(20\text{ ft})}{2}$$
$$= 30.0\text{ kips}$$

Step 4b—Compressive force on the connection due to thermal expansion of the beam

The coefficient of thermal expansion coefficient is:

$$\alpha = 1.2(10^{-5})/°C$$
$$= 6.67(10^{-6})/°F$$

The elongation of the beam due to thermal expansion is:

$$\Delta l = L(\Delta T)(\alpha)$$
$$= (20\text{ ft})(932°F - 68°F)(6.67/°F)(10^{-6})(12\text{ in./ft})$$
$$= 1.38\text{ in.}$$

Because the frame is symmetrical, the horizontal displacement of the column mid-span is:

$$\Delta = \frac{\Delta l}{2}$$

$$= \frac{1.38 \text{ in.}}{2}$$

$$= 0.690 \text{ in.}$$

The column temperature is roughly estimated to be 300°C (572°F) which is 60% of the beam temperature. From Table 3, the value of K_E at 300°C (572°F) is estimated at 0.90. Thus, the thermal compressive force applied to the connection is:

$$\Delta = \frac{PH^3}{48K_E EI_x}$$

Solving for P:

$$P = \frac{48 \Delta K_E EI_x}{H^3}$$

$$= \frac{48(0.690 \text{ in.})(0.90)(29{,}000 \text{ ksi})(272 \text{ in.}^4)}{(20 \text{ ft})^3 (12 \text{ in/ft})^3}$$

$$= 17.0 \text{ kips}$$

Step 4c—Moment applied at the connection

The beam line is a straight line that can be plotted from the moment and end rotation for a fixed-end beam and simply supported beam.

For a simply supported beam:

$$\theta_c = \frac{wL^3}{24K_E EI_x}$$

$$= \frac{(3 \text{ kip/ft})(20 \text{ ft})^3 (12 \text{ in./ft})^2}{24(0.771)(29{,}000 \text{ ksi})(518 \text{ in.}^4)}$$

$$= 0.0124 \text{ rad}$$

$$M = 0 \text{ kip-in.}$$

For a fixed-end beam:

$$\theta_c = 0 \text{ rad}$$

$$M = \frac{wL^2}{12}$$

$$= \frac{(3 \text{ kip/ft})(20 \text{ ft})^2 (12 \text{ in./ft})}{12}$$

$$= 1{,}220 \text{ kip-in.}$$

The beam-line and moment-rotation characteristics (using the stiffness model) of the connection are plotted in Figure 10. The moment applied to the connection is determined at the intersection of these two lines. Use $M = 20.0$ kip-in.

M is used to check the strength of the double-angle connection when subjected to beam-end moments.

Step 5—Compute the Applied Shear Force on the Bolts

The double angle is connected to the beam web by one column of three bolts.

Step 5a—Bolt shear force due to gravity load

$$V_v = \frac{V}{n}$$
$$= \frac{30.0 \text{ kips}}{3 \text{ bolts}}$$
$$= 10.0 \text{ kips/bolt}$$

Step 5b—Bolt shear force due to thermal expansion

$$V_p = \frac{P}{n}$$
$$= \frac{17.0 \text{ kips}}{3 \text{ bolts}}$$
$$= 5.67 \text{ kips/bolt}$$

Step 5c—Bolt shear force due to the applied moment on the connection

$$V_m = \frac{M}{(n-1)s}$$
$$= \frac{20.0 \text{ kip-in.}}{(3-1)(2\frac{1}{2} \text{ in.})}$$
$$= 4.00 \text{ kips/bolt}$$
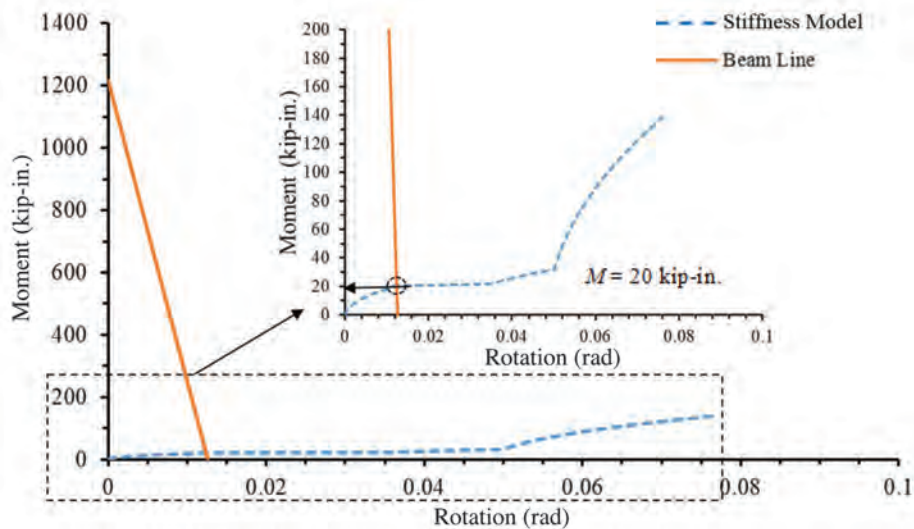
Fig. 10. Moment demand on the double-angle connection using beam-line theory.

Step 5d—Applied shear force on each bolt

$$V_{top} = \sqrt{(V_m - V_p)^2 + (V_v)^2}$$
$$= \sqrt{(4.00 \text{ kips} - 5.67 \text{ kips})^2 + (10.0 \text{ kips})^2}$$
$$= 10.1 \text{ kips}$$

$$V_{middle} = \sqrt{(V_p)^2 + (V_v)^2}$$
$$= \sqrt{(5.67 \text{ kips})^2 + (10.0 \text{ kips})^2}$$
$$= 11.5 \text{ kips}$$

$$V_{bottom} = \sqrt{(V_p + V_m)^2 + (V_v)^2}$$
$$= \sqrt{(4.00 \text{ kips} + 5.67 \text{ kips})^2 + (10.0 \text{ kips})^2}$$
$$= 13.9 \text{ kips}$$

Step 5e—Applied axial force on each tension bolt (connecting the column to the angle)

The compression load applied on each bolt due to the beam thermal expansion is:

$$\frac{P}{6} = \frac{17.0 \text{ kips}}{6}$$
$$= 2.83 \text{ kips/bolt}$$

To obtain the tension applied to the bolts due to the applied moment, the elastic method of distributing forces can be used. The moment applied on each angle is:

$$\frac{M}{2} = \frac{20.0 \text{ kip-in.}}{2}$$
$$= 10.0 \text{ kip-in.}$$

For the system of angle leg in bearing and bolts in tension, the tension applied on the top bolt (critical bolt) due to M is:

$$P_m = \frac{M}{2I_x} A_b p$$
$$= \frac{10.0 \text{ kip-in.}}{17.7 \text{ in.}^4} (0.442 \text{ in.}^2)(5.1 \text{ in.})$$
$$= 1.27 \text{ kips/bolt}$$

$$P_{total} = P_m - \frac{P}{6}$$
$$= 1.27 \text{ kips} - 2.83 \text{ kips}$$
$$= -1.56 \text{ kips/bolt (compression)}$$

Because all the bolts are in compression, there is no need to check the tensile bolt capacity (including prying effects), angle leg in bending, and bolt punching for the double angle.

Step 6—Determine the Angle Leg Strength

Shear applied on each angle leg is:

$$\frac{V}{2} = \frac{30.0 \text{ kips}}{2}$$
$$= 15.0 \text{ kips}$$

The moment applied on each angle leg is:

$$\frac{M}{2} = \frac{20.0 \text{ kip-in.}}{2}$$

$$= 10.0 \text{ kip-in.}$$

Step 6a—Shear yielding

$$A_s = lt$$

$$= (8.00 \text{ in.})(\tfrac{3}{8} \text{ in.})$$

$$= 3.00 \text{ in.}^2$$

$$R_{vy} = 0.6K_{yt}F_{yt}A_s$$

$$= 0.6(0.66)(50 \text{ ksi})(3.00 \text{ in.}^2)$$

$$= 59.4 \text{ kips} > 15.0 \text{ kips} \quad \textbf{o.k.}$$

Step 6b—Shear rupture

$$A_n = [l - n(d + \tfrac{1}{16} \text{ in.})]t_p$$

$$= [8.00 \text{ in.} - 3(\tfrac{13}{16} \text{ in.} + \tfrac{1}{16} \text{ in.})](\tfrac{3}{8} \text{ in.})$$

$$= 2.02 \text{ in.}^2$$

$$R_{vu} = 0.6K_{ut}F_{ut}A_n$$

$$= 0.6(0.64)(65 \text{ ksi})(2.02 \text{ in.}^2)$$

$$= 50.4 \text{ kips} > 15.0 \text{ kips} \quad \textbf{o.k.}$$

Step 6c—Flexural yielding

$$Z_x = \frac{t_p l^2}{4}$$

$$= \frac{(\tfrac{3}{8} \text{ in.})(8.00 \text{ in.})^2}{4}$$

$$= 6.00 \text{ in.}^3$$

$$M_y = K_{yt}F_{yt}Z_x$$

$$= 0.66(50 \text{ ksi})(6.00 \text{ in.}^3)$$

$$= 198 \text{ kip-in.} > 10.0 \text{ kip-in.} \quad \textbf{o.k.}$$

Step 6d—Flexural rupture

The net plastic section modulus is not calculated here. Use $Z_{net} = 3.56 \text{ in.}^3$

$$M_u = K_{ut}F_{ut}Z_{net}$$

$$= 0.64(65 \text{ ksi})(3.56 \text{ in.}^3)$$

$$= 148 \text{ kip-in.} > 10.0 \text{ kip-in.} \quad \textbf{o.k.}$$

Step 6e—Block shear rupture

$$R_n = 0.60A_{nv}K_{ut}F_{ut} + U_{bs}A_{nt}K_{ut}F_{ut} \le 0.60A_{gv}K_{yt}F_{yt} + U_{bs}A_{nt}K_{ut}F_{ut}$$

where

$$A_{nt} = \left[1\tfrac{1}{2}\text{ in.} - 0.5\left(\tfrac{13}{16}\text{ in.} + \tfrac{1}{16}\text{ in.}\right)\right]\left(\tfrac{3}{8}\text{ in.}\right)$$
$$= 0.398\text{ in.}^2$$

$$A_{gv} = \left(5.00\text{ in.} + 1\tfrac{1}{2}\text{ in.}\right)\left(\tfrac{3}{8}\text{ in.}\right)$$
$$= 2.44\text{ in.}^2$$

$$A_{nv} = \left[\left(5.00\text{ in.} + 1\tfrac{1}{2}\text{ in.}\right) - 2.5\left(\tfrac{13}{16}\text{ in.} + \tfrac{1}{16}\text{ in.}\right)\right]\left(\tfrac{3}{8}\text{ in.}\right)$$
$$= 1.62\text{ in.}^2$$

$$U_{bs} = 1.0$$

$$0.60 A_{nv} K_{ut} F_{ut} = 0.60\left(1.62\text{ in.}^2\right)(0.64)(65\text{ ksi})$$
$$= 40.4\text{ kips}$$

$$0.60 A_{gv} K_{yt} F_{yt} = 0.60\left(2.44\text{ in.}^2\right)(0.66)(50\text{ ksi})$$
$$= 48.3\text{ kips}$$

$$U_{bs} A_{nt} K_{ut} F_{ut} = 1.0\left(0.398\text{ in.}^2\right)(0.64)(65\text{ ksi})$$
$$= 16.6\text{ kips}$$

$$R_n = 0.60 A_{nv} K_{ut} F_{ut} + U_{bs} A_{nt} K_{ut} F_{ut} \leq 0.60 A_{gv} K_{yt} F_{yt} + U_{bs} A_{nt} K_{ut} F_{ut}$$
$$= 40.4\text{ kips} + 16.6\text{ kips} < 48.3\text{ kips} + 16.6\text{ kips}$$
$$= 57.0\text{ kips} > 15.0\text{ kips} \quad \textbf{o.k.}$$

Step 7—Check Shear Transfer at Bolts

Step 7a—Bolt shear strength

$$R_v = 0.625 n K_{bt} F_{ub} A_s (2)$$
$$= (0.625)(1)(0.379)(120\text{ ksi})\left[\frac{\pi\left(\tfrac{3}{4}\text{ in.}\right)^2}{4}\right](2)$$
$$= 25.1\text{ kips/bolt}$$

Step 7b—Angle leg bearing and tearout resistance

$$R_{br} = 3.0 K_{ut} F_{ut} d_b t \leq 1.5 l_c t K_{ut} F_{ut}$$
$$= 3.0(0.64)(65\text{ ksi})\left(\tfrac{3}{4}\text{ in.}\right)\left(\tfrac{3}{8}\text{ in.}\right) \leq 1.5(1.06\text{ in.})\left(\tfrac{3}{8}\text{ in.}\right)(0.64)(65\text{ ksi})$$
$$= 24.8\text{ kips/bolt per angle}$$

For the two angles:

$$2R_{br} = 2(24.8\text{ kips/bolt})$$
$$= 49.6\text{ kips/bolt}$$

Step 7c—Beam web bearing and tearout resistance

$$R_{br} = 3.0 K_{ut} F_{ut} d_b t \leq 1.5 l_c t K_{ut} F_{ut}$$
$$= 3.0(0.64)(65\text{ ksi})\left(\tfrac{3}{4}\text{ in.}\right)(0.305\text{ in.}) \leq 1.5(1.66\text{ in.})(0.305\text{ in.})(0.64)(65\text{ ksi})$$
$$= 28.5\text{ kips/bolt}$$

Table 4. Summary of the Limit State Available Strength for a Double-Angle Connection in Fire [500°C (932°F)]	
Mode	**Available Strength**
Shear yielding of angle leg =	59.4 kips
Shear rupture of angle leg =	50.4 kips
Flexural yielding of angle leg =	198 kip-in.
Flexural rupture of angle leg =	148 kip-in.
Block shear of angle leg =	57.0 kips
Bolt shear strength =	25.1 kips/bolt
Angle leg bearing and tearout strength =	24.8 kips/bolt
Beam web bearing and tearout strength =	28.5 kips/bolt

Comparing the strength of the bolts in shear to the angle leg and beam web in bearing and tearout, the bolt in shear has the minimum strength.

$$R_v = \min\{25.1 \text{ kips/bolt}, 49.6 \text{ kips/bolt}, 28.5 \text{ kips/bolt}\}$$
$$= 25.1 \text{ kips/bolt}$$

$V_{top} = 10.1 \text{ kips} < 25.1 \text{ kips}$ **o.k.**

$V_{middle} = 11.5 \text{ kips} < 25.1 \text{ kips}$ **o.k.**

$V_{bottom} = 13.9 \text{ kips} < 25.1 \text{ kips}$ **o.k.**

A summary of the limit state available strength is presented in Table 4. The designed connection can withstand the applied gravity loads at 500°C (932°F), in addition to the exerted moment by the beam on the connection and the compressive forces due to restrained thermal expansion. Further details of the final geometric configuration of the double-angle connection are given in Figure 11.
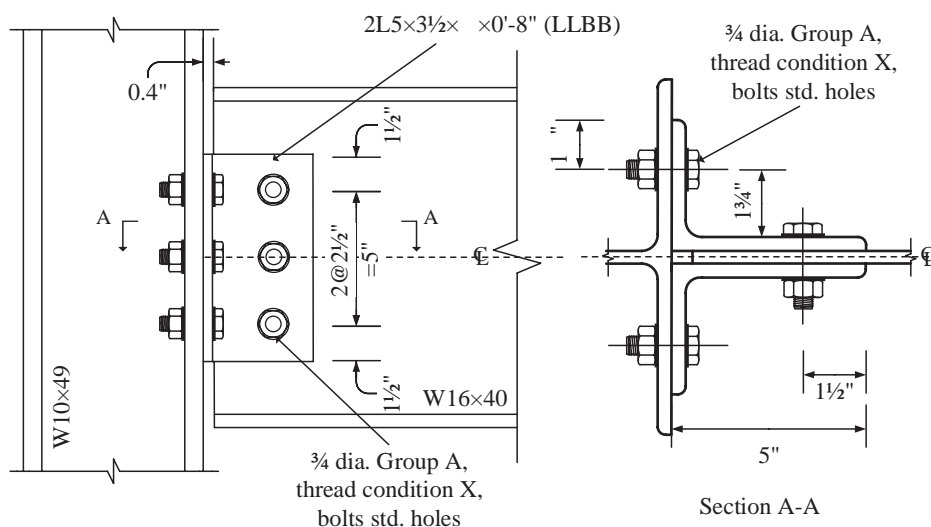

Fig. 11. Detailed design for W16×40 beam connected to W10×49 column through a double-angle connection.

CONCLUSIONS

The goal of this study is to propose fire design–oriented guidelines that aim at designing robust simple steel connections (shear tab and double angle) at low to medium temperatures of fire. To reach this aim, first, a simple tool, which can be used by professional structural fire engineers, is developed to characterize the stiffness and capacity of simple steel connections in fire. Thus, a stiffness-based model, which is considered to be a simple and practical tool, is proposed. The developed model is based on stiffness and strength equations available in the literature. Materials and geometric nonlinearities are incorporated in the proposed model to ensure accurate predictions of the connection response. Geometric nonlinearity can be observed through the complex interaction between connection components by surface to surface contact and slip of shear planes, whereas material nonlinearity is included through material yielding and steel retention factors. The proposed model is validated against experimental data available in the literature to test its prediction capabilities. It is able to capture—with reasonable accuracy—the force-rotation behavior of the connections when compared with the experimental results. Further, the ultimate capacities and failure modes from the experimental work results are identified and well predicted.

The study further incorporates the proposed stiffness model in fire design procedure of unprotected simple steel connections under transient-state conditions of fire. The design procedure is presented in two fire design examples illustrated as step-by-step design guidelines for simple steel connections. It accounts for the three main sources of stresses on the steel connections in fire: (1) the sustained gravity loads, (2) the induced axial load due to restrained thermal expansion, and (3) the moment demand exerted by the beam material (stiffness) degradation. Simplifications are identified and implemented to reach a simple and conservative design procedure to be used by professional structural fire engineers. Comparing the two design examples, it can be concluded that the double-angle connection exhibits a better performance than the shear tab connection when subjected to fire. The fact that the double-angle connection provides double shear planes to resist the applied loads, compared to one shear plane in the shear tab connection, makes it more flexible and resilient when subjected to fire. This is consistent with previous findings in the literature (Hantouche et al., 2016). Moreover, this study showed that the bolts are the most vulnerable element in the connection during fire, especially for shear tab connections with a single shear plane. This was also observed in the fire tests of Yu et al. (2009a, 2009c), where the failure mode was governed by shear bolt failure at high temperatures. This can be attributed to the severe reduction in the bolt ultimate strength (e.g., relatively low retention factor) when exposed to fire. Therefore, in such cases, it is advised to use A490-X bolts to increase the strength and ductility of simple steel connections. The bolts in steel connection should be given exceptional care in both design and construction phases.

This study should be extended to cover other aspects and load demands that the simple steel connections are subjected to at later stages (high temperatures) of fire—most importantly, tension stresses due to beam catenary action. Studies should be also conducted to ensure the survival of the connection during cooling phase where the connection is subjected to additional tension stresses. Moreover, the design of connections surrounded by a cooler structure in a full building system should be also considered. Creep material should be accounted for in the fire design to include the time-dependent effects. It is noteworthy that quite a bit of ongoing research is proving that steel connections and beams can survive fire events without having fire protection (insulation). These findings will eventually lead to establishing both safe and economic design of steel structures.

SYMBOLS

A_b	Effective area of the bolt shank, in.^{2}
A_f	Effective contact area of the beam, in.^{2}
A_{gv}	Gross area subject to shear for block shear failure mode, in.^{2}
A_{nt}	Net area subject to tension for block shear failure mode, in.^{2}
A_{nv}	Net area subject to shear for block shear failure mode, in.^{2}
A_s	Effective shear area (e.g. web area in beams), in.^{2}
A_{we}	Effective area of the weld, in.^{2}
D	Distance between the beam bottom flange and the center of rotation c, in.
D_u	Ratio of the mean installed bolt pretension to the specified minimum bolt pretension
E	Elastic modulus of steel material at ambient temperature, ksi
F_{EXX}	Filler metal classification strength at ambient temperature, ksi
F_{ub}	Ultimate strength of steel bolt at ambient temperature, ksi
F_{ut}	Ultimate strength of base material at ambient temperature, ksi
F_{yt}	Yield strength of base material at ambient temperature, ksi

H	Column height, ft	R_t	Bolt tensile resistance, kips
I_x	Moment of inertia about the x-axis, in.^{4}	S_x	Elastic section modulus about the x-axis, in.^{3}
K_E	Temperature-dependent retention factor for the elastic modulus of the base material	T_b	Minimum pretension force applied on the bolt, kips
K_{bt}	Temperature-dependent retention factor for the ultimate strength of steel bolt	U_{bs}	Tension stress distribution factor
K_{ut}	Temperature-dependent retention factor the ultimate strength of the base material	V	Applied shear force on the connection, kips
K_{wt}	Temperature-dependent retention factor for the ultimate strength of the weld	V_{bottom}	Applied shear force on the bottom bolt, kips
K_{yt}	Temperature-dependent retention factor the yield strength of the base material	V_m	Bolt shear forces due to applied moment, kips
L	Length of the beam, ft	V_{middle}	Applied shear force on the middle bolt, kips
L_b	Elongation length of the bolt shank, in.	V_p	Bolt shear forces due to compressive force, kips
L_{eh}	Horizontal edge distance, in.		
L_{ev}	Vertical edge distance, in.	V_{top}	Applied shear force on the top bolt, kips
M	Resultant moment on the connection calculated from applied shear and tensile forces, kip-in.	V_v	Bolt shear forces due to gravity load, kips
		W	Applied uniformly distributed gravity load on the beam, kip/ft
M_p	Plastic moment capacity, kip-in.	Z_{net}	Net plastic section moduli about the x-axis, in.^{3}
M_u	Rupture moment capacity, kip-in.		
M_y	Yielding moment capacity, kip-in.	Z_x	Plastic section moduli about the x-axis, in.^{3}
P	Axial force due to thermal expansion of the beam, kips	a	Distance from the bolt line to the weld line, in.
P_m	Axial force due to applied moment, kips	d_{M16}	Diameter of M16 bolt shank, in.
P_{total}	Total axial force, kips	d_b	Diameter of bolt shank, in.
R_b	Capacity of angle leg in bending, kips	d_h	Diameter of bolt hole, in.
R_{br}	Strength of plate/angle leg/beam web in bearing/tearout, kips	d_m	Mean of the across points and across flats dimensions of the bolt head or the nut, whichever is smaller, in.
R_{bs}	Shear resistance of plate/angle leg against block shear, kips	e	Shear force eccentricity, in.
R_{nw}	Weld strength, kips	e_b	Distance from the bolt to the free edge of the plate in the direction of the load transfer, in.
R_{pn}	Shear resistance of plate/angle leg against bolt punching rupture, kips		
R_s	Bolt slip resistance, kips	f_t	Shear stress perpendicular and parallel to the weld line, ksi
R_v	Bolt shear resistance, kips	f_v	Shear stress parallel to the weld line, ksi
R_{vu}	Shear resistance of plate/angle leg against shear rupture, kips	h	Distance between the end components connecting shear tab/double angle to column, in.
R_{vy}	Shear resistance of plate/angle leg against shear yielding, kips		
		h_f	Factor of fillers

k_{ab}	Stiffness of the web angle in bending, kip/in.
k_b	Parameter as defined in Equation 4
k_{bcc}	Stiffness of the beam flange in contact with the column, kip/in.
$k_{beam\text{-}angle\ lapjoint}$	Stiffness of a double-lap joint in double-angle connections, kip/in.
$k_{bolt\ row}$	Stiffness of a single bolt row, kip/in.
k_{bs}	Stiffness of the bolts in shear, kip/in.
k_{bt}	Stiffness of the bolts in tension, kip/in.
k_{pb}	Stiffness of beam web/angle leg in bearing, kip/in.
k_r	Rotational stiffness, kip-in.
k_r	Parameter as defined in Equation 5
k_{tb}	Stiffness of steel plates in bearing, kip/in.
l_c	Clear distance between the edge of the bolt hole and the edge of the material, in.
$l_{eff,ab}$	Effective length of the double angles in bending in each bolt-row, in.
m	Distance between the center of the bolt and the angle leg fillet, in.
n	Number of slip/shear planes
n_b	Number of bolt columns
p	Distance between the farthest bolt-row and center of rotation c, in.
p_b	Spacing of the bolt in the direction of the load transfer, in.
s	Setback distance, in.
s_{slip}	Sum of the gaps between the bolt shank and the edge of the bolt hole, in.
t	Thickness of shear tab plate, double-angle leg, or beam web, in.
Δ	Horizontal deflection at the mid-span of the column due to beam thermal expansion, in.
ΔT	Change in temperature, °F
Δl	Thermal elongation of the heated beam, in.
Ω	Temperature-dependent parameter defined by Yu et al. (2009c)
α	Coefficient of thermal expansion of steel, °F

θ	Angle between the line of action of the required force and the weld longitudinal axis, degrees
θ_c	Connection rotation, rad
$\theta_{beam\text{-}contact}$	Angle of contact between the beam flange and the column flange, rad
$\theta_{bolt\text{-}contact}$	Angle at which the farthest bolt comes in contact with respective bolt hole edge, rad
μ	Mean slip coefficient

ACKNOWLEDGMENTS

REFERENCES

AISC (2016), *Specification for Structural Steel Buildings*, ANSI/AISC 360-16, American Institute of Steel Construction, Chicago, Ill.

AISC (2017), *Steel Construction Manual*, 15th Ed., American Institute of Steel Construction, Chicago, Ill.

CEN (2005a), *Eurocode 3: Design of Steel Structures—Part 1–2: General Rules—Structural Fire Design*, European Committee for Standardization, Brussels.

CEN (2005b), *Eurocode 3: Design of Steel Structures—Part 1–8: Design of Joints*, European Committee for Standardization, Brussels.

Garlock, M.E. and Selamet, S. (2010), "Modeling and Behavior of Steel Plate Connections Subject to Various Fire Scenarios," *Journal of Structural Engineering*, ASCE, Vol. 136, No. 7, pp. 897–906.

Hantouche, E.G., Abboud, N.H., Morovat, M.A., and Engelhardt, M.D. (2016), "Analysis of Steel Bolted Double Angle Connections at Elevated Temperatures," *Fire Safety Journal*, Vol. 83, pp. 79–89.

Hu, G. and Engelhardt, M. (2012), "Studies on the Behavior of Steel Single-Plate Beam End Connections in a Fire," *Structural Engineering International*, Vol. 22, No. 4, pp. 462–469.

Hu, Y., Davison, J.B., Burgess, I.W., and Plank, R.J. (2007), "Comparative Study of the Behaviour of BS 4190 and BS EN ISO 4014 Bolts in Fire," *Proceedings, 3rd International Conference on Steel and Composite Structures*, Taylor & Francis, Manchester, England, pp. 587–592.

Lee, J., Morovat, M.A., Hu, G., Engelhardt, M.D., and Taleff, E. (2013), "Experimental Investigation of Mechanical Properties of ASTM A992 Steel at Elevated Temperatures," *Engineering Journal*, AISC, Vol. 50, No. 4, pp. 249–272.

Pakala, P., Kodur, V., Selamet, S., and Garlock, M. (2012), "Fire Behavior of Shear Angle Connections in a Restrained Steel Frame," *Journal of Constructional Steel Research*, Vol. 77, pp. 119–130.

Seif, M., Main, J., Weigand, J., McAllister, T.P., and Luecke, W. (2016), "Finite Element Modeling of Structural Steel Component Failure at Elevated Temperatures," *Structures*, Vol. 6, pp. 134–145.

Seif, M.S., Main, J.A., and McAllister, T.P. (2013), "Performance of Steel Shear Tab Connections at Elevated Temperatures," *Proceedings of the Annual Stability Conference*, *Structural Stability Research Council*, St. Louis, Mo., pp. 16–20.

Selamet, S., and Garlock, M.E. (2010), "Robust Fire Design of Single Plate Shear Connections," *Engineering Structures*, Vol. 32, pp. 2,367–2,378.

Sunder, S. (2005), "Final Report on the Collapse of the World Trade Center Towers: Federal Building and Fire Safety Investigation of the World Trade Center Disaster," National Institute of Standards and Technology.

University of Sheffield (2007), EPSRC Project EP/C510984/1: Robustness of Joints in Fire, 2005–2008, http://fire-research.group.shef.ac.uk/downloads.html.

Wald, F., Simões da Silva, L., Moore, D.B., Lennon, T., Chladná, M., Santiago, A., Beneš, M., and Borges, L. (2006), "Experimental Behaviour of a Steel Structure under Natural Fire," *Fire Safety Journal*, Vol. 41, No. 7, pp. 509–522.

Wang, Y.C., Dai, X.H., and Bailey, C.G. (2011), "An Experimental Study of Relative Structural Fire Behaviour and Robustness of Different Types of Steel Joint in Restrained Steel Frames," *Journal of Constructional Steel Research*, Vol. 67, No. 7, pp. 1,149–1,163.

Wuwer, W., Zamorowski, J., and Swierczyna, S. (2012), "Lap Joints Stiffness According to Eurocode EC3 and Experimental Investigations Results," *Archives of Civil and Mechanical Engineering*, Vol. 12, No. 1, pp. 95–104.

Yu, H., Burgess, I.W., Davison, J.B., and Plank, R.J. (2009a), "Tying Capacity of Web Cleat Connections in Fire, Part 1: Test and Finite Element Simulation," *Engineering Structures*, Vol. 31, No. 3, pp. 651–663.

Yu, H., Burgess, I.W., Davison, J.B., and Plank, R.J. (2009b), "Tying Capacity of Web Cleat Connections in Fire, Part 2: Development of Component-Based Model," *Engineering Structures*, Vol. 31, No. 3, pp. 697–708.

Yu, H., Burgess, I.W., Davison, J.B., and Plank, R.J. (2009c), "Experimental Investigation of The Behaviour of Fin Plate Connections in Fire," *Journal of Constructional Steel Research*, Vol. 65, No. 3, pp. 723–736.

Zhang, C., and Usmani, A. (2015), "Heat Transfer Principles in Thermal Calculation of Structures in Fire," *Fire Safety Journal*, Vol. 78, pp. 85–95.

An Experimental Study of the Influence of Eccentricity on Shear Lag Effects in Welded Connections

KENNETH L. ORLOFF, JAMES A. SWANSON, GIAN ANDREA RASSATI, and THOMAS M. BURNS

ABSTRACT

In the 2010 AISC *Specification*, the shear lag factor for longitudinally welded tension members was applicable only to plate-type members having equal length welds on each side with a minimum length equal to the distance between the welds (AISC, 2010). Fortney and Thornton (2012) used experimental data from three previous research programs consisting of 175 various tension members to develop a generalized shear lag model that addresses the aforementioned limitations. The members comprising this dataset consisted of 158 flat plates with equal weld lengths, 4 single angles with unequal but balanced weld lengths, and 13 other members having equal weld lengths. The shear lag factor presented in the 2016 AISC *Specification* Table D3.1, Case 4 (AISC, 2016b) is a product of Fortney and Thornton's work and applies to longitudinally welded plates, angles, channels, tees, and W-shapes having equal or unequal lengths and no length-to-width limitation. This paper presents an experimental study on the shear lag effects in longitudinally welded tension members under both in-plane and out-of-plane eccentricity through the testing of eight 3×½ plate sections and twelve 3×3×½ single-angle sections having both equal and unequal longitudinal weld lengths. Experimental shear lag factors were determined for each of the 20 tested specimens and compared to three theoretical values: (1) the shear lag factor in the 2010 AISC *Specification* (AISC, 2010), (2) the shear lag factor based on a bi-planar model (Fortney and Thornton, 2012), and (3) the shear lag factor from Case 4 in the 2016 AISC *Specification*. The findings of this experimental study confirm that shear lag factor given by Case 4 in the 2016 AISC *Specification* provides the best prediction of shear lag factors in welded connections subject to both in-plane and out-of-plane eccentricity.

KEYWORDS: Shear lag, angle, eccentric, tension member.

INTRODUCTION

Tension members are an efficient way to transfer stress from one point to another in a structure and are commonly found in bridge and roof trusses, wind bracing systems in buildings, cables in bridges, and rods in suspended roof systems. In order to successfully transfer stress from one member to another, tension members must be adequately connected using bolts or welds. Should the bolts or welds have sufficient strength, there are three limit states that may control the strength of a tension member: yielding of the gross section, fracture of the net section at the connection, and block shear fracture at the connection (Salmon et al., 2009). Gross section yielding is considered a limit state because it could lead to excessive elongation of the member while net section fracture and block shear fracture are considered limit states because the member would no longer be able to carry load. Net section fracture of a welded connection depends on the cross-sectional element being used as the tension member and on the connection details.

The design provisions for longitudinally welded tension members are located in Chapter D of the 2016 *Specification for Structural Steel Buildings* (AISC, 2016b), hereafter referred to as the AISC *Specification*. The design tensile strength, ϕP_n, and the allowable tensile strength, P_n/Ω, of a tension member is the lower value obtained when considering the limit states of tensile yielding in the gross section and tensile rupture in the net section. The nominal tensile strength of a tension member is as follows:

For tensile yielding in the gross section, the nominal tensile strength is:

$$P_n = F_y A_g \tag{1}$$

For tensile rupture in the net section, the nominal tensile strength is:

$$P_n = F_u A_e \tag{2}$$

The effective net area of the tension member, A_e, is determined as:

$$A_e = A_n U \tag{3}$$

Kenneth L. Orloff, The Dwyer Company Inc., Cincinnati, Ohio. Email: korloff@thedwyercompany.com

James A. Swanson, Associate Professor, Department of Civil and Architectural Engineering and Construction Management, University of Cincinnati, Cincinnati, Ohio. Email: james.swanson@uc.edu (corresponding)

Gian Andrea Rassati, Associate Professor, Department of Civil and Architectural Engineering and Construction Management, University of Cincinnati, Cincinnati, Ohio. Email: gian.rassati@uc.edu

Thomas M. Burns, Adjunct Professor, Department of Civil and Architectural Engineering and Construction Management, University of Cincinnati, Cincinnati, Ohio. Email: burnstm@ucmail.uc.edu

where
A_g = gross area of the member, in.^{2}
A_n = net area of the member, in.^{2}
U = shear lag reduction coefficient

AISC *Specification* Table D3.1 provides shear lag factors for various cases. Because this experimental study focused on the effect that eccentricity has on shear lag factors, Case 4 as listed in the table is of prime interest, as shown in Figure 1.
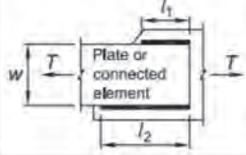
BACKGROUND

The Shear Lag Effect

The shear lag effect is the nonuniform stress distribution that occurs in a tension member adjacent to a connection. The total shear lag effect is a combination of both in-plane effects and out-of-plane effects. The in-plane shear lag effect is a function of the connection length and width of the connected element, while the out-of-plane effect occurs when not all of the elements of a cross section are directly connected, such as when an angle is used as a tension member and only one leg of the angle is connected, as shown in Figure 2. Eccentrically loaded members will experience a nonuniform stress distribution across the width of the member. Shear stresses acting in the plane of the member transmit stress from the location of the applied load to locations distant from the load (Salmon et al., 2009). The shear transfer "lags" behind at locations farther away from the applied load (Salmon et al., 2009). As a result of the shear lag effect, the design strength of the member must be reduced (Easterling and Giroux-Gonzalez, 1993). The shear lag factor, U, is a reduction coefficient that is multiplied by the net area to determine the effective net area for the limit state of net section fracture.

Shear lag provisions for welded members were first introduced in the *Load and Resistance Factor Design Specification for Structural Steel Buildings* (AISC, 1986) and

Case	Description of Element	Shear Lag Factor, U	Example
4[a]	Plates, angles, channels with welds at heels, tees, and W-shapes with connected elements, where the tension load is transmitted by longitudinal welds only.	$U = \dfrac{3l^2}{3l^2 + w^2}\left(1 - \dfrac{\bar{x}}{l}\right)$	

[a] $l = \dfrac{l_1 + l_2}{2}$, where l_1 and l_2 shall not be less than 4 times the weld size.

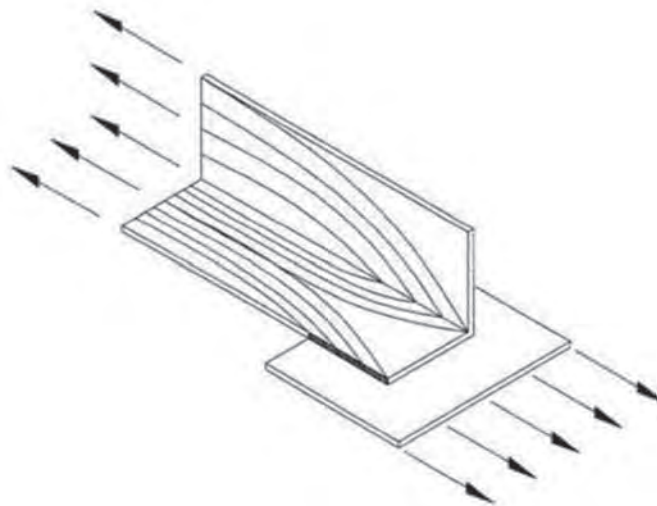Fig. 1. AISC shear lag factor provision for Case 4 (AISC, 2016b).

Fig. 2. Stress distribution in an angle section in tension (Mannem, 2002).

Specification for Structural Steel Buildings—Allowable Stress Design and Plastic Design (AISC, 1989). These provisions addressed only plate-type members having no eccentricity.

Shear Lag Provisions

As previously mentioned, shear lag provisions for tension members connected by longitudinal welds first appeared in the AISC *Load and Resistance Factor Design Specification for Structural Steel Buildings* (AISC, 1986). Determination of the shear lag factor for a variety of cases was tabulated in 2005 AISC *Specification* Table D3.1 (AISC, 2005), with Case 2 addressing out-of-plane eccentricity and Case 4 addressing the shear lag factor for flat plates where the tension load is transmitted by longitudinal welds only. The shear lag provisions for Case 2 and Case 4 in the subsequent 2010 AISC *Specification* (AISC, 2010), as shown in Figure 3, were virtually identical to the 2005 *Specification*.

A task group was assigned by the AISC Committee on Specifications to evaluate Table D3.1 of the AISC *Specification* (Fortney and Thornton, 2012). Fortney and Thornton described four limitations in Case 4:

1. Only plates are considered.

2. Both edges of the plate must be welded.

3. The welds must be of equal length.

4. The length of the welds, or the average thereof, must be equal to or greater than the distance between them.

During their review of Case 4, Fortney and Thornton (2012) evaluated a generalized procedure for calculating the shear lag factor in connections using longitudinal welds that included not only plate-type tension members, but also those consisting of angles, channels, and WT sections.

Fortney and Thornton (2012) reviewed past experimental research in order to investigate shear lag effects. Three experimental research programs, consisting of 175 longitudinally welded tension members, were evaluated in their study. The dataset used consisted of 158 flat plates with equal weld lengths; 4 single angles with unequal but balanced weld lengths; and 13 other members, including double angles, tees, and channels having equal weld lengths. One of the major findings was that a larger strength reduction existed in experimental data compared to the calculated value using the 2010 AISC *Specification*. They concluded that this might be a result of the in-plane shear lag effect due to the connection length not being considered in members with eccentricity. As a result, two recommendations were proposed that take into account both in-plane and out-of-plane effects to accurately predict the shear lag factor. The first recommendation, the bi-planar model, uses the product of the out-of-plane effect and the in-plane effect of Table D3.1 for the calculation of the shear lag factor (Figure 4).

In Fortney and Thornton's second recommendation, the out-of-plane effect is accounted for by using Case 2 of AISC *Specification* Table D3.1 (AISC, 2010), while the in-plane effect is accounted for by a fixed-fixed beam model. The moment-axial interaction equation of AISC *Specification* Section H1.1 (AISC, 2010) was used along with the assumption of a fixed-fixed beam with a uniformly distributed load along its length and plastic hinges forming at locations of maximum positive and negative moments. Using the conservative approximation of $F_u/F_y = 1.5$, the in-plane shear lag effect for the connected element in the second recommendation is shown in Equation 4. Figure 5 details this recommendation for Case 4 proposed by Fortney and Thornton (2012), which was incorporated in equivalent form into the 2016 *Specification*.

$$U_{CE} = \frac{1}{1 + \left(\frac{1}{3}\right)\left(\frac{w}{l}\right)^2} \tag{4}$$
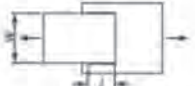
Case	Description of Element	Shear Lag Factor, *U*	Example
2	All tension members, except plates and HSS, where the tension load is transmitted to some but not all of the cross sectional elements by fasteners or longitudinal welds or by longitudinal welds in combination with transverse welds.	$U = 1 - \dfrac{\bar{x}}{l}$	
4	Plates where the tension load is transmitted by longitudinal welds only.	$l \geq 2w$ .... $U = 1.0$ $2w > l \geq 1.5w$ .... $U = 0.87$ $1.5w > l \geq w$ .... $U = 0.75$	

Fig. 3. 2010 AISC shear lag factor provision for welded tension members (AISC, 2010).

where

U_{CE} = shear lag factor of the connected element

l = length of the weld, in.

w = width of the plate/element, in.

The fixed-fixed beam model developed by Fortney and Thornton (2012) is now used in 2016 AISC *Specification* Table D3.1, Case 4. The current Case 4 shear lag factor removes previous limitations by accommodating weld lengths shorter than the width of the member, conditions using unequal weld lengths, and members besides flat plates.

EXPERIMENTAL PROGRAM

Research was conducted at the University of Cincinnati to study the influence of both in-plane and out-of-plane eccentricity on shear lag. The project consisted of the experimental testing of 20 longitudinally welded tension specimens consisting of eight 3×½ plates and twelve 3×3×½ angles. The specimens were ordered as ASTM A36 material and were designed assuming a yielding strength of 50 ksi and an ultimate strength of 70 ksi. The main parameters that were varied included the length of the connection and the weld configuration. Material testing was also performed to determine the actual yield and ultimate stresses of the material. Shear lag factors resulting from these tests were evaluated
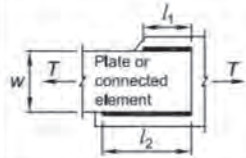
for their conformance to theoretical values given by 2016 AISC *Specification* Table D3.1, Case 4. The experimental shear lag factors resulting from these 20 tests were also compared to the AISC bi-planar model from Fortney and Thornton (2012), as well as the theoretical shear lag values from Case 4 in the 2010 AISC *Specification* (AISC, 2010).

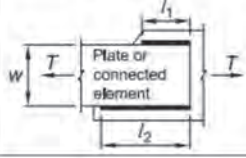### Description of the Tensile Specimens

Eight 3×½ plate specimens and twelve 3×3×½ angle specimens were tested using a Tinius Olsen testing machine with a capacity of 400 kips. The configuration details of the plate specimens (Group A) and the angle specimens (Group C) are shown in Figures 6 and 7 as well as Tables 1 and 2, respectively. The clear length of all specimens was 36 in. The joint at gusset plate #1 was designed to fail, while the joint at gusset plate 2 was intended to be stronger than the connected members. Specimen C-11 was originally detailed with a transverse weld at gusset #1 (L_B = 3 in.) but the specimen was fabricated without the transverse weld. As a result, Specimen C-11 was identical to Specimen C-6.

The universal testing machine used a displacement-controlled loading at a rate of 0.125 in./min. until the yield plateau was observed. After a couple tenths of an in. of displacement in the yield plateau, the rate of loading was increased to 0.25 in./min. Each specimen was tested until failure. The experimental setup is shown in Figure 8. Each

Case	Description of Element	Shear Lag Factor, U	Example
4[a]	Plates, angles, channels, tees, and W-shapes with connected elements where the tension load is trans-mitted by longitudinal welds only.	$U = U_{CE}\left(1 - \dfrac{\bar{x}}{l}\right)$ $l \geq 2w$ .... $U_{CE} = 1.0$ $2w > l \geq 1.5w$ .... $U_{CE} = 0.87$ $1.5w > l \geq w$ .... $U_{CE} = 0.75$ $w > l$ .... $U_{CE} = 0.75(l/w)$	

[a] $l = \dfrac{l_1 + l_2}{2}$, where l_1 and l_2 shall not be less than 4 times the weld size.

Fig. 4. Fortney and Thornton's (2012) bi-planar model—first recommendation.

Case	Description of Element	Shear Lag Factor, U	Example
4[a]	Plates, angles, channels, tees, and W-shapes with connected elements where the tension load is trans-mitted by longitudinal welds only.	$U = U_{CE}\left(1 - \dfrac{\bar{x}}{l}\right)$ $U_{CE} = \dfrac{1}{1 + \left(\frac{1}{3}\right)\left(\frac{w}{l}\right)^2}$	

[a] $l = \dfrac{l_1 + l_2}{2}$, where l_1 and l_2 shall not be less than 4 times the weld size.

Fig. 5. Fortney and Thornton's (2012) fixed-fixed beam model—second recommendation.

Table 1. Group A Plate Specimen Details								
Specimen	w_1	L_A	L_B	L_C	w_2	L_D	L_E	L_F
PL3×½	(in.)	(in.)	(in.)	(in.)	(in)	(in.)	(in.)	(in.)
A-1	5⁄16	8	0	8	5⁄16	10	0	10
A-2a	5⁄16	6	0	6	5⁄16	8	0	8
A-2b	7⁄16	6	0	6	5⁄16	8	0	8
A-3	3⁄8	4	0	4	5⁄16	6	0	6
A-4	7⁄16	2	0	2	5⁄16	4	0	4
A-5	5⁄16	4	0	8	5⁄16	10	0	10
A-6	3⁄8	3	0	6	5⁄16	8	0	8
A-7	7⁄16	2	0	4	5⁄16	6	0	6

specimen was installed into the universal testing machine with the end expected to fail (i.e., gusset 1) at the bottom. Both gusset plates were gripped at their ends using mechanical grips, and shims were used in order to align the centroid of the member with the applied load. Two linear variable differential transformers (LVDTs) were attached to a plate and clamped to the specimen above and below the bottom welded connection. Also, an aluminum angle was clamped to the specimen below the top gusset plate. Monofilament was used to suspend the rods of the LVDTs from hooks attached to the aluminum angle. Rubber pads were used between the clamps and the specimen to ensure the clamps would stay snug despite the specimen becoming thinner due to Poisson effects. Load and displacement data was collected by a National Instruments data acquisition system and exported to Excel. Displacement data was also collected by the LVDTs in order to determine the elongation of the bottom welded connection. The average displacement of the top two LVDTs was subtracted from the average displacement of the bottom two LVDTs in order to determine the connection elongation. The maximum load for each specimen was found and used for the shear lag analysis.
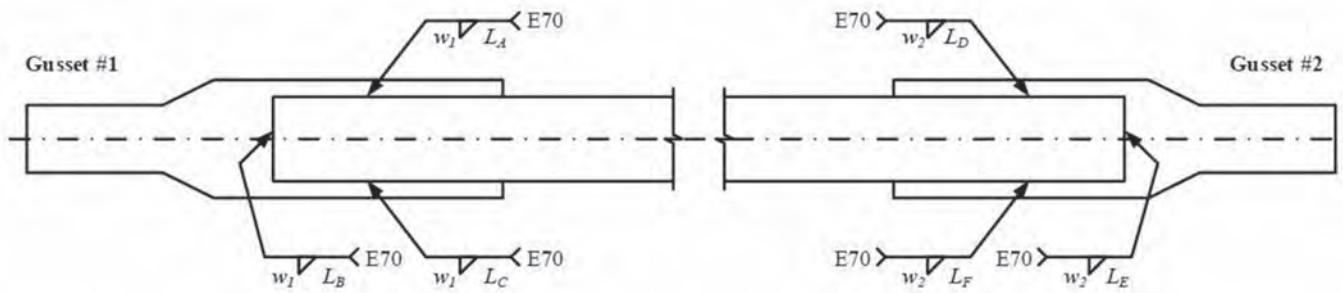

Fig. 6. Group A plate specimen.
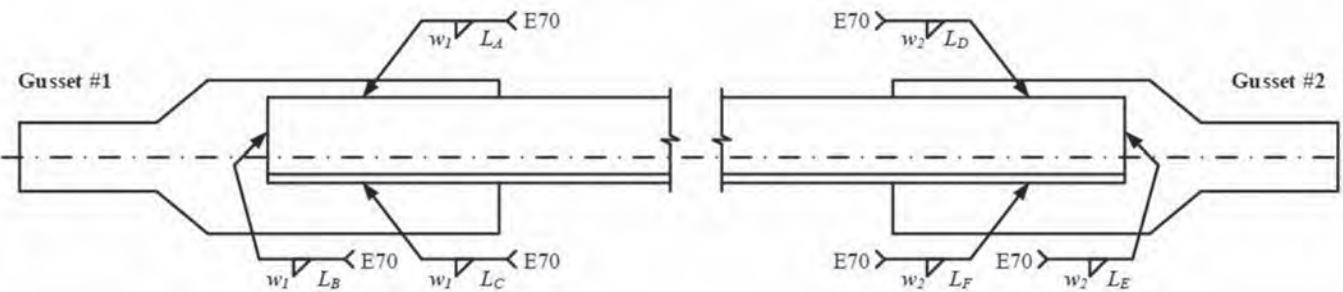
Fig. 7. Group C angle specimen.

Table 2. Group C Angle Specimen Details								
Specimen	w_1	L_A	L_B	L_C	w_2	L_D	L_E	L_F
L3×3×½	(in.)	(in.)	(in.)	(in.)	(in)	(in.)	(in.)	(in.)
C-1	⅜	8	0	8	⁵⁄₁₆	10	0	10
C-2	⁷⁄₁₆	6	0	6	⁵⁄₁₆	10	0	10
C-3	⁷⁄₁₆	4	0	4	⁵⁄₁₆	10	0	10
C-4	⁷⁄₁₆	2	0	2	⁵⁄₁₆	6	0	6
C-5	⁷⁄₁₆	4	0	8	⁵⁄₁₆	10	0	10
C-6	⁷⁄₁₆	3	0	6	⁵⁄₁₆	8	3	8
C-7a	⁷⁄₁₆	1.5	0	3	⁵⁄₁₆	5	3	5
C-7b	⁷⁄₁₆	1.5	0	3	⁵⁄₁₆	5	3	5
C-8	⁷⁄₁₆	3	0	1.5	⁵⁄₁₆	5	3	5
C-9	⁷⁄₁₆	6	0	3	⁵⁄₁₆	8	3	8
C-10	⁷⁄₁₆	8	0	4	⁵⁄₁₆	10	0	10
C-11	⁷⁄₁₆	3	0	6	⁵⁄₁₆	8	3	8

Material Testing

Two steel coupons were machined and tested for both the plate and angle material provided by the fabricator. The plate and angle material coupons are designated with the letters A and C, respectively. The actual measured yield and ultimate stresses for both the plate and angle material are shown in Table 3. Note that the measured ultimate strength reached values well above 70 ksi.

EXPERIMENTAL RESULTS

The 20 longitudinally welded tension specimens experienced one of three different failure modes—a gross section failure (GSF), a net section failure (NSF), or a weld failure (WF), as shown in Table 4. Pictures of a typical failure for each mode are shown in Figures 9, 10, and 11. The specimens were originally detailed such that the welds would be stronger than the members. Despite the fact that

Fig. 8. Experimental setup of tension specimen.

Table 3. Results of Material Testing										
Coupon	Yield		Ultimate			Coupon	Yield		Ultimate	
	Load	Stress	Load	Stress			Load	Stress	Load	Stress
	(kips)	(ksi)	(kips)	(ksi)			(kips)	(ksi)	(kips)	(ksi)
A-1	10.38	53.47	15.03	77.43		C-1	10.14	51.80	14.58	74.52
A-2	10.35	53.35	15.02	77.44		C-2	10.08	51.92	14.49	74.67
Avg.	10.37	53.41	15.03	77.44		Avg.	10.11	51.86	14.54	74.60

Fig. 9. Typical gross section fracture.
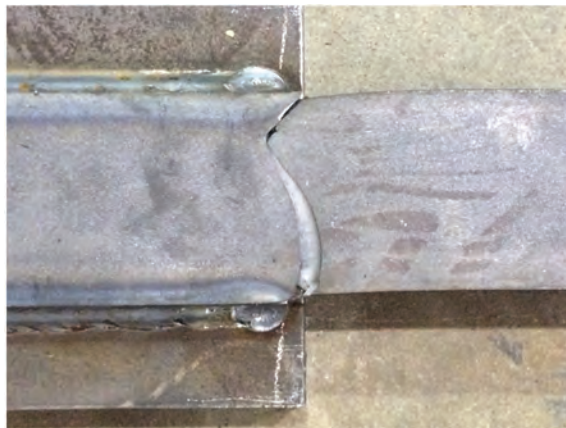
Fig. 10. Typical net section fracture.

(a)	*(b)*

Fig. 11. Typical weld failures.

Table 4. Experimental Results						
Specimen	Failure Mode	A_g	F_y	F_u	Max Load	Experimental Shear Lag Factor, U_e
		(in.²)	(ksi)	(ksi)	(kips)	
A-1	GSF	1.50	53.4	77.4	111	0.96
A-2a	GSF	1.50	53.4	77.4	107	0.92
A-2b	GSF	1.50	53.4	77.4	107	0.92
A-3	GSF	1.50	53.4	77.4	107	0.92
A-4	WF	1.50	53.4	77.4	72.4	> 0.62
A-5	GSF	1.50	53.4	77.4	111	0.96
A-6	NSF	1.50	53.4	77.4	111	0.95
A-7	WF	1.50	53.4	77.4	102	> 0.87
C-1	NSF	2.76	51.9	74.6	196	0.95
C-2	WF	2.76	51.9	74.6	181	> 0.88
C-3	WF	2.76	51.9	74.6	115	> 0.56
C-4	WF	2.76	51.9	74.6	73.6	> 0.36
C-5	NSF	2.76	51.9	74.6	187	0.91
C-6	WF	2.76	51.9	74.6	156	> 0.76
C-7a	WF	2.76	51.9	74.6	86.5	> 0.42
C-7b	WF	2.76	51.9	74.6	90.3	> 0.44
C-8	WF	2.76	51.9	74.6	83.6	> 0.41
C-9	WF	2.76	51.9	74.6	127	> 0.62
C-10	WF	2.76	51.9	74.6	179	> 0.87
C-11	WF	2.76	51.9	74.6	157	> 0.76

expected material strengths, $R_yF_y = (1.5)(36) = 54$ ksi and $R_tF_u = (1.2)(58) = 70$ ksi, consistent with the AISC *Seismic Provisions* (2016a), were used for the members in the design calculations, two of the plate specimens and all but two of the angle specimens exhibited failures in the welds instead of in the member because of, at least in part, unexpectedly high strengths of the member materials. This is a consequence of the constraints dictated by the specimens' configurations, which were chosen purposely to have relatively short welds, for which the maximum weld size was limited to $\frac{7}{16}$ in. and for which selecting an electrode stronger than E70 would have led to the strength of the adjacent base metal to govern, even when expected material strengths were considered. Thus, the weld strength and base metal strength were in many instances very close to each other, such that even a moderate overstrength of the base metal would force a limit state in the weld. As shown in Table 3, the measured F_u is on average 77 ksi for the plates and 75 ksi for the angles.

The maximum load for each specimen was recorded, and the experimental shear lag factors, U_e, were calculated as

the ratio of the maximum load to the rupture strength (gross area × ultimate tensile stress, F_u). The ultimate tensile stress was taken as the value determined from the material coupon testing. The experimental shear lag factor for each specimen is shown in Table 4. For the specimens that did not experience net section fracture, the experimental shear lag factor can be taken to be at least equal to those shown in Table 4.

Plate Specimens

All of the experimental shear lag factors for the plate specimens, except Specimens A-4 and A-7, were greater than 0.90. This agrees with what previous researchers have found (Easterling and Giroux-Gonzalez, 1993). Specimens A-4 and A-7 both experienced weld failures; therefore, the experimental shear lag factor would have been greater than the recorded value if the welded connection had sufficient strength. To validate the consistency of the experiment, two identical specimens were tested. The results from Specimens A-2a and A-2b show the testing was very consistent

because both specimens failed by gross section fracture with virtually no difference in the maximum load. To investigate the degree to which the connection length affects the experimental shear lag factor, the results from Specimens A-1 and A-3 can be compared. Specimen A-1 had two 8-in. welds with $U_e = 0.96$, while Specimen A-3 had two 4-in. welds with $U_e = 0.92$. From these results, the connection length for plates with a balanced weld configuration appears to have a minimal effect on the experimental shear lag factor, which was previously noted in a thesis by Dhungana (2014). A comparison of Specimens A-1 and A-5 reveals the effect of the weld configuration. Specimen A-1 had a balanced weld configuration with two 8-in. longitudinal welds, and Specimen A-5 had an unbalanced weld configuration with $L_A = 4$ in. and $L_C = 8$ in. Both of these specimens experienced gross section fracture and had an experimental shear lag factor of 0.96. An unbalanced weld configuration leading to in-plane eccentricity appears to have had no effect on the efficiency of longitudinally welded plates. Further review of all plate-type tension members that failed by either gross or net section failure (A-1, A-2a, A-2b, A-3, A-5, and A-6) also supports the premise that in-plane eccentricity appeared to have little effect on the experimental shear lag factor, U_e. The four plate specimens with balanced weld configurations (A-1, A-2a, A-2b, and A-3) had shear lag factors that ranged between 0.92 and 0.96, while the two plate specimens with unbalanced weld configurations (A-5 and A-6) had shear lag factors of 0.96 and 0.95, respectively.

Angle Specimens

The experimental shear lag factors, U_e, for two angle specimens (C-1 and C-5) that failed by net section fracture were 0.95 and 0.91, respectively. For the angles experiencing weld failures, the experimental shear lag factors ranged from 0.36 to 0.88. Larger values for these experimental shear lag factors would have been achieved if the welded connection had sufficient strength to reach the net section capacity of these members. To confirm consistency in testing of the angles, two identical specimens were tested. The results from Specimens C-7a and C-7b show the testing was again very consistent from specimen to specimen. Both members failed through the weld with a slight difference in the maximum load. Specimens C-1 (unbalanced weld configuration) and C-5 (balanced weld configuration) did experience net section failure while the remaining angle specimens experienced weld failure. Although only two specimens experienced net section failure, the experimental shear lag factor, U_e, of both Specimens C-1 and C-5 exceeded the theoretical shear lag factor, U_t, of the 2016 *Specification*.

The angles that experienced net section fracture (C-1 and C-5) were compared with plate specimens (A-1 and A-5) that had similar weld configurations at each end. The plates experienced gross section fracture and failed as designed at the bottom, with Specimen A-1 having a balanced connection and Specimen A-5 having an unbalanced connection. Both angles, however, failed at the top connection under a combination of in-plane and out-of-plane eccentricity. The experimental shear lag factor, U_e, was 0.95 for angle Specimen C-1 and 0.91 for angle Specimen C-5 as compared to 0.96 for the plates.

DISCUSSION

Theoretical Shear Lag Factors

Theoretical shear lag factors, U_t, were calculated using the 2010 AISC *Specification* (AISC, 2010), the bi-planar model from Fortney and Thornton (2012), and the 2016 AISC *Specification* (AISC, 2016b). The theoretical shear lag factors for the AISC bi-planar model and those using the 2010 AISC *Specification* were calculated based on the requirements developed by Fortney and Thornton and the 2010 AISC *Specification*, respectively. The theoretical shear lag factors based on the 2016 AISC *Specification* were calculated using Table D3.1, Case 4, for the angle and plate specimens. These values are shown in Table 5 along with the ratio of experimental to theoretical shear lag factors, U_e/U_t.

Using the 2010 AISC *Specification*, the values of U_e/U_t for the plate specimens ranged from 0.92 to 1.23, with two values greater than or equal to 1.00. For the angle specimens, U_e/U_t ranged from 0.67 to 1.08, with eight values being lower than 1.00. All of the U_e/U_t values less than 1.00 for the angle specimens experienced weld failure.

Using the bi-planar model (Fortney and Thornton, 2012), the values of U_e/U_t for the plate specimens ranged from 0.92 to 1.24 with three of the eight members having values equal to or greater than 1.00. These values were the same as those for the aforementioned 2010 AISC *Specification* values with the exception of the value of U_e/U_t for Specimen A-4, which was not calculated because the 2010 AISC *Specification* did not allow l/w to be less than 1.0. For the 12 angle specimens, U_e/U_t ranged from 0.90 to 1.33, with only two values less than 1.00. These two values were from specimens that experienced weld failure.

Using the 2016 AISC *Specification*, the values of U_e/U_t for the plate specimens ranged from 0.99 to 1.16, with seven of the eight members having values equal to or greater than 1.0. The one plate member (A-6) failing at the net section had a theoretical shear lag virtually equal to the experimental value. For the angle specimens, the values ranged from 0.87 to 1.19, with only two values being less than 1.00. The two values that were less than 1.00 were for members (C-3 and C-9) that failed through the weld, indicating that the experimental shear lag value for these members would have been higher had they been able to reach net section capacity before the welds failed.

	Table 5. Experimental and Theoretical Shear Lag Factors								
Specimen	**Experimental Shear Lag Factor, U_e**		$\dfrac{l}{w}$	**Theoretical Shear Lag Coefficient, U_t**			$\dfrac{U_e}{U_t}$		
				2010	**Bi-Planar**	**2016**	**2010**	**Bi-Planar**	**2016**
A-1	0.96		2.67	1.00	1.00	0.96	0.96	0.96	1.00
A-2a	0.92		2.00	1.00	1.00	0.92	0.92	0.92	1.00
A-2b	0.92		2.00	1.00	1.00	0.92	0.92	0.92	1.00
A-3	0.92		1.33	0.75	0.75	0.84	1.23	1.23	1.10
A-4	> 0.62		0.67	*	0.50	0.57	*	>1.24	>1.09
A-5	0.96		2.00	1.00	1.00	0.92	0.96	0.96	1.04
A-6	Top connection	0.95	2.67	1.00	1.00	0.96	0.95	0.95	0.99
	Bottom connection	>0.95	1.50	0.87	0.87	0.87	>1.09	>1.09	>1.09
A-7	>0.87		1.00	0.75	0.75	0.75	>1.16	>1.16	>1.16
C-1	Top connection	0.95	3.33	0.91	0.91	0.88	1.04	1.04	1.08
	Bottom connection	>0.95	2.67	0.88	0.88	0.84	>1.08	>1.08	>1.13
C-2	> 0.88		2.00	0.85	0.85	0.78	>1.04	>1.04	>1.13
C-3	> 0.56		1.33	0.77	0.58	0.65	>0.73	>0.97	>0.87
C-4	> 0.36		0.67	0.54	0.27	0.31	>0.67	>1.33	>1.18
C-5	Top connection	0.91	3.33	0.91	0.91	0.88	1.00	1.00	1.03
	Bottom connection	>0.91	2.00	0.85	0.85	0.78	>1.08	>1.07	>1.17
C-6	> 0.76		1.50	0.79	0.69	0.69	>0.96	>1.10	>1.10
C-7a	> 0.42		0.75	0.59	0.33	0.37	>0.72	>1.27	>1.14
C-7b	> 0.44		0.75	0.59	0.33	0.37	>0.75	>1.33	>1.19
C-8	> 0.41		0.75	0.59	0.33	0.37	>0.70	>1.24	>1.11
C-9	> 0.62		1.50	0.79	0.69	0.69	>0.78	>0.90	>0.90
C-10	> 0.87		2.00	0.85	0.85	0.78	>1.03	>1.02	>1.12
C-11	> 0.76		1.50	0.79	0.69	0.69	>0.96	>1.10	>1.10
* 2010 AISC *Specification* did not allow $l/w < 1$.									

A comparative analysis of the U_e/U_t ratios based on the three methods was performed. In order for the theoretical shear lag factor to be conservative, the ratio U_e/U_t needs to be greater than or equal to 1.00. Figure 12 shows a comparison of the U_e/U_t ratio for the 20 specimens tested using the three aforementioned methods of determining theoretical shear lag factors. The 2016 AISC *Specification* based on the fixed-fixed beam model performed best, with 85% of the members tested (17 of the 20) having a U_e/U_t ratio exceeding 1.00. In addition to the high percentage of tests having a U_e/U_t ratio exceeding 1.00, the 2016 AISC *Specification* for shear lag also shows much less variability than either of the other two methods used in this comparison. The bi-planar model had 65% of the members tested (13 of the 20) with a U_e/U_t ratio exceeding 1.00, while the 2010

AISC *Specification* was the least conservative because only 32% of the members tested (6 of the 19) had a U_e/U_t ratio exceeding 1.00. In addition, the comparison showed that U_e/U_t values for both the bi-planar model and the 2010 AISC *Specification* were more variable than those using the 2016 AISC *Specification*.

Another comparison was performed based on the average length of the welds versus the distance between the welds, l/w. Graphs of shear lag factor versus l/w are presented in Figures 13, 14, and 15. After comparing the experimental shear lag factors of the 20 welded specimens to the theoretical values from the three methods, it can be seen that the experimental shear lag factors for members experiencing non-weld failure conform closely to provisions given in 2016 *Specification* Table D3.1, Case 4. For the five plates that experienced either gross or net section failure the U_e/U_t
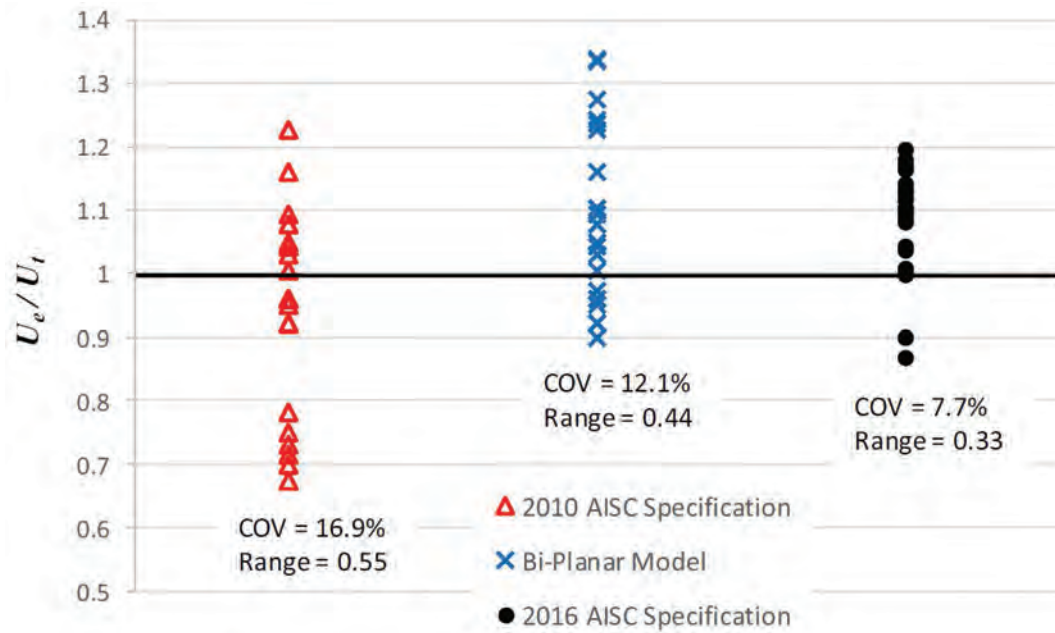
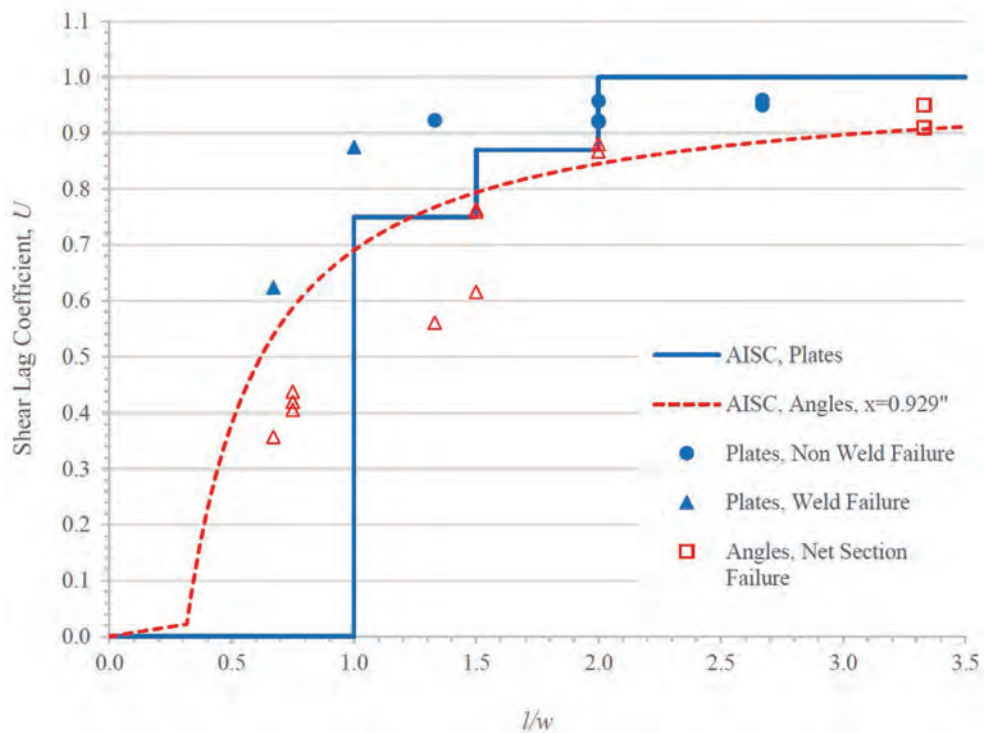Fig. 12. U_e/U_t Comparison between different shear lag models.

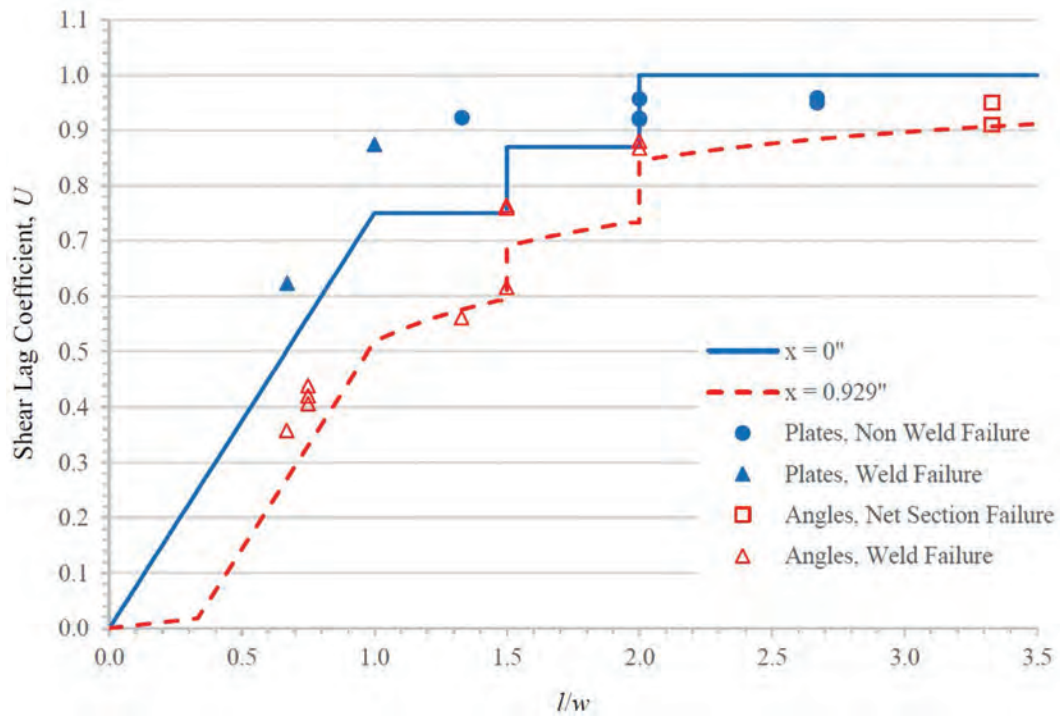Fig. 13. Shear lag factor versus l/w using the 2010 AISC Specification.

Fig. 14. Shear lag factor versus l/w *using Fortney and Thornton's (2012) bi-planar recommendation.*
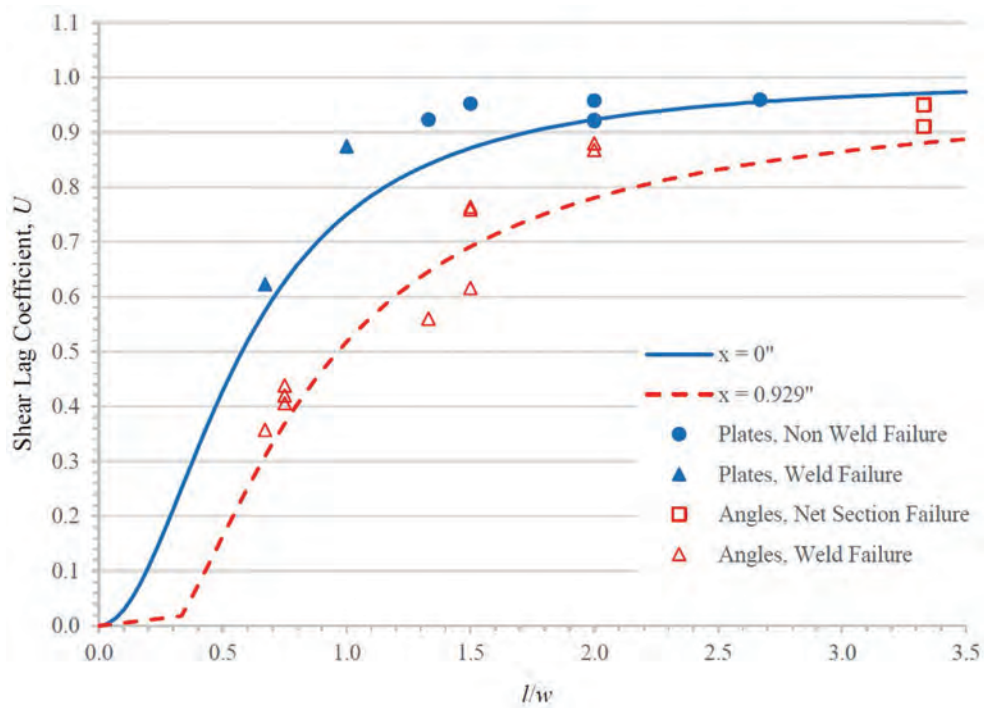

Fig. 15. Shear lag factor versus l/w *using the 2016 AISC* Specification.

ratio ranged from 0.99 to 1.10, with l/w ratios that varied between 1.33 and 2.67. Although only two angles experienced net section failure, those two members had a U_e/U_t ratio ranging from 1.03 to 1.08, and each angle had an l/w ratio of 3.33. This indicates that Case 4 from the 2016 AISC *Specification* seems to adequately predict shear lag factor over a wide range of l/w ratios.

Another item of note is the behavior of the experimental specimens with a length-to-width ratio under 1.0 (i.e., $l/w < 1.0$). The 2016 AISC *Specification* removed the previous limitation that the length of the longitudinal welds must be greater than or equal to the distance between them. The experimental results discussed herein contained four angles and one plate with l/w ratios of less than 1.0. Although, perhaps not surprisingly, all five of these tension members experienced weld failures, the U_e/U_t ratio for these specimens ranged from 1.09 to 1.19 when compared to the 2016 *Specification*. When the U_e/U_t ratio for these five members was calculated using the bi-planar model (Fortney and Thornton, 2012) the range is 1.24 to 1.33. This suggests that the experimental specimens with $l/w < 1.0$ appear to conform most closely with the 2016 AISC *Specification*.

SUMMARY AND CONCLUSIONS

The main objective of this paper was to experimentally test 20 longitudinally welded tension specimens and compare the experimental shear lag factor to theoretical values from three methods. Eight 3×½ plate sections and twelve 3×3×½ angle sections were tested. The parameters that were varied include the length of the connection and the weld configuration. Also, four coupons—two from the plate material and two from the angle material—were tested in tension to determine the yield stress and the ultimate stress of the plate and angle material.

The experimental shear lag factor, U_e, for each specimen was calculated as the ratio of the maximum load measured to the rupture strength. Experimental shear lag factors were determined for each of the 20 tested specimens and compared to three theoretical values: (1) the shear lag factor from Case 4 in the 2016 AISC *Specification*, (2) the shear lag factor based on a bi-planar model (Fortney and Thornton, 2012), and (3) the shear lag factor from the 2010 AISC *Specification*. The ratio of the experimental shear lag factor to the theoretical, U_e/U_t, was used to identify which of the three methods provided the best prediction of shear lag behavior. Trends of the experimental shear lag factor were also studied with respect to the influence of connection length versus width, l/w.

Based on the results from the experimental program and a comparison of shear lag factors to the aforementioned provisions, it has been found that:

2016 AISC *Specification* Table D3.1, Case 4, provides the best prediction of shear lag factor in longitudinally welded tension members under the influence of eccentricity. The 20 tension members tested in this experiment, with a mixture of balanced and unbalanced longitudinal welds, showed that shear lag factors using the 2016 AISC *Specification* had the highest percentage of U_e/U_t ratios at or above 1.0 with the least variation as compared to the 2010 AISC *Specification* as well as to the bi-planar model studied by Fortney and Thornton.

2016 AISC *Specification* Table D3.1, Case 4, provides the best prediction of shear lag factor in longitudinally welded tension members with connection length-to-width ratios of less than 1.0 ($l/w < 1.0$). The experimental tension members with $l/w < 1.0$ conformed more closely to the 2016 AISC *Specification* than to the bi-planar model. For members with $l/w < 1.0$ using the AISC bi-planar model, the U_e/U_t ratio ranged from 1.24 to 1.33 while the same value ranged from 1.09 to 1.19 using the 2016 AISC *Specification*.

For the flat plate specimens, all of the experimental shear lag factors were greater than 0.90, except for the two specimens that failed via weld fracture. The connection length for plates with a balanced weld configuration appears to have had a small effect on the experimental shear lag factor. The testing of a specimen having two 8-in. welds resulted in an experimental shear lag factor of 0.96, while a similar tension member having two 4-in. welds resulted in an experimental shear lag factor of 0.92. This difference is less than that predicted by the 2016 AISC *Specification*.

For the flat plate specimens, the presence of in-plane eccentricity appeared to have had little effect on the experimental shear lag factor, U_e. Among plates that experienced gross or net section failure, the four plate specimens with balanced weld configurations had shear lag factors that ranged between 0.92 and 0.96, while the two plate specimens with unbalanced weld configurations had shear lag factors of 0.96 and 0.95, respectively. A comparison of the experimental shear lag factor for these six specimens conformed very closely with the theoretical shear lag factor based on the 2016 AISC *Specification*.

ACKNOWLEDGMENTS

REFERENCES

AISC (1986), *Load and Resistance Factor Design Specification for Structural Steel Buildings*, American Institute of Steel Construction, Chicago, Ill.

AISC (1989), *Specification for Structural Steel Buildings—Allowable Stress Design and Plastic Design*, American Institute of Steel Construction, Chicago, Ill.

AISC (2005), *Specification for Structural Steel Buildings*, ANSI/AISC 360-05, American Institute of Steel Construction, Chicago, Ill.

AISC (2010), *Specification for Structural Steel Buildings*, ANSI/AISC 360-10, American Institute of Steel Construction, Chicago, Ill.

AISC (2016a), *Seismic Provisions for Structural Steel Buildings*, ANSI/AISC 341-16, American Institute of Steel Construction, Chicago, Ill.

AISC (2016b), *Specification for Structural Steel Buildings*, ANSI/AISC 360-16, American Institute of Steel Construction, Chicago, Ill.

Dhungana, U. (2014), *Shear Lag Factor for Longitudinally Welded Tension Members Using Finite Element Method*, Thesis, University of Cincinnati, Cincinnati, Ohio.

Easterling, W.S. and Giroux-Gonzalez, L. (1993), "Shear Lag Effects in Steel Tension Members," *Engineering Journal,* AISC, Vol. 30, No. 3, pp. 77–88.

Fortney, P.J. and Thornton, W.A. (2012), "Recommendations for Shear Lag Factors for Longitudinally Welded Tension Members," *Engineering Journal,* AISC, Vol. 49, No. 1, pp. 11–32.

Mannem, R. (2002), *Shear Lag Effects on Welded Steel Angles and Plates*, Thesis, Department of Civil Engineering, University of Newfoundland.

Salmon, C.G., Johnson, J.E., and Malhas, F.A. (2009), *Steel Structures: Design and Behavior*, Pearson Education Inc., Upper Saddle River, N.J.

Evaluation of AISC Seismic Design Methods for Steel Multi-Tiered Special Concentrically Braced Frames

PABLO A. CANO and ALI IMANPOUR

ABSTRACT

Steel multi-tiered concentrically braced frames (MT-CBFs) are commonly used in North America as a lateral load resisting system of tall single-story buildings. Past studies show that MT-CBF columns designed in accordance with the 2010 AISC *Seismic Provisions* are prone to buckling due to a high axial compression force combined with in-plane bending moments caused by the nonuniform distribution of inelastic brace deformations along the frame height. Special design provisions have been introduced in the 2016 AISC *Seismic Provisions* to address flexural demands imposed on MT-CBF columns and prevent column instability. In this paper, the seismic design methods for multi-tiered special concentrically braced frames are evaluated using the nonlinear finite element analysis method. A two-tiered special concentrically braced frame was then created, and nonlinear static and dynamic analyses were performed to evaluate the seismic performance of both frames. Analysis results confirmed that the inelastic deformations in the frame designed using the 2010 requirements are not uniformly distributed but rather concentrated in one of the tiers and cause column instability under large story drifts, whereas, the 2016 design method significantly improves the distribution of inelastic deformation along the height of the frame and prevents column instability. Furthermore, it was found that the 2016 AISC *Seismic Provisions* accurately estimate the axial load but overestimate the in-plane flexural demands and underestimates the out-of-plane flexural demand. Nonetheless, the overestimation of in-plane flexure demands results in acceptable strength capacity even though out-of-plane flexural demands is underestimated.

Keywords: Steel multi-tiered concentrically braced frame, design standards, column buckling, cyclic-pushover analysis.

INTRODUCTION

Steel multi-tiered concentrically braced frames (MT-CBFs) are widely used in North America as a lateral-resisting system of tall, single-story buildings such as airplane hangars, recreational facilities, shopping centers and industrial buildings. MT-CBFs consist of multiple bracing panels stacked along the height of the building and are separated by horizontal struts as illustrated in Figure 1(a). Intermediate struts are used between braced panels to avoid unsatisfactory K-braced frame (K-BF) response. Various bracing configurations—including chevron, diagonal, V-type, and cross—are used in MT-CBFs. Two examples of such frames with cross bracing configuration is shown in Figures 1(b) and 1(c). Multi-tiered arrangements are typically used when it is not practical or economical to use a single bracing panel along the height of the frame. In MT-CBFs, the length of the braces is reduced, resulting in a lower slenderness ratio, which allows for smaller brace sizes to resist lateral loads and a more efficient angle between the

brace and the horizontal plane of the frame. Additionally, the buckling length of the column in the plane of the frame is reduced as the intermediate struts provide lateral support for in-plane buckling. This framing configuration is also beneficial when frames are designed to resist seismic load effects. The limits on width-to-thickness and global slenderness ratios can be easily satisfied when using shorter braces. Moreover, reduced brace sizes result in smaller design forces on the adjacent members, including struts, beams, columns, connections, and footing.

MT-CBF columns are typically W-shaped members oriented such that out-of-plane bending moment due to the wind load acts about the major axis of the section. The columns can be considered braced in the plane of the frame as a result of horizontal struts; however, no out-of-plane bracing exists between the ground and roof levels, and the column buckling length is equal to the full-frame height in this direction.

Two concentrically braced frame systems have been defined in the AISC *Seismic Provisions* (AISC, 2010, 2016a): ordinary concentrically braced frames (OCBFs) and special concentrically braced frames (SCBFs). Braces of both OCBFs and SCBFs are sized to resist the seismic load effects under the design seismic base shear. In SCBFs, the columns are designed under the axial loads due to the combined gravity loads and the axial capacity of the braces when they respond in the inelastic range. The columns of OCBFs are, however, designed to resist the overstrength seismic load. The 2010 AISC *Seismic Provisions* (AISC, 2010) did not include design provisions for MT-CBFs. The
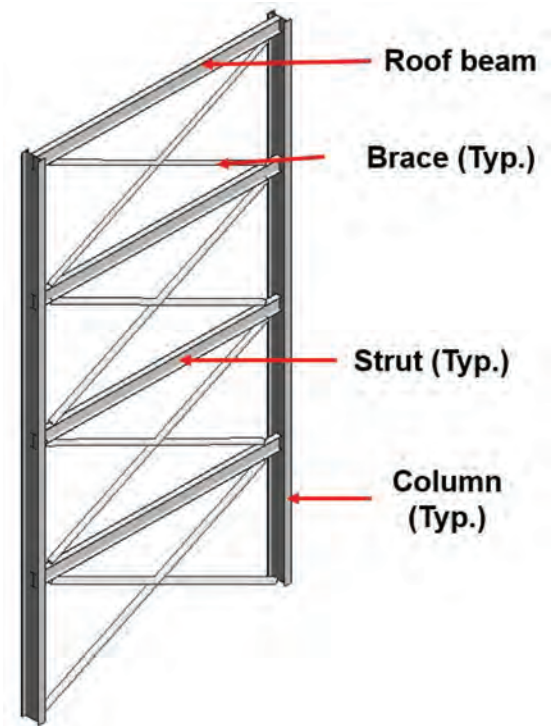
Pablo A. Cano, E.I.T, M.Sc., Ph.D. Student, University of Alberta, Edmonton, Alberta. Email: cano@ualberta.ca (corresponding)

Ali Imanpour, P.Eng., Ph.D., Assistant Professor, University of Alberta, Edmonton, Alberta. Email: imanpour@ualberta.ca

(a) Multi-tiered concentrically braced frame components

(b) Two-tiered concentrically braced frame

(c) Four-tiered concentrically braced frame

Fig. 1. Multi-tiered concentrically braced frames.

two brace loading analysis cases for SCBFs in this standard led engineers to recognize the potential for unbalanced loads at the intermediate tier due to the violation of the equilibrium when such brace loading scenarios are considered. As such, this framing configuration over time came to be considered a K-brace, a framing system that is prohibited by the AISC *Seismic Provisions*. In the absence of special design provisions, MT-CBFs had been designed using the provisions prescribed for multi-story steel braced frames in Section F of the 2010 AISC *Seismic Provisions*.

The seismic behavior of MT-CBFs designed using the 2010 *Seismic Provisions* has been the focus of a number of research studies in recent years (Imanpour and Tremblay, 2012, 2014; Imanpour et al., 2013, 2016a). The results obtained from past numerical simulations confimed that inelastic frame deformations tend to concentrate in a single tier rather than be uniformly distributed along the height of

the frame. The reason is that tensile yielding is only initiated in the tier that has the lowest story shear resistance; this tier is referred to as the critical tier. Even if tiers are identical, slight variations between the brace properties such as material properties, initial geometric imperfections, or end conditions can lead to the initiation of brace yielding in one of the tiers. This response is illustrated in Figure 2(a) for the two-tiered CBF. As shown in Figure 2(b), the compression braces buckle nearly simultaneously in both tiers. As the lateral displacement at the roof level increases, tensile yielding initiates only in one of the tiers [i.e., Tier 1 as shown in Figure 2(c)], which reduces the story shear resistance of that tier and attracts the rest of the lateral deformations, thus preventing tensile yielding of the tension brace in the adjacent tiers. By further elongation of the tensile brace after yielding, excessive inelastic deformations are induced in the critical tier. The difference between the story
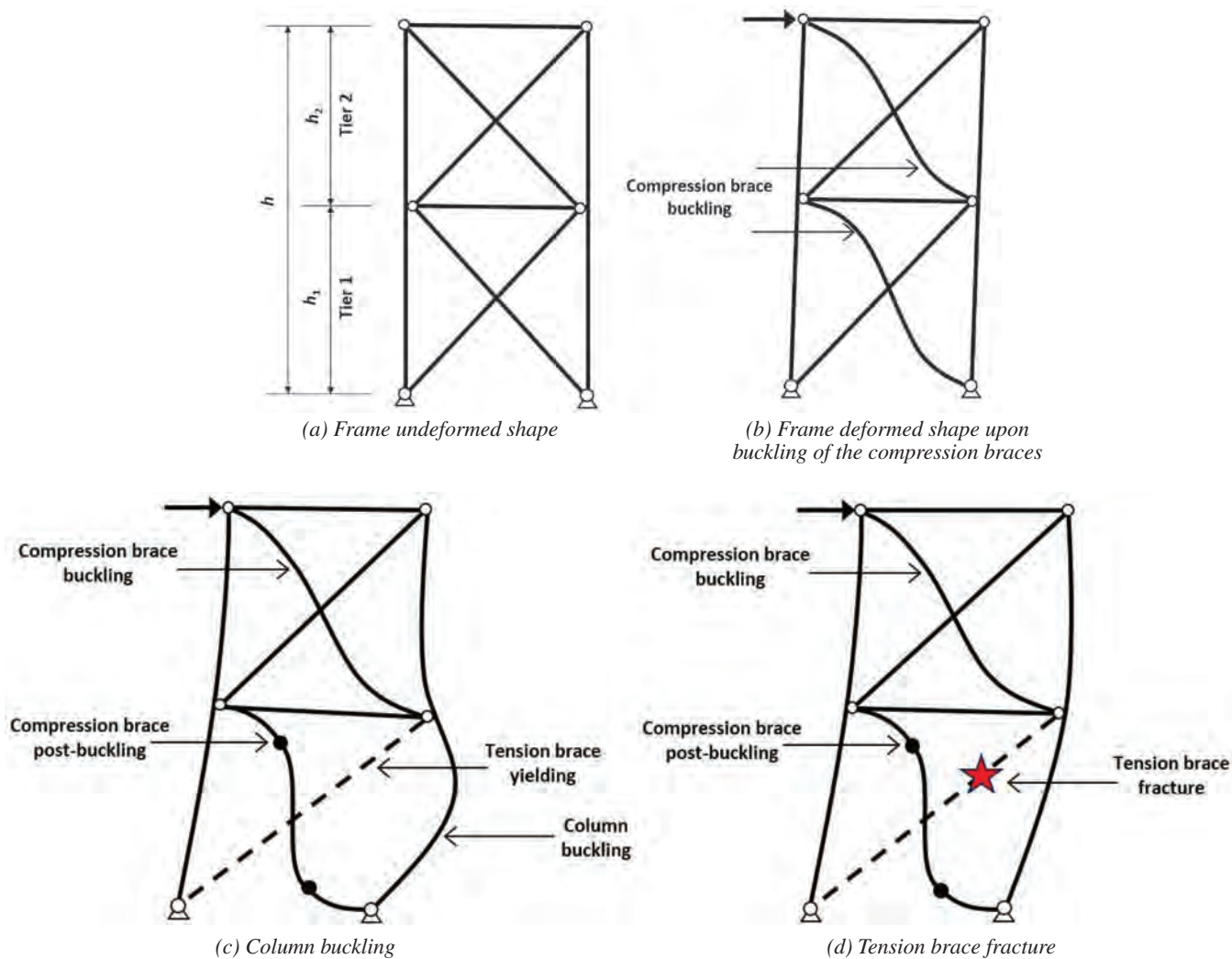

(a) Frame undeformed shape

(b) Frame deformed shape upon buckling of the compression braces

(c) Column buckling

(d) Tension brace fracture

Fig. 2. Inelastic response of MT-CBFs.

shear resistance of the adjacent tiers induces an unbalanced horizontal shear force on the columns of the frame, which results in large in-plane bending moments in the columns. The concentration of inelastic deformations in the critical tier can lead to column yielding under the combination of high axial compression force and bending moments if the columns do not possess sufficient strength and stiffness. Such large demands may lead to column buckling as shown in Figure 2(c) and even frame collapse. It was found that column instability is first initiated in the plane of the frame in a flexural buckling mode and suddenly changes to a flexural-torsional buckling mode as excessive out-of-plane displacements develop at the frame mid-height. In addition to column instability, excessive brace deformations that take place only in one of the tiers can lead to low cyclic fatigue fracture of the brace (Tremblay et al., 2003; Hsiao et al., 2013) as shown in Figure 2(d).

Stoakes and Fahnestock (2014, 2016) showed that providing torsional bracing, along the height of the column at the strut-to-column connections, can improve the strong-axis buckling strength in the presence of in-plane flexural yielding, particularly when the location of the weak-axis flexural moment matches the location of the strong-axis flexural moment. More recently, Imanpour et al. (2018) examined the seismic performance of an MT-CBF designed in accordance with the 2010 AISC *Seismic Provisions* using hybrid simulation where the first-tier column segment was tested experimentally, while the rest of the frame was analyzed numerically. The results of hybrid simulations confirmed the column instability observed in previous numerical simulations. A preliminary study was recently performed by the authors to evaluate the seismic response of multi-tiered concentrically braced frames designed in accordance with the 2010 and 2016 *Seismic Provisions* (AISC, 2010, 2016a; Cano and Imanpour, 2018, 2019). The results provide insight into the behavior of MT-CBFs designed in accordance with the 2016 *Seismic Provisions* and also the unfavorable failure modes of frames designed in accordance with the 2010 *Seismic Provisions* frames such as column buckling and frame collapse.

The 2016 AISC *Seismic Provisions* have introduced special design requirements for both multi-tiered OCBFs and SCBFs to address the unsatisfactory response of MT-CBFs observed in previous studies. Although significant improvements have been made over the past decade in the seismic design methodologies of multi-tiered braced frames, it is felt that there is limited information to validate and improve the recently adopted design requirements. In particular, the in-plane and out-of-plane bending moment demands prescribed by the current AISC *Seismic Provisions* must be examined and improved if necessary.

This paper aims to examine and compare the seismic design methods for steel multi-tiered special concentrically braced frames (MT-SCBFs) designed in accordance with the 2010 and 2016 AISC *Seismic Provisions*. In particular the paper serves to confirm the improved seismic performance expected when the 2016 provisions are employed. A review of the current and previous seismic design provisions is first given. The seismic design of a case study two-tiered SCBF in accordance with both provisions is then presented followed by the analysis of the seismic response of the frames using nonlinear static (pushover) and nonlinear dynamic (response history) analyses. Finally, the analysis results including the drifts and column moment demands are discussed and used to evaluate the column design demands.

AISC *SEISMIC PROVISIONS* FOR THE DESIGN OF STEEL MT-SCBFS

2010 AISC *Seismic Provisions*

In the 2010 AISC *Seismic Provisions*, no special design guidelines existed for the design of MT-SCBFs. In lieu of such provisions, the requirements for standard SCBFs were used in design. Two analysis cases (A and B) were considered in Section F2.3 representing the brace nonlinear response to determine the forces in the members adjacent to the bracing members, such as columns, struts, beams, and their connections. Analysis cases A and B are shown in Figures 3(a) and 3(b) for a two-tiered braced frame, respectively. In analysis case A, the tension braces reach their expected tensile strength, T_{exp}, and compression braces reach their expected buckling strength, C_{exp}. Moreover, the second analysis case represents the frame response after experiencing several inelastic cycles where the tension braces elongated in tension, but their strength can still be estimated by the expected tensile strength, T_{exp}, while the compression braces reach their expected post-buckling strength, C'_{exp}. These two analysis cases result in seismic axial forces in the columns and struts of MT-SCBFs, which are used to size these members. The effect of gravity loads must be also considered for the design of columns and the roof beam.

2016 AISC *Seismic Provisions*

Past numerical simulations showed that the seismic-induced demands in multi-tiered braced frames differ from those in standard multi-story concentrically braced frames, which, if not considered in the design, may result in column instability or excessive brace elongation that can lead to brace fracture (Imanpour and Tremblay, 2014; Imanpour et al., 2016a). The 2016 AISC *Seismic Provisions* have introduced design requirements for ordinary and special concentrically braced frames as well as buckling-restraint braced frames to prevent such unsatisfactory limit states in the braced frames with multi-tiered configurations. According to the 2016 AISC *Seismic Provisions* Section F2.3(c), MT-SCBFs

must be analyzed under the new analysis case (C) in addition to analysis cases A and B applied to all other SCBFs. This new analysis case is shown in Figure 3(c) for a two-tiered braced frame. Analysis case C represents the progressive yielding and buckling of braces in MT-SCBFs, meaning that brace tensile yielding has occurred in the tier that possesses the least story shear resistance (critical tier) [i.e., Tier 1 in Figure 3(c)] and propagates to the strongest tier [Tier 2 in Figure 3(c)]. In analysis case C, it is assumed that the compression brace in the critical tier has reached its post-buckling strength, C'_{exp}, and the compression brace in the noncritical tier has reached its expected buckling strength, C_{exp}. Concurrently, the tension brace in both tiers is assumed to be at their expected tension strength, T_{exp}.

In the case of frames with more than three tiers, the compression forces can be taken equal to their expected buckling strength while the tension forces are below their expected tension strength, which can be computed using an equilibrium knowing that tiers have an identical story shear. For a two-tiered braced frame similar to the one shown in Figure 2(a), analysis case C requires only one step when the critical tier is known; however, analysis case C must be repeated with the critical tier being Tier 2 if the difference between the story shear resistances is negligible to account for potential variabilities in the brace material (Schmidt and Barlett, 2002), brace length connection details, or initial geometric imperfections. The designer can set the criterion to identify the critical tier based on the story shear resistance (e.g., a difference between the story shear resistances less than 10% would be deemed sufficient to examine other plausible critical cases). This would mean that multiple analyses are

needed when designing frames with three or more bracing tiers under analysis case C. As a result of this analysis case, columns are subjected not only to an axial force, but also to an in-plane bending moment due to the difference between the shear forces in the braces of adjacent tiers, which creates an unbalanced brace story shear force on the columns. To obtain the column bending moments in a two-tiered braced frame, half of the unbalanced brace story shear force, which is determined under the brace expected forces, is used on a simply supported column spanning between the tiers. This method can be expanded to frames with three or more tiers when brace tension yielding propagates progressively starting from the bottom tier or from the top one (Imanpour and Tremblay, 2016; Imanpour et al., 2016b).

In addition to the new analysis case that results in column in-plane moment demands, an out-of-plane bending moment demand must be considered in design of columns as outlined in AISC *Seismic Provisions* Section F2.4e(c)(3). Out-of-plane bending moments are induced in the columns of multi-tiered braced frames as a result of initial geometric imperfections, out-of-plane buckling of braces, and plastic hinge forming in the brace gusset plate. The 2016 AISC *Seismic Provisions* require a horizontal notional load be applied on the column at the tier level to produce an out-of-plane bending moment demand on the column, representing imperfection effects. The notional load is equal to 0.006 times the vertical component of the compression brace that meets the column at the tier level. This notional load should be amplified by the B_1 factor (AISC, 2016b) to account for P-δ effects. Furthermore, the columns must be designed to resist the out-of-plane moment produced by the buckling

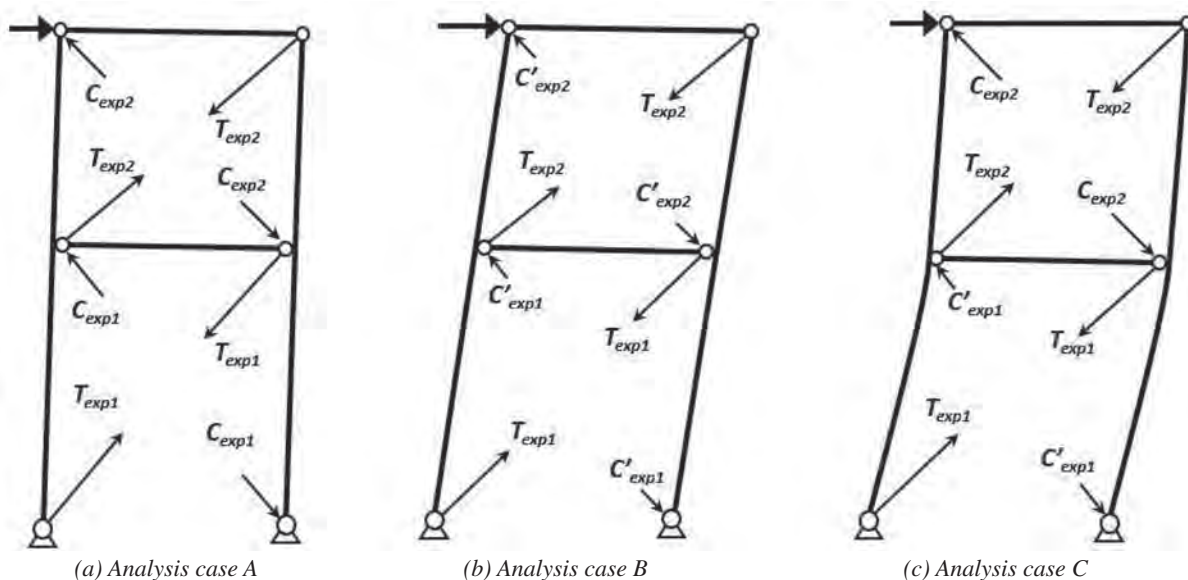(a) Analysis case A   (b) Analysis case B   (c) Analysis case C

Fig. 3. Brace loading scenarios used for the design of capacity-controlled members.

of the braces, but less than the maximum bending moment resistance of the brace connections.

As required in the 2016 AISC *Seismic Provisions* Section F2.4e(b)(1), MT-CBFs must also have intermediate struts placed between adjacent tiers to prevent the unsatisfactory K-braced frame response. Furthermore, columns must be torsionally braced at the strut-to-column connections as per Section F2.4e(c)(1). Finally, AISC *Seismic Provisions* Section F2.4e(d) has established a maximum tier drift ratio of 2% to prevent excessive brace deformations that can cause brace low-cycle fatigue fracture.

BUILDING CONFIGURATION AND LOADING FOR CASE STUDY

Building Geometry

A single-story steel building located in Seattle, Washington, was selected as a case study. The building has plan dimensions of 115 ft × 620 ft with a height of $h = 29.5$ ft. In each principal direction, the building has four concentrically braced frames (two per each exterior wall). The frame height is divided into two tiers with X-bracing configuration as shown in Figure 4. As illustrated, the bottom tier (Tier 1) height is $h_1 = 15.4$ ft, and the top tier (Tier 2) height is $h_2 = 14.1$ ft. The purpose of having tiers of different heights is to trigger brace tensile yielding in one of the tiers first. A special concentrically braced frame system was selected.

The columns are made of wide-flange sections and oriented such that the out-of-plane bending moment occurs about the strong-axis of the section. A 23-ft horizontal strut is placed between tiers to prevent K-braced frame response and ensure the seismic load is appropriately transferred to the base through the truss action once the braces respond in the inelastic range.

Loading

The design loads for the selected building were determined in accordance with ASCE/SEI 7-16 *Minimum Design Loads and Associated Criteria for Buildings and Other Structures* (ASCE, 2016). Risk Category II was chosen, and it was assumed that the building is located on a Site Class C with a Seismic Design Category D. The gravity loads include the roof dead load DL = 21 psf, the exterior wall dead load WL = 10 psf, and a live load LL = 20 psf. The tributary area considered per column was calculated on the basis that steel roof trusses support the roof system between the exterior walls of the building. The resulting factored axial load at the top of each column was then calculated to be $P_G = 56$ kips.

The seismic load parameters include a response modification factor $R = 6.0$, overstrength factor $\Omega_o = 2$, and a deflection amplification factor $C_d = 5.0$. The mapped risk-targeted Maximum Considered Earthquake (MCE_R)

spectral response acceleration parameters, $S_S = 1.362g$ and $S_1 = 0.458g$ for short and 1.0-s periods, respectively, were used to obtain the design spectral response acceleration parameters $S_{DS} = 0.908g$ and $S_{D1} = 0.458g$. The empirical fundamental period was calculated using $C_t = 0.0488$ and $x = 0.75$, which is equal to $T_a = 0.25$ s. The seismic design coefficient was then calculated as $C_s = 0.15$. The seismic weight of the building W is equal to 1,710 kips and was obtained from the roof dead load plus half of the exterior wall dead load. The equivalent lateral force procedure was used to calculate the frame seismic base shear V, which is the product of the seismic coefficient and the seismic weight. This force was amplified to account for accidental torsion, resulting in a seismic design base shear per frame equal to 71 kips.

FRAME DESIGN

Design of structural members was performed in accordance with the AISC *Specification for Structural Steel Buildings* (AISC, 2016b) and AISC *Seismic Provisions* (AISC, 2010; 2016a). This section summarizes the key design steps and member sizes for braces, columns, and the strut. The design of braces is presented once as the steps and requirements are the same for both the 2010 and 2016 designs. The column design is described for each braced frame individually. Design of the strut is presented once and differences between the 2010 and 2016 designs are highlighted. The frame drift check is then presented for each design.

Brace Design

The braces in both tiers were designed to resist the seismic load effects in tension and compression. The brace design compression force in Tier 1 is equal to $P_{r,b1} = 45$ kips, which includes the seismic induced axial force $P_{E,b1} = 43$ kips plus the gravity-induced axial force $P_{G,b1} = 2$ kips. The design compression force of the Tier 2 brace is $P_{r,b2} = 44$ kips, which similarly includes the seismic induced axial force $P_{E,b2} = 42$ kips plus the gravity-induced axial force $P_{G,b2} = 2$ kips. The braces are designed using square HSS members. Such members are commonly used in practice and are more efficient than singly symmetric sections as they have an identical radius of gyration about both principal axes of the section (Black et al., 1980). The braces are made of ASTM A1085 steel (ASTM, 2015a) with a yield stress $F_y = 50$ ksi and an expected yield stress $R_yF_y = 62.5$ ksi. Although use of the selected HSS grade was not common for the frames designed in 2010, the steel grade was kept the same for braces of both 2010 and 2016 designs to ease the comparison between the frames. Braces were designed such that they buckle out of the plane of the frame using a linear hinge zone in the gusset plate (Astaneh-Asl et al., 1985) as specified in the AISC *Seismic Design Manual* (AISC, 2018) to trigger out-of-plane buckling. An effective length

of 0.45 times the total length of the brace, which is measured between the brace working points, was used in design to account for the lateral bracing provided by the brace acting in tension (Wakabayashi et al., 1974; Nakashima and Wakabayashi, 1992; El-Tayem and Goel, 1985, 1986; Sabelli and Hohbach, 1999). An identical HSS 3½×3½×¼ section was selected for braces of both tiers, even though the brace

design forces and lengths are slightly different in the tiers. The brace design axial compression strengths were determined from the AISC *Specification* Chapter E to be $P_{c,b1} = 48$ kips and $P_{c,b2} = 51$ kips in Tiers 1 and 2, respectively. The selected section complies with the width-to-thickness ratio limit $b/t = 12 < 14$ as required for highly ductile members in AISC *Seismic Provisions* Section F2.5a. The global
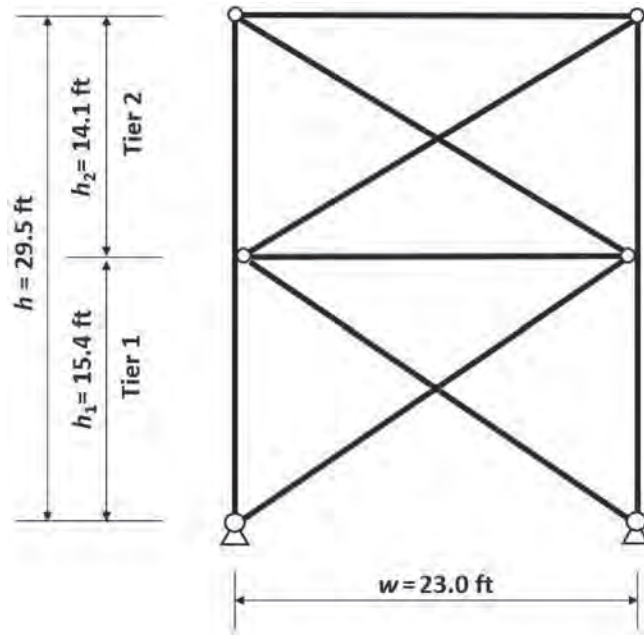
(a) Geometry of two-tiered SCBF selected for case study
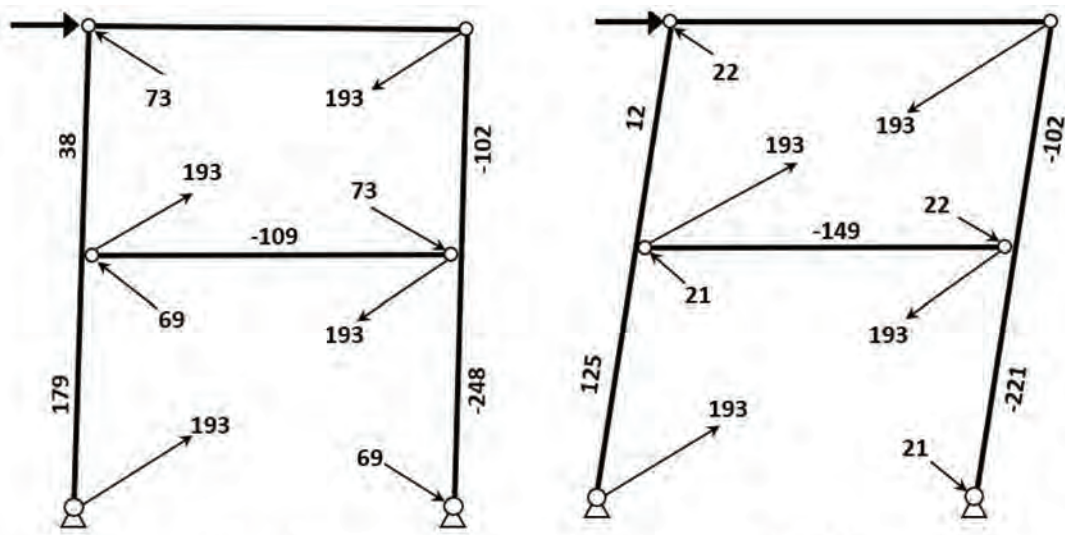
Case A

(b) Analysis case A*

Case B

(c) Analysis case B*

* No column bending moment considered.

Fig. 4 (a–c). Geometry and internal member forces for the different seismic analyses of SCBFS (forces in kips).

slenderness ratios for braces in Tiers 1 and 2 are $L/r = 113$ and 110, respectively, which are less than the limit (i.e., 200) prescribed by AISC *Seismic Provisions* Section F2.5b.

Column Design

The columns of the selected braced frame were designed using two design methodologies, 2010 and 2016 AISC *Seismic Provisions*, to illustrate the design procedures and
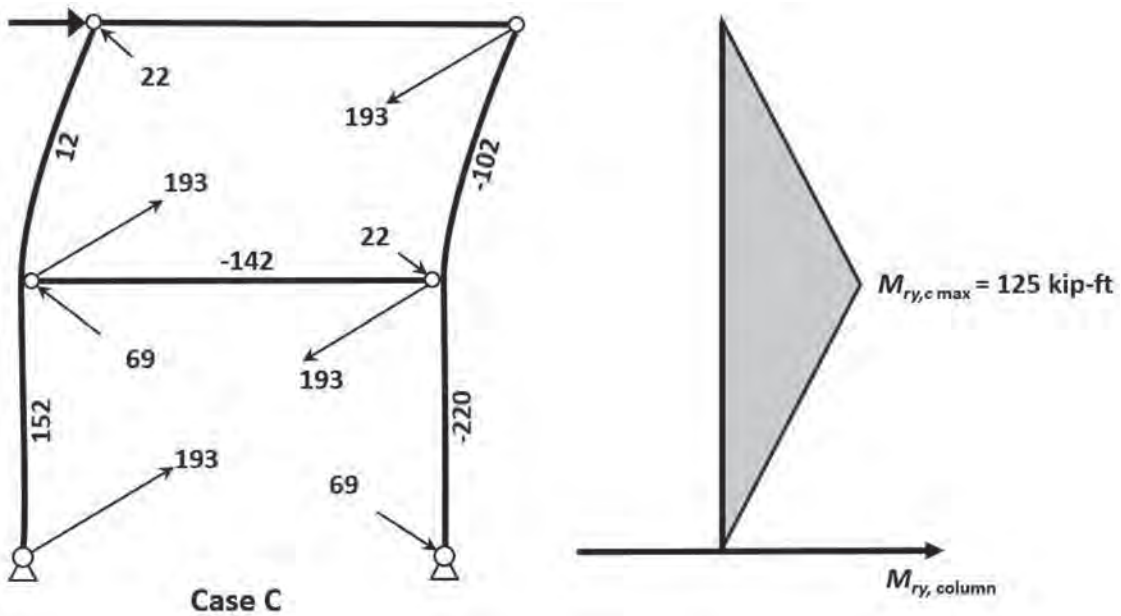
examine the seismic performance, in particular, the stability of columns.

2010 Design

The frame with the columns designed using the 2010 AISC *Seismic Provisions* is referred to as the 2010 design. The columns were designed to resist the axial compression force due to gravity loads $P_{G,c} = 51$ kips plus the maximum axial
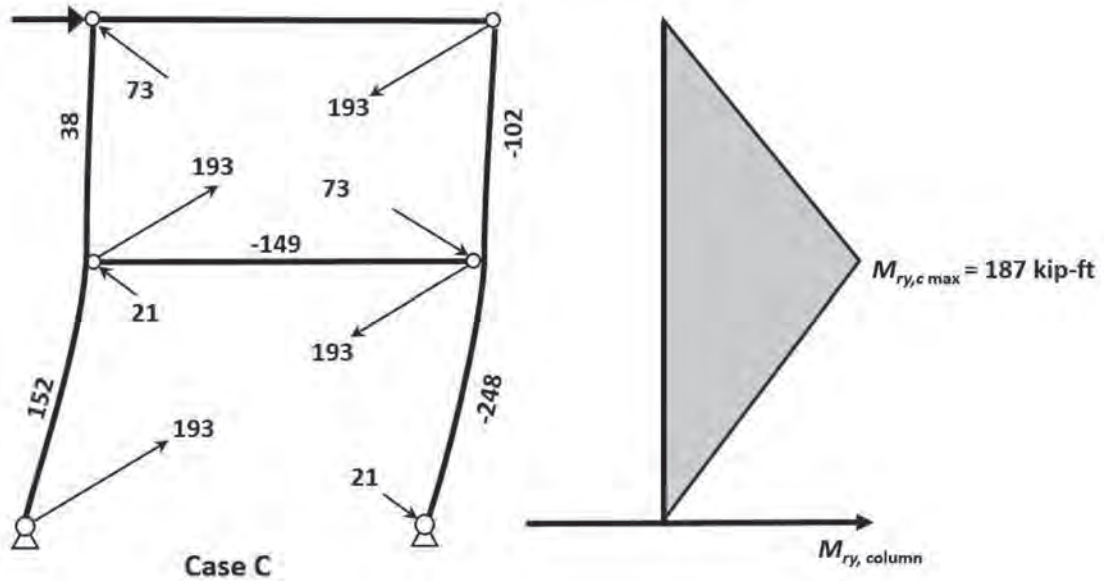
(d) Analysis case C with critical Tier 1

(e) Analysis case C with critical Tier 2

Fig. 4 (d–e). Geometry and internal member forces for the different seismic analyses of SCBFS (forces in kips).

load induced by the vertical components of brace forces when they reach their resistance in tension and compression. For the latter, two analysis cases are prescribed by the 2010 AISC *Seismic Provisions* Section F2.3 as shown in Figures 4(b) and 4(c). The maximum seismic axial compression force $P_{E,c}$ = 248 kips was obtained under analysis case A. The required column axial strength is $P_{r,c}$ = 299 kips. The columns are made of ASTM A992 steel (ASTM, 2015b) with a yield stress F_y = 50 ksi. To determine the flexural buckling resistance in the strong-axis and flexural-torsional buckling resistance of the column, the full-frame height was used, whereas, the weak-axis flexural buckling resistance was computed using the length of the column equal to the height of the first tier as the strut provides lateral support in the plane of the frame. The effective length factors K_x = 0.84, K_y = 0.80, and K_z = 1.0 were used to compute the column effective length factors in strong-axis, weak-axis, and torsion, respectively. The effective length factors for flexural buckling modes, K_x and K_y, were obtained using an Eigen buckling analysis of an individual column under the loads applied at the roof and tier levels using S-Frame software (S-Frame, 2017). A W16×45 column conforming to ASTM A992 Grade 50 steel (ASTM, 2015b) with yield stress F_y = 50 ksi was selected for the 2010 design as the lightest cross-section based solely on the axial demand since there are no flexural moments considered in design. The column design axial strength is equal to $P_{c,c}$ = 313 kips. Although in practice the effective length factors are generally taken equal to one, $K_x = K_y = K_z$ = 1.0, in this study the effective length factors smaller than unity were used as allowed by the AISC *Specification* Appendix 7.2 to account for the beneficial effect of distributed axial loads on MT-CBF columns (Dalal, 1969). Had effective length factors equal to one been used in design, a W14×48 column section would have been chosen.

2016 Design

The 2016 design represents the frame with the columns designed using the 2016 AISC *Seismic Provisions*. The required strength of the columns was determined using the most critical combination of the axial compression force and bending moment obtained from analysis cases A, B, and C as shown in Figures 4(b)–4(e). One major difference between the 2010 and 2016 design is that analysis case C, which represents the progressive buckling and yielding of the braces as shown in Figure 3(c), is required in the 2016 design. Analysis case C resulted in the most critical demands on the columns as illustrated in Figure 4(d), including an axial compression force equal to $P_{r,c}$ = 299 kips due to the brace resistances plus the gravity load and an in-plane flexural bending moment $M_{ry,c}$ = 187 kip-ft caused by non-uniform yielding of the braces between two adjacent tiers. To calculate the in-plane bending moment in the columns, the critical tier was first identified by comparing the story

shear resistance between the tiers: $V_{exp,1}$ = 218 kips < $V_{exp,2}$ = 228 kips. The shear resistance was obtained from the summation of the horizontal components of the brace resistances in tension and compression $V_{exp} = (T_{exp} + C_{exp}) \cos\theta$, where θ is the angle between the brace and the horizontal plane. Comparing the shear resistances shows that Tier 1 has the least shear resistance and therefore is the critical tier. However, because the difference between the shear resistances is small, analysis case C was repeated assuming critical Tier 2 as shown in Figure 4(e). The case where the critical tier is Tier 1 resulted in the most critical combination of the axial compression force and flexural bending moment. The design in-plane bending moment of the column $M_{ry,c}$ is calculated using Equation 1 and the unbalanced brace story shear force ΔV_{br} as described in Imanpour et al. (2016b).

$$M_{ry,c} = \frac{\Delta V_{br} h_1}{1 + (h_1/h_2)} \tag{1}$$

where ΔV_{br} is the unbalanced brace story shear computed as follows:

$$\Delta V_{br} = (T_{exp} + C_{exp})_2 \cos\theta_2 - (T_{exp} + C'_{exp})_1 \cos\theta_1 \tag{2}$$

For the frame shown in Figure 4(d), the unbalanced brace story shear and design in-plane bending moment in the columns are equal to ΔV_{br} = 51 kips and $M_{ry,c}$ = 187 kip-ft (0.66 times the nominal plastic flexural strength in the weak-axis M_{py}), respectively. This was obtained assuming that the column is pinned in the plane of the frame at the roof and base levels.

As prescribed by the 2016 AISC *Seismic Provisions*, an additional out-of-plane bending moment demand equal to $M_{rx,c}$ = 4.2 kip-ft (0.007 times the nominal plastic flexural strength in the strong-axis M_{pxs}) was calculated, arising from the out-of-plane notional load applied at the tier level plus the brace out-of-plane buckling. The former effect was calculated by applying an out-of-plane horizontal notional load at the tier level that is 0.006 times the vertical component of the buckling strength of the Tier 2 brace; this force was amplified by multiplier B_1 = 1.16 to account for the P-δ effect. Multiplier B_1 was calculated using the method specified in 2016 AISC *Specification* Appendix 8.2. The latter effect need not exceed forces corresponding to the flexural resistance of the brace connections and was equal to $1.1R_y M_p/\alpha_s$, where R_y is the ratio of expected yield stress to the specified minimum yield stress, M_p is the corresponding plastic bending moment of the brace, and α_s is the LRFD force level adjustment factor taken equal to 1.0. A W12×96 column conforming to ASTM A992 Grade 50 steel was selected to carry the gravity plus seismic-induced forces for the frame of Figure 4(a). Note that had the effective length factors K_x, K_y, and K_z been set equal to 1.0, the column section would have remained unchanged. For the selected column, the axial strength, strong-axis flexural strength, and

weak-axis flexural strength are $P_{c,c} = 1{,}020$ kips, $M_{cx,c} = 552$ kip-ft, and $M_{cy,c} = 255$ kip-ft, respectively. The column resistance was verified using the interaction equation given in AISC *Specification* Section H1.1:

$$\frac{P_{r,c}}{P_{c,c}} + \frac{8}{9}\left(\frac{M_{rx,c}}{M_{cx,c}} + \frac{M_{ry,c}}{M_{cy,c}}\right) \leq 1.0 \qquad \text{(from \emph{Spec.} Eq. H1-1a)}$$

$$\frac{299 \text{ kips}}{1{,}020 \text{ kips}} + \frac{8}{9}\left(\frac{4.20 \text{ kip-ft}}{552 \text{ kip-ft}} + \frac{187 \text{ kip-ft}}{255 \text{ kip-ft}}\right) \leq 1.0$$

$$0.95 < 1.0 \quad \textbf{o.k.}$$

Strut Design

The maximum axial compression force equal to $P_{r,s} = 149$ kips was induced in the strut under analysis case B in Figure 4(c) for both the 2010 and 2016 designs. This analysis case corresponds to the brace loading scenario when the tension braces reach T_{exp} and C'_{exp} is developed in the compression braces of both tiers. As required by the 2016 AISC *Seismic Provisions*, when braces buckle out-of-plane, in addition to the axial compression force a flexural moment induced by brace buckling was considered in design; however, the torsional moment need not exceed the moment corresponding to the flexural resistance of the brace connections. Although the design forces between two designs are not identical, a W10×45 section made of ASTM A992 Grade 50 steel satisfies both designs. For the 2010 design, the strut was oriented such that the web is in the vertical plane; however, the web of the strut was placed in the horizontal plane for the 2016 design so that it can provide torsional bracing at the strut-to-column connections through its strong-axis moment capacity (Imanpour et al., 2016a; Stoakes and Fahnestock, 2014). This detail for the 2016 design was selected to satisfy the 2016 AISC *Seismic Provisions* requirement to torsionally brace the MT-CBF columns at the strut-to-column location.

Drift Checks

The story drift must be verified for both designs as specified in ASCE/SEI 7-16 (ASCE, 2016). The maximum story drift allowed by this standard is 2.5% for the structures in risk category II. The design story drift, Δ_d, was calculated by multiplying the elastic drift $\Delta_e = 0.12\%$ for the 2010 design and $\Delta_e = 0.11\%$ for the 2016 design by the deflection amplification factor $C_d = 5$ and divided by the importance factor $I_e = 1$: $C_d \Delta_e / I_e = 0.6\%$ and 0.55% for the 2010 and 2016 designs, respectively. Both design story drifts satisfy the story drift limit prescribed by ASCE/SEI 7-16. Note that the elastic drift Δ_e can be calculated manually using structural analysis principles or using a structural analysis program under the design seismic force.

An additional drift limit is imposed by the 2016 AISC

Seismic Provisions for individual braced tiers in MT-SCBFs to prevent premature brace failure due to excessive tier drifts (Tremblay et al., 2003; and Hsiao et al., 2013). It is required that the drift in each braced tier be limited to 2% of the tier height when the frame is subjected to the design story drift. This check was only performed for the 2016 design at the critical tier, which experiences the largest tier drift among the braced tiers. To calculate the critical tier drift, it was assumed that the tier drift is composed of two components: (1) the overall frame drift represented by a linear variation over the length of the frame Δ_F and (2) the distortion due to column bending caused by the unbalanced brace story shear ΔV_{br}. When the first tier is the critical tier, Equation 4 gives the first-tier drift:

$$\Delta_1 = \Delta_{F,1} + \left(\frac{V_{br}}{2}\right)\left(\frac{h_1 h_2^2}{3EI_c h}\right) \leq 2\% \qquad (4)$$

where $E = 29{,}000$ ksi is the Young's modulus of steel, and I_c is the moment of inertia of the column about the weak-axis of the section.

The overall frame drift Δ_F is equal to the design story drift, $\Delta_d = 0.55\%$; therefore, $\Delta_{F,1} = 0.55\%$. To calculate the distortion due to column bending, the unbalanced brace story shear was calculated using the Case B forces shown in Figure 4(c), assuming that the compression braces in both tiers have experienced several inelastic cycles and reached their expected post-buckling capacity, while tension braces have reached their yield force and experienced significant elongations at least in one tier:

$$\begin{aligned}\Delta V_{br} &= \left(T_{exp} + C'_{exp}\right)_2 \cos\theta_2 - \left(T_{exp} + C'_{exp}\right)_1 \cos\theta_1 \qquad (5)\\ &= (193 \text{ kips} + 22 \text{ kips})\cos 31.6° - \\ &\quad (193 \text{ kips} + 21 \text{ kips})\cos 33.9° \\ &= 5.40 \text{ kips}\end{aligned}$$

The drift in Tier 1 obtained using Equation 4 is equal to $\Delta_1 = 0.74\%$, which meets the 2% limit prescribed by the 2016 AISC *Seismic Provisions*. A similar check was performed assuming Tier 2 as the critical tier, which resulted in a critical tier drift equal to 0.76% and, therefore, satisfying the 2% limit as well. Thus, the selected column for the 2016 design satisfies the story drift and tier drift checks. Figures 5(a) and 5(b) show the final members selected for the 2010 and 2016 designs, respectively.

SEISMIC PERFORMANCE EVALUATION

Braced Frame Numerical Model

The three-dimensional finite element models of the two-tiered concentrically braced frames designed in accordance with the 2010 and 2016 AISC *Seismic Provisions* were developed using the *ABAQUS* program (ABAQUS, 2014).

The numerical model of the frame is shown in Figure 6. The frame connections were designed in accordance with the AISC *Seismic Design Manual* (AISC, 2018). All connections, excluding the column base connection, were included in the numerical models. Frame connections were designed as welded connections in accordance with AISC *Seismic Design Manual*; however, welds were not explicitly simulated in the numerical model; instead, connection plates and structural members were tied in their intersections. Three-dimensional deformable shell elements (S4R) were used to simulate braces, columns, struts, and connections. A finer mesh was used in the connection zones to better reproduce local effects. Material nonlinearity was incorporated through the Maxwell-Huber-Hencky-von Mises yield criterion with associated flow rule. The nonlinear kinematic/isotropic cyclic hardening model in *ABAQUS* was chosen to simulate the inelastic cyclic behavior of steel. The parameters used to define the hardening model were obtained from Suzuki and Lignos (2015). Geometric nonlinearities were incorporated in the models through the use of a large-displacement formulation. Young's modulus of elasticity and Poisson's ratio were assumed as 29,000 ksi and 0.3, respectively. The yield stress $R_yF_y = 62.5$ ksi and $F_y = 50$ ksi were assigned to the braces and other members, respectively.

The base of the columns and bottom-edge of the base gusset plates were constrained to a reference point at the center of the column. The three translational degrees-of-freedom (DOFs) along with the torsional degree-of-freedom were fixed at the reference point. The reference point was free to rotate in and out of the plane of the frame to simulate a pinned base condition of the braced frame columns.

Similarly, at the top of each column, the web and flanges were constrained to a reference point at the middle of the web of the column. These reference points at the top of the columns were restrained from out-of-plane movement and twist. The reference points at the top were free to move in the plane of the frame and rotate in and out of the plane of the frame.

Initial geometric imperfections corresponding to the first buckling mode of the members, which were obtained from an eigenvalue buckling analysis, were assigned to columns and braces. The amplitude of the initial geometric imperfection was taken equal to 1/1000 times the unbraced length of the member in the direction of buckling (AISC, 2016c). For the columns, the total height of the frame was used for the out-of-plane direction, and the tier heights were used for the amplitudes in the plane of the frame. For the braces, the imperfections were only considered in the out-of-plane direction within the half of the brace length. Initial residual stresses were incorporated in wide-flange sections based on the pattern proposed by Galambos and Ketter (1958). A leaning column was also included in the model to account for large P-Δ effects. The leaning column was simulated using a deformable wire element and pin connected at its base and top. The in-plane horizontal displacement of the leaning column was constrained to the lateral displacement of the braced frame at the roof level. Additional information on the numerical model development and calibration can be found in Cano (2019).

Inertial forces developed at the roof level were reproduced using two point masses at the top end of the braced frame columns. The masses represent the weight equal to

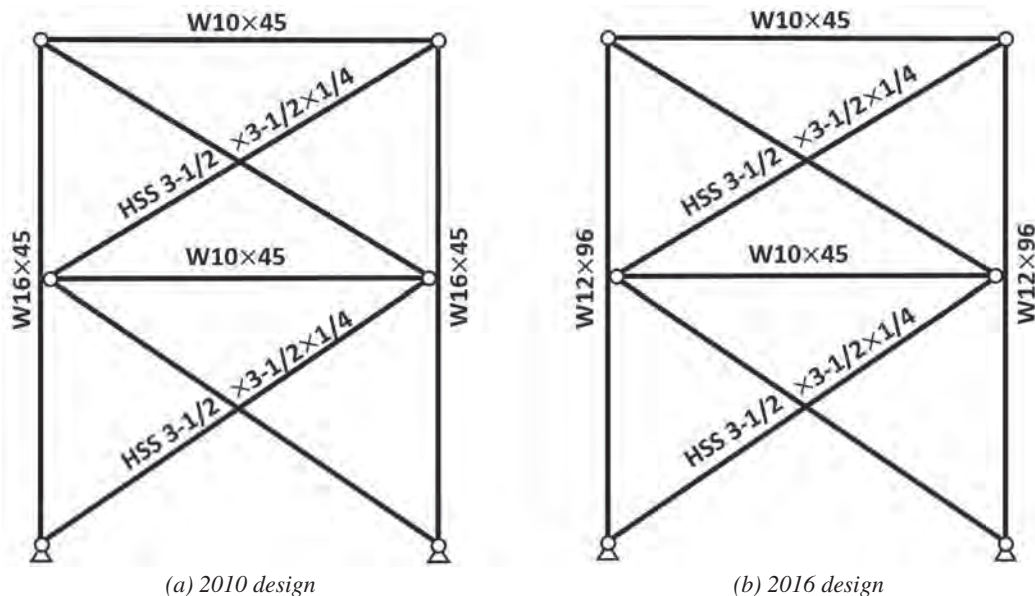*(a) 2010 design*   *(b) 2016 design*

Fig. 5. Selected members for two-tiered SCBF.

one-eighth of the total building seismic weight. The masses corresponding to the self-weight of the strut, roof beam, and connections were assigned as mass densities. However, only 0.1% of the mass density corresponding to the braces and columns was input in the mass definition to overcome the overshoot effect in the prediction of brace buckling response (Kazemzadeh Azad et al., 2018). Damping was defined using the Rayleigh's damping method to generate the damping forces under dynamic loading.

Nonlinear static (pushover) and dynamic analyses were performed on both 2010 and 2016 models. Each analysis was carried out in two steps. A gravity load of 51 kips was applied at the top end of each column in the first step using the static/general procedure. The gravity load equal to 675 kips corresponding to the adjacent gravity columns in the selected building was also applied at the top end of the leaning column in the same step. Once the gravity loads were applied, the lateral seismic load was applied. For the nonlinear static analysis, the frame was subjected to a cyclic horizontal displacement history at its roof level using a similar static/general procedure. For the nonlinear dynamic analysis, a set of ground motion accelerations were applied to the base of the frame and leaning column in the horizontal direction. Note that the inertia masses were only included in the dynamic analysis. To perform the dynamic analysis, the dynamic implicit procedure was selected, which uses the Newton-Raphson method to solve the nonlinear dynamic equilibrium.

Loading History for Nonlinear Static Analysis

Figure 7 shows the horizontal displacement history applied to the frames at the roof level. The displacement history consists of 14 cycles in which the first 10 cycles were obtained from the displacement history prescribed for prequalification of buckling restrained braces (BRBs) in 2016 AISC *Seismic Provisions* Appendix K plus four additional cycles: two cycles with the peak displacement corresponding to three times the frame design story drift and the last two cycles corresponding to four times the design story drift. The largest displacement cycle was selected to reproduce the maximum roof displacement observed in the dynamic analysis of the frame (see Table 1). In Figure 7, δ_y is the story drift corresponding to brace tensile yielding, and $C_d\delta_e$ is the frame design story drift per ASCE/SEI 7-16.
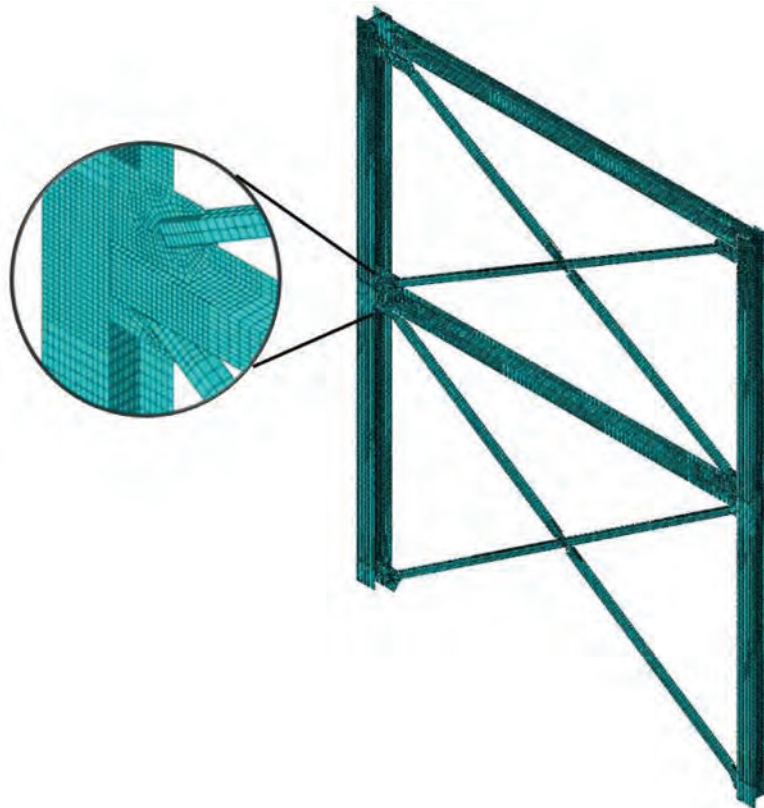

Fig. 6. Finite element model of the two-tiered concentrically brace frame (leaning column not shown for clarity).

Ground Motion Acceleration for Nonlinear Dynamic Analysis

The set of ground motion accelerations used to perform the dynamic analysis comprises the horizontal component of 40 historical ground motions. The ground motion records were selected and scaled using the method proposed by Dehghani and Tremblay (2016) to match, on average, the code-prescribed MCE_R response spectra as given in ASCE 7 at the fundamental period of the braced frame. The selection and scaling methods are described in detail in Dehghani (2016). The ensemble contains 14 records representing crustal earthquakes (0–185 miles), 21 records representing interplate earthquakes (45–185 miles deep), and 5 records representing in-slab earthquakes (185–440 miles).

Nonlinear Static Analysis Results

The results obtained from the nonlinear static (pushover) analysis of the 2010 and 2016 designs are presented in this section. Figures 8(a) and 8(b) show the drift demands in both tiers for the 2010 and 2016 designs, respectively. For both designs, the drifts in both braced tiers are nearly identical through the first six cycles before the story drift reaches 0.6%. Brace buckling took place in both tiers in the seventh cycle. Brace yielding was then initiated in the critical Tier 1, as expected in design. In the 2010 design, however, the subsequent brace elongation in tension led to a significantly larger drift in this tier compared to Tier 2, which remained essentially elastic through the entire analysis. The nonuniform distribution of drift demands was observed in the

subsequent cycle, which eventually led to column instability in the first-tier segment of the right-hand-side (RHS) column of the 2010 design. Column buckling occurred under the combination of large in-plane bending moment and axial compression force demands. Figure 9(a) shows the deformed frame shape at the initiation of column buckling. The analysis stopped just at the column buckling due to numerical convergence issues at 2.0% story drift.

The response of the 2016 design was significantly different than the 2010 counterpart. Brace tensile yielding developed in Tier 2 at 0.76% story drift, which reduced the nonuniformity of lateral inelastic deformations along the frame height. As shown in Figure 8(b), inelastic frame lateral deformations were distributed more uniformly between the tiers. Nevertheless, tier drift in critical Tier 1 was still higher than the one in noncritical Tier 2. No column instability was observed in the 2016 design. The frame deformed shape at the maximum story drift applied (i.e., 2.1%) is shown in Figure 9(b).

The brace axial forces in both tiers were normalized by the maximum expected tensile strength, AR_yF_y where A is the cross-sectional area of the brace and R_yF_y is the expected yield stress, and plotted against the tier drift in Figures 10(a) and 10(b) and Figures 10(c) and 10(d) for 2010 and 2016 designs, respectively. For the 2010 design, the tension brace in Tier 2 remained essentially elastic. Although the compression brace experienced buckling in compression, the buckling capacity was not significantly reduced; however, the braces in Tier 1 underwent severe inelastic deformations due to severe buckling and yielding. In contrast, the braces
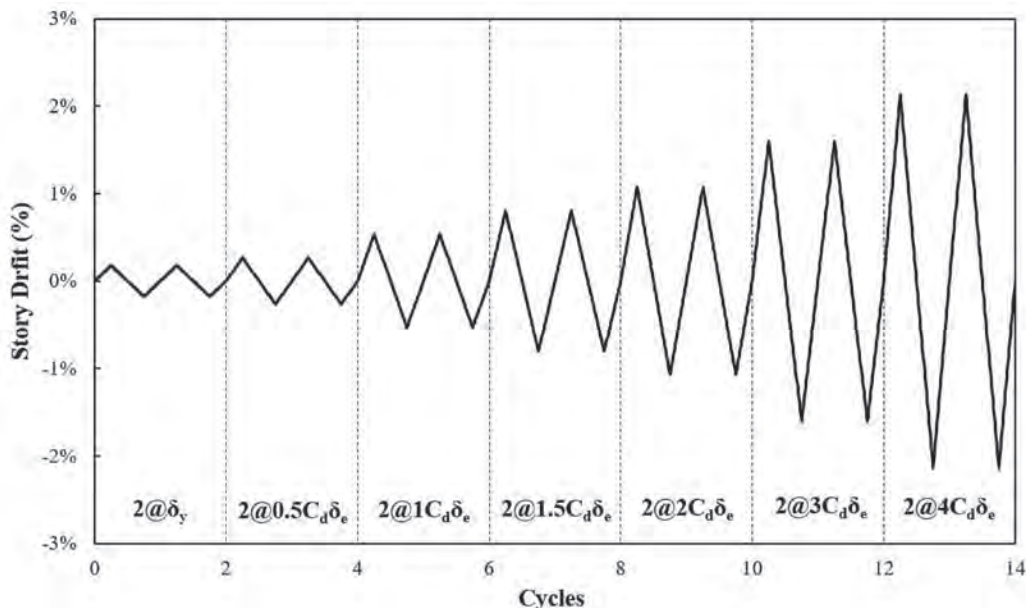
Fig. 7. Horizontal displacement history.

in both tiers of the 2016 design contributed to the inelastic response of the frame through yielding and buckling as shown in Figures 10(c) and 10(d).

Column in-plane bending moments recorded just below the brace-to-column connection were plotted against the story drift for 2010 and 2016 designs in Figures 11(a) and 11(b), respectively, to determine how the differential tier drifts can affect the bending moment demand on the column. The results are only presented for the critical RHS column, which is in compression when column buckling takes place in the 2010 design. The moments were normalized by the weak-axis plastic moment M_{py} of the corresponding section. The maximum normalized moment demand in the frame designed using the 2010 and 2016 AISC *Seismic Provisions* are 0.34 and 0.33, respectively. In 2016 design, the tension brace in Tier 2 yields at approximately 0.7% story drift, and the columns begins to straighten, which, combined with large-P-Δ effects, led to a nearly constant in-plane moment for the story drift exceeding 0.7% as shown in Figure 11(b). This is due to the combination of the moment arising from the decrease of the unbalanced brace story shear plus the P-Δ effects on the RHS column when it is under compression. It was also found that the design in-plane bending moment as per the 2016 AISC *Seismic Provisions* was largely overestimated (0.66M_{py} vs. 0.33M_{py}).

Column out-of-plane bending moments recorded just below the brace-to-column connection are plotted against the story drift for 2010 and 2016 designs in Figure 11(c) and 11(d), respectively. The moments were normalized by the strong-axis plastic moment M_{px} of the corresponding section. The columns of the 2010 and 2016 designs experienced a maximum out-of-plane demand of 17.0 kip-ft (0.05M_{px}) and 18.4 kip-ft (0.03M_{px}), respectively. The maximum

out-of-plane bending moment obtained for the 2016 design significantly exceeded the design value specified in the 2016 AISC *Seismic Provisions* (0.007M_{px} vs. 0.03M_{px}). However, it was observed that the maximum in-plane and out-of-plane moments generally do not co-exist. The maximum in-plane moments are experienced at story drifts that occur when the brace tensile yielding is initiated in the noncritical tier or higher (i.e., >0.7% story drift), but the out-of-plane moment value is driven by the compression brace force meeting the column at the tier level, and its maximum is achieved when the compression brace in the noncritical tier begins to buckle, which occurs at relatively small story drift.

The results obtained from the nonlinear static analysis suggest that the strength and stability of the column designed in accordance with the 2016 AISC *Seismic Provisions* is satisfactory even though the in-plane and out-of-plane bending demands are not accurately estimated in design. The overestimation of the in-plane moment demand can be attributed to the fact that the demand is calculated with a conservative assumption of brace expected strengths, which agrees with the other brace loading analysis cases [see Figures 2(a) and 2(b)] prescribed by the standard for multi-story SCBFs. The underestimation of the out-of-plane moment demand is not expected to have a significant impact on design due to relatively low moment demands compared to a large strong-axis moment capacity provided by the column selected to primarily resist the axial compression force and large weak-axis bending moment. For comparison, the interaction ratio is recalculated to be 0.62 using the measured column forces from the numerical analysis, which is lower than 0.95 obtained using design values, thus confirming the adequacy of the new column design requirements specified in 2016 AISC *Seismic Provisions*.
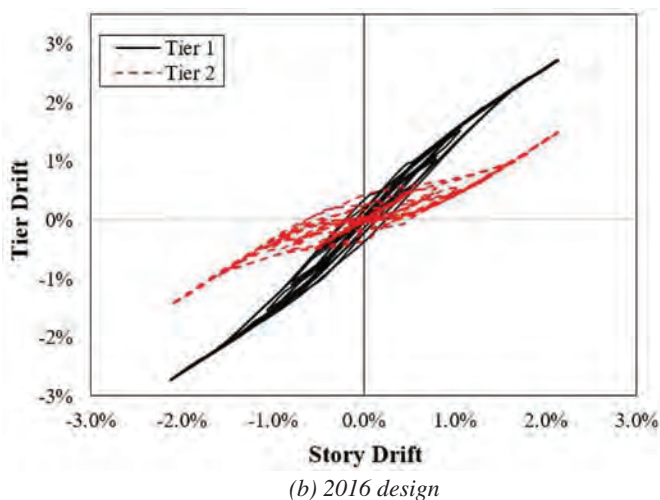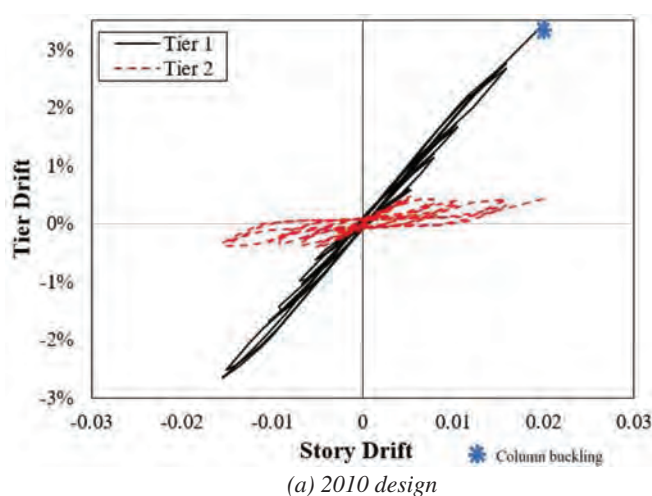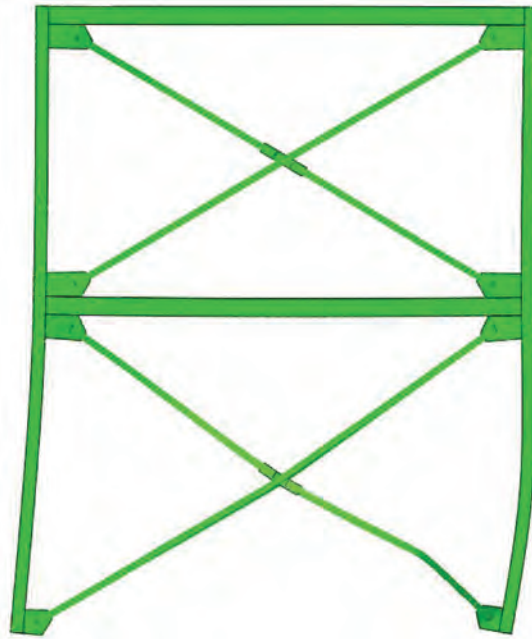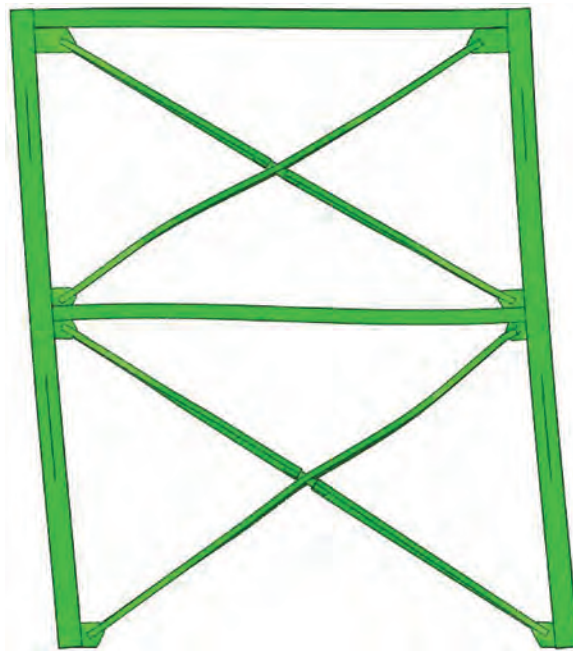

(a) 2010 design

(b) 2016 design

Fig. 8. Tier drift versus story drift.

(a) 2010 design at column buckling, 2.0% story drift

(b) 2016 design at maximum story drift 2.1%

Fig. 9. Frame deformed shape at peak story drift.

Nonlinear Dynamic Analysis Results

The results obtained from the nonlinear dynamic analysis of the 2010 and 2016 designs under 40 ground motion records are presented in this section.

2010 Design Overall Behavior

Column instability similar to the one observed using the static analysis method was observed for the 2010 design under 13 ground motion records out of the 40 ground motions analyzed. Column buckling triggered dynamic instability and led to frame collapse in all 13 cases. Figure 12 shows an example of the frame collapse under the 1994 Northridge ground motion record. Examining the results of the collapsed cases showed that the left-hand-side (LHS) column buckled upon reaching lower story drifts in comparison to the RHS column due to the direction of initial geometric imperfections, which favored the in-plane buckling of the LHS column. The in-plane flexural buckling was observed

first with a limited twist; the instability mode then changed to out-of-plane buckling due to the lack of out-of-plane support, resulting in a flexural-torsional buckling mode.

The statistics of the NonLinear Response History (NLRH) analysis results were used to evaluate the seismic response of the frames. Table 1 presents the results for the story drift, story drift ratio normalized by the design story drift $C_d\Delta_e$, drifts in Tiers 1 and 2, and drift ratios in Tiers 1 and 2 normalized by the story drift. For each parameter, the maximum, minimum, median and 84th percentile of the maximum recorded value under each ground motion are given. Note that the maximum, median, as well as the 84th percentile values were computed based on the ground motion records where the frame did not collapse. The story drifts range between 0.5% and 2.2% with a median value of 1.1%. Comparing the tier drift results for the non-collapse cases shows that drift in Tier 1 is approximately three times that of Tier 2, which confirms the finding of the static analysis and that brace tensile yielding only occurred in the critical tier.
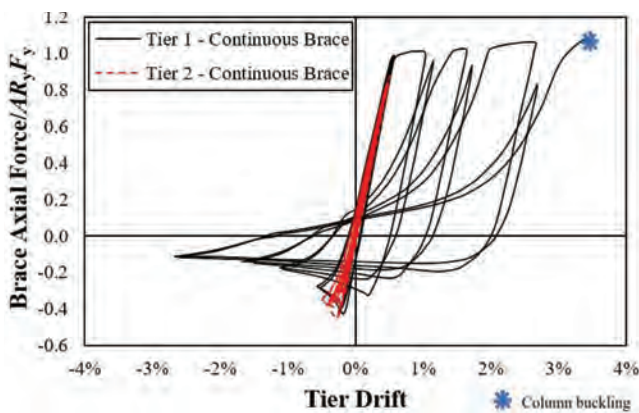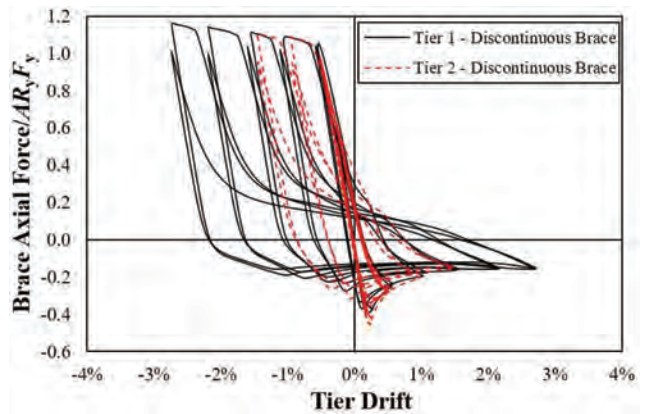

(a) 2010 design continuous braces
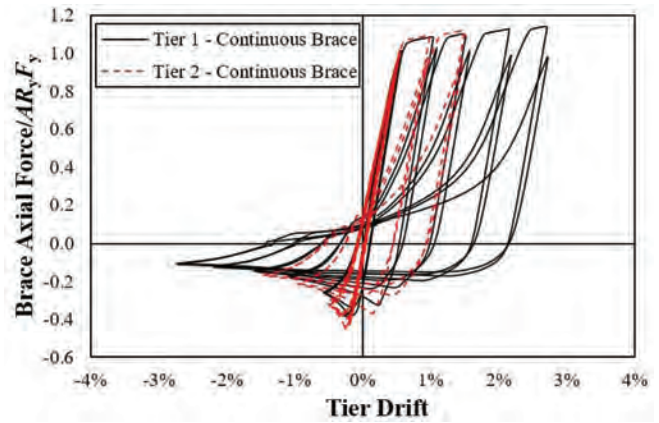
(b) 2016 design continuous braces
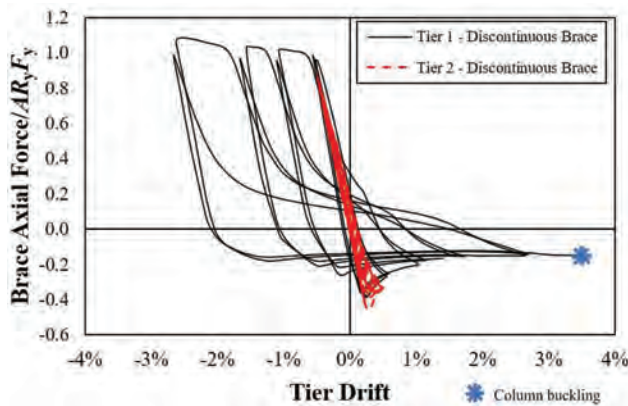
(c) 2010 design discontinuous braces

(d) 2016 design discontinuous braces

*Fig. 10. Normalized brace axial forces.*

| Table 1. Dynamic Analysis Statistics for Drift Response							
		Story Drift		Tier 1 Drift	Tier 2 Drift		
	Parameters	Δ	$\Delta/C_d\Delta_e$	Δ_1	Δ_2	Δ_1/Δ	Δ_2/Δ
2010 Design	Minimum	0.5%	0.8	0.5%	0.5%	1.0	1.0
	Maximum	2.2%	3.6	3.6%	0.6%	1.7	0.3
	Median	1.1%	1.9	1.7%	0.5%	1.5	0.4
	84th percentile	1.5%	2.5	2.4%	0.5%	1.6	0.4
2016 Design	Minimum	0.5%	0.9	0.5%	0.5%	1.0	1.0
	Maximum	2.6%	4.7	3.3%	1.9%	1.6	0.7
	Median	1.4%	2.5	2.0%	0.7%	1.4	0.5
	84th percentile	1.9%	3.5	2.6%	1.3%	1.5	0.7
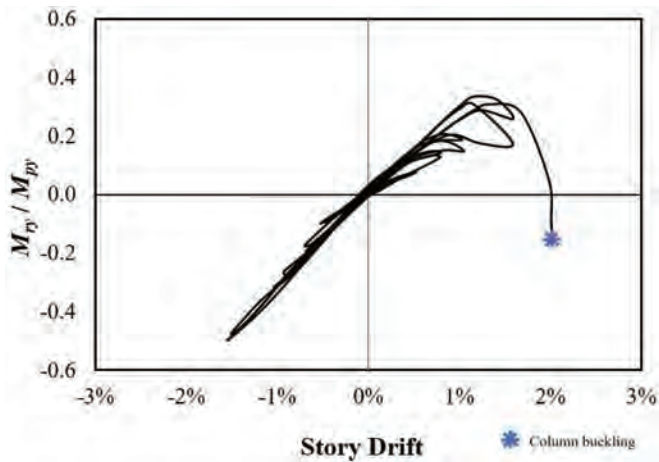
(a) 2010 design in-plane bending moment
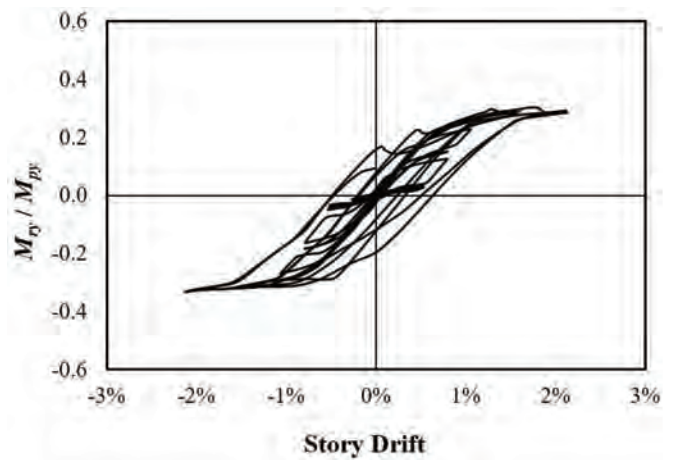
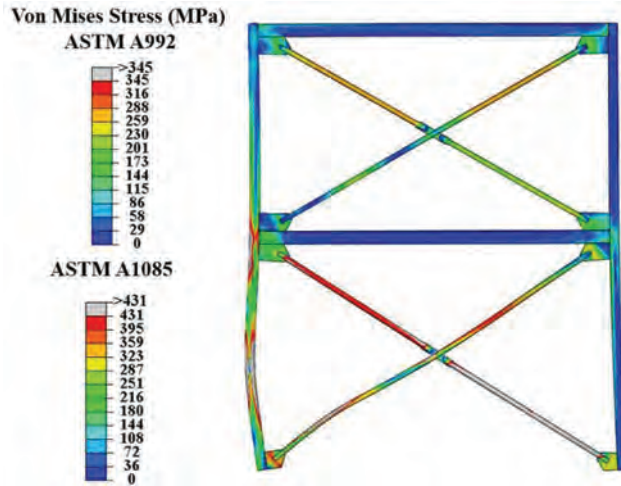*(b) 2016 design in-plane bending moment*
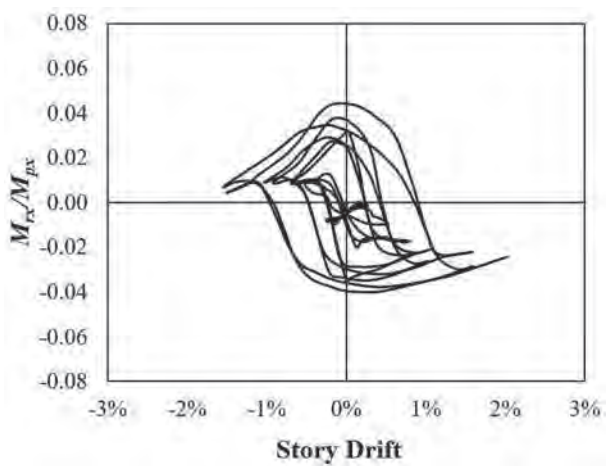
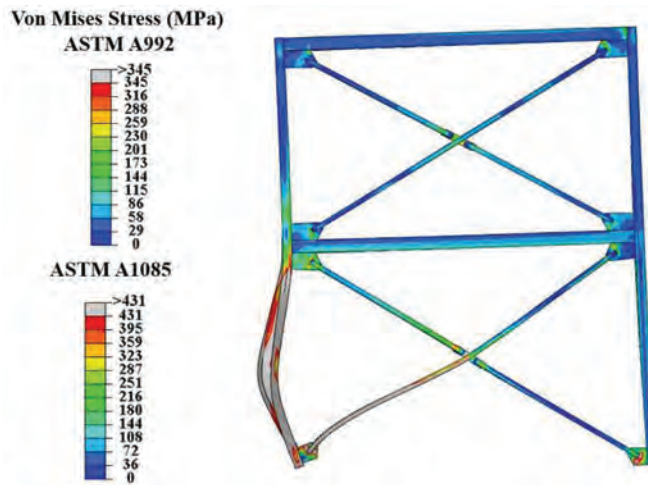*(c) 2010 design out-of-plane bending moment*
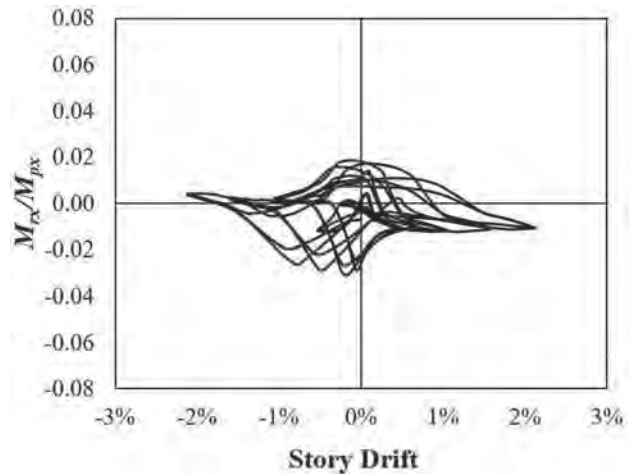
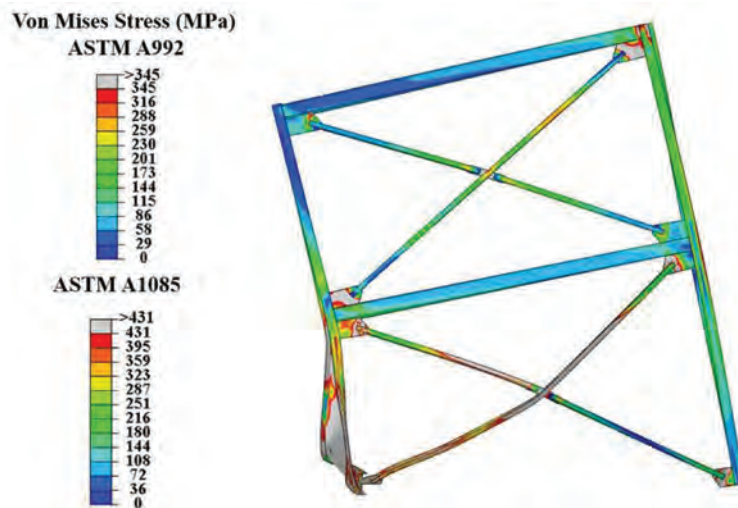*(d) 2016 design out-of-plane bending moment*

Fig. 11. RHS column moment demands.

(a) Onset of LHS column buckling at t *= 4.70 sec and story drift of 1.7%*

(b) LHS column buckling at t *= 5.38 sec*

(c) Frame collapse at t *= 5.49 sec*

Fig. 12. 2010 frame deformed shape under 1994 Northridge record.

Table 2. Dynamic Analysis Statistics for Column Demands							
	Parameters	M_{ry}/M_{py}	$M_{ry}/M_{ry,design}$	M_{rx}/M_{px}	$M_{rx}/M_{rx,design}$	P_r/P_n	$P_r/P_{r,design}$
2010 Design	Minimum	0.04	–	0.01	–	0.86	1.00
	Maximum	0.31	–	0.10	–	0.92	1.07
	Median	0.18	–	0.06	–	0.90	1.04
	84th percentile	0.28	–	0.08	–	0.91	1.06
2016 Design	Minimum	0.01	0.01	0.01	0.51	0.25	0.94
	Maximum	0.41	0.61	0.06	2.32	0.27	1.02
	Median	0.30	0.46	0.04	1.63	0.26	0.99
	84th percentile	0.35	0.53	0.05	1.96	0.26	1.00

2016 Design Overall Behavior

The results obtained for the 2016 design indicated that neither column buckling nor frame instability occurs under any of the 40 ground motion records. The summary of the frame displacement response is presented in Table 1. The median story drift is 1.4%, 2.5 times higher than the design story drift. The maximum story drift of 2.6% occurred under the 1979 Montenegro, Yugoslavia, earthquake. Note that the median story drift for the 2016 frame appears higher than the 2010 design; however, this is because the collapsed cases are not included in the calculation of median for the 2010 design.

The results of the tier drifts for the 2016 frame indicate that the tension brace in noncritical Tier 2 yields under the majority of the ground motion records, which significantly improved the distribution of inelastic lateral deformations over the height of the selected braced frame. Although the critical tier drift exceeded the limit prescribed by 2016 AISC *Seismic Provisions* (i.e., 2.0%) under a few major earthquakes, the median value of the critical tier drift 2.0% suggests that the stiffness design requirements specified in the 2016 AISC *Seismic Provisions* on average lead to a satisfactory drift response.

2010 Design Column Behavior

The statistics of the maximum column demands, including bending moments and axial forces for the 2010 and 2016 designs, are given in Table 2. The moment values were normalized by the corresponding plastic moment M_p (x and y are the strong and weak axis of the section, respectively), and axial forces were normalized by the nominal compressive strength. For the 2010 design, the axial forces were compared against the design value only because there were no moments used in design to compare against flexural demands. For the 2016 design, both the flexural moments and axial forces were compared against the designed values. Column moment demands were recorded for each ground motion just below the brace-to-column connection in Tier 1.

The results obtained for the 2010 frame indicate a high axial compression force that matches the design axial compression load is induced in the columns. Column in-plane and out-of-plane moments were not significantly large because the statistics only encompasses the noncollapse cases.

2016 Design Column Behavior

The axial force and moment values in the 2016 design show that the column capacity is shared between the axial force and biaxial bending moments as expected in design. However, the measured in-plane bending moment is lower than the value obtained using the current AISC *Seismic Provisions* because (1) brace tensile yielding does not occur under some of the ground motion records, and (2) the compression brace forces assumed in design to compute the unbalanced brace story shear (C'_{exp} in the critical tier and C_{exp} in noncritical tier) were found to be higher than C'_{exp} in the critical tier, due to the difference between the observed strength degradation at the post-buckling range and that expected in the standard to determine C'_{exp}, and lower than C_{exp} in the noncritical tier, due to slight strength degradation after achieving brace buckling.

Out-of-plane moments for the 2016 frame exceeded the design out-of-plane moment as per the 2016 AISC *Seismic Provisions* in 35 out of 40 cases with a median $M_{rx}/M_{rx,design}$ value of 1.63. The maximum out-of-plane moment tends to occur when the braces reach their maximum buckling capacity and generally do not coincide with the maximum in-plane moment. The out-of-plane moment was investigated further by differentiating the contributing components including (tension and compression) brace forces, strut forces, gusset plate plastic moments, and P-δ effects. It was found that the out-of-plane moment induced by the out-of-plane component of the brace forces and the P-δ effects are the key contributors to the out-of-plane bending moment of the compression column. The contribution from the braces on the out-of-plane moment of the columns was found not

only to be caused by the buckled compression braces, but also by the tension braces. This is because residual plastic deformations developed upon brace out-of-plane buckling result in an elongated brace in the subsequent tension cycle that creates out-of-plane forces on the column. However, such out-of-plane deformations in the tension brace were considerably smaller than those in the compression brace since the brace tends to straighten under the tension load. The results of the NLRH analyses showed that although the moment demands are not accurately predicted, the stability and strength of the column designed in accordance with the 2016 AISC *Seismic Provisions* are satisfactory.

CONCLUSIONS

This paper presents the seismic response of steel multi-tiered special concentrically braced frames designed in accordance with the 2010 and 2016 AISC *Seismic Provisions*. A detailed nonlinear finite element model of a two-tiered special concentrically braced frame capable of simulating the brace inelastic response and column instability modes was developed. This numerical model was analyzed under cyclic displacement demands and earthquake accelerations to assess the frame nonlinear lateral response and evaluate the column moment demands prescribed by the latest edition of the AISC *Seismic Provisions*. The main findings of this study are summarized as follows:

- The seismic response of both 2010 and 2016 frames predicted using cyclic nonlinear static analysis agrees well with that predicted using the nonlinear dynamic analysis.

- Inelastic frame deformations tend to concentrate in one of the braced tiers in the frame designed in accordance with the 2010 AISC *Seismic Provisions*. Such nonuniform lateral response led to column instability in the first-tier segment for the frame.

- Column instability in the 2010 design is influenced by the direction of the initial geometric imperfection assigned in the plane of the frame. Because the column instability is initiated by flexural buckling mode in the plane of the frame within a tier, the column with the initial geometric imperfection aligned with the direction of lateral displacement demand is more prone to instability.

- The seismic response of the frame designed in accordance with the 2016 AISC *Seismic Provisions*, where the columns were sized to resist additional in-plane and out-of-plane bending moments, was significantly improved compared to the frame designed to the 2010 AISC *Seismic Provisions*.

- Neither yielding nor instability occurred in the columns designed in accordance with the 2016 AISC *Seismic Provisions*.

- The column designed using the 2016 AISC *Seismic Provisions* possesses sufficient stiffness to trigger yielding in the noncritical tier under large story drifts, which allows for better distribution of inelastic frame deformations over the height of the frame.

- The median value of the peak tier drifts for the 2016 design as obtained from the nonlinear response history analyses is within the limit prescribed by the 2016 AISC *Seismic Provisions*.

- The results of nonlinear response history analyses performed on the 2016 design confirmed that the column axial force demand is appropriately predicted, the in-plane bending moment demand of the column is overestimated, and the out-of-plane bending moment demand of the column is underestimated. However, the underestimation of the out-of-plane moment demand did not have a detrimental effect on the frame seismic response.

Future numerical simulations should investigate a large number of multi-tiered steel concentrically braced frames with different geometries to further validate the 2016 AISC *Seismic Provisions* and improve further if necessary. In particular, the results of such studies can be used to evaluate torsional and out-of-plane demands of the column. Furthermore, the results obtained from the present numerical simulations should be validated using full-scale experimental tests on two-tiered concentrically braced frames once available.

REFERENCES

ABAQUS (2014), Dassault Systèmes, Waltham, Mass.

AISC (2010), *Seismic Provisions for Structural Steel Buildings*, ANSI/AISC 341-10, American Institute of Steel Construction, Chicago, Ill.

AISC (2016a), *Seismic Provisions for Structural Steel Buildings*, ANSI/AISC 341-16, American Institute of Steel Construction, Chicago, Ill.

AISC (2016b), *Specification for Structural Steel Buildings*, ANSI/AISC 360-16, American Institute of Steel Construction, Chicago, Ill.

AISC (2016c), *Code of Standard Practice for Steel Buildings and Bridges*, ANSI/AISC 303-16, American Institute of Steel Construction, Chicago, Ill.

AISC (2018), *Seismic Design Manual.* American Institute of Steel Construction, Chicago, Ill.

ASCE (2016), *Minimum Design Loads for Buildings and Other Structures*, ASCE/SEI 7-16, American Society of Civil Engineers.

Astaneh-Asl, A., Goel, S.C., and Hanson, R.D. (1985), "Cyclic Out-of-Plane Buckling of Double-Angle Bracing," *Journal of Structural Engineering,* ASCE, Vol. 111, No. 5, pp. 1,135–1,153.

ASTM (2015a), *Standard Specification for Cold-Formed Welded Carbon Steel Hollow Structural Sections (HSS),* A1085/A1085M-15, ASTM International, West Conshohocken, Pa.

ASTM (2015b), *Standard Specification for Structural Steel Shapes,* A992/A992M-11, ASTM International, West Conshohocken, Pa.

Black, R. Gary, Wenger, W.A., and Popov, E.P. (1980), "Inelastic Buckling of Steel Struts under Cyclic Load Reversal," Earthquake Engineering Research Center, University of California, Berkely, Calif.

Cano, P.A. and Imanpour, A. (2018), "Evaluation of Seismic Design Methods for Steel Multi-Tiered Special Concentrically Braced Frames," *Proceedings Structural Stability Research Council Annual Stability Conference 2018* (April 10–13). Baltimore, Md.

Cano, P.A. (2019), *Evaluation of the Seismic Design Methods for Steel Multi-Tiered Concentrically Braced Frames*, Master's Thesis, University of Alberta.

Cano, P.A. and Imanpour, A. (2019), "Dynamic Analysis of Steel Multi-Tiered Special Concentrically Braced Frames," *Structures Congress 2019,* Orlando, Fla. April 24–27, pp. 99–112.

Dalal, S. T. (1969), "Some Non-Conventional Cases of Column Design," *Engineering Journal,* AISC, Vol. 6, No. 1, pp. 28–39.

Dehghani, M. (2016), *Seismic Design and Qualification of All-Steel Buckling-Restrained Braced Frames for Canadian Applications*, Dissertation from Ecole Polytechnique Montreal, Order No. 10806518, Ecole Polytechnique, Montreal, Canada.

Dehghani, M. and Tremblay, R. (2016), "Robust Period-Independent Ground Motion Selection and Scaling for Effective Seismic Design and Assessment," *Journal of Earthquake Engineering*, Vol. 20, No. 2, pp. 185–218. DOI: 10.1080/13632469.2015.1051635.

El-Tayem, A.A. and Goel, S.C. (1985), "Cyclic Behavior of Angle X-Bracing with Welded Connections," Research Report No. UMCE 85-4, University of Michigan, Ann Arbor, Mich.

El-Tayem, A.A. and Goel, S.C. (1986), "Effective Length Factor for the Design of X-Bracing Systems," *Engineering Journal,* AISC, Vol. 24, No. 1, pp. 41–45.

Galambos, T.V. and Ketter, R.L. (1958), "Columns under Combined Bending and Thrust," Report 205A.21, Fritz Engineering Laboratory, Bethlehem, Pa.

Hsiao, P-C., Lehman, D.E., and Roeder, C.W. (2013), "A Model to Simulate Special Concentrically Braced Frames Beyond Brace Fracture," *Earthquake Engineering and Structural Dynamics*, Vol. 42, pp. 183–200.

Imanpour, A., Stoakes, C., Tremblay, R., Fahnestock, L., and Davaran, A. (2013), "Seismic Stability Response of Columns in Multi-Tiered Braced Steel Frames for Industrial Applications," *Proceedings of the 2013 SEI Structures Congress,* pp. 2,650–2,661.

Imanpour, A. and Tremblay, R. (2012), "Analytical Assessment of Stability of Unbraced Column in Two Panel Concentrically Braced Frames," *3rd International Structural Specialty Conference,* Edmonton, Alberta, Canada, Paper No. 1218.

Imanpour, A. and Tremblay, R. (2014), "Seismic Design of Steel Multi-Tiered Braced Frames: Application of Incremental Static Analysis for Design of Steel Multi-Tiered Braced Frames," *EUROSTEEL 2014,* September 10-14, Napoli, Italy.

Imanpour, A. and Tremblay, R. (2016), "Analysis Methods for the Design of Special Concentrically Braced Frames with Three or More Tiers for In-Plane Seismic Demand," *Journal of Structural Engineering*, Vol. 143, No. 4, 04016213.

Imanpour, A., Tremblay, R., Davaran, A., Stoakes, C., and Fahnestock, L.A. (2016a), "Seismic Performance Assessment of Multitiered Steel Concentrically Braced Frames Designed in Accordance with the 2010 AISC Seismic Provisions," *Journal of Structural Engineering,* Vol. 142, No. 12, 4016135.

Imanpour, A., Tremblay, R., Fahnestock, L.A., and Stoakes, C. (2016b), "Analysis and Design of Two-Tiered Steel Braced Frames under In-Plane Seismic Demand," *Journal of Structural Engineering*, Vol. 142, No. 2.

Imanpour, A., Tremblay, R., Leclerc, M., and Siguier, R. (2018), "Development of a Hybrid Simulation Computational Model for Steel Braced Frames," *Key Engineering Materials,* Vol. 763, pp. 609–618, Trans Tech Publications.

Kazemzadeh Azad, S., Topkaya, C., and Bybordiani, M. (2018), "Dynamic Buckling of Braces in Concentrically Braced Frames," *Earthquake Engineering Structural Dynamics*, Vol. 47, pp. 613–633. DOI: https://doi.org/10.1002/eqe.2982.

Nakashima, M. and Wakabayashi, M. (1992), "Analysis and Design of Steel Braces and Braced Frames in Building Structures," *Stability and Ductility of Steel Structures under Cyclic Loading*, Y. Fukumoto and G.C. Lee, eds., CRC Press, Boca Raton, Fla., pp. 309–321.

Sabelli, R. and Hohbach, D. (1999), "Design of Cross-Braced Frames for Predictable Buckling Behavior," *Journal of Structural Engineering*, Vol. 125, No. 2, pp. 163–168.

Schmidt, B.J. and Bartlett, F.M. (2002), "Review of Resistance Factor for Steel: Data Collection," *Canadian Journal of Civil Engineering*, Vol. 29, pp. 109–118.

S-Frame Software [Computer Software] (2017), Structural analysis software.

Stoakes, C.D. and Fahnestock, L. A. (2014), "Three-Dimensional Finite Element Simulation of the Seismic Behavior of Multitier Concentrically Braced Frames," *Procedings of Structures Congress 2014*, pp. 2,675–2,686.

Stoakes, C.D. and Fahnestock, L. A. (2016), "Strong-Axis Stability of Wide Flange Steel Columns in the Presence of Weak-Axis Flexure," *Journal of Structural Engineering*, ASCE, January, DOI: 10.1061/(ASCE)ST.1943-541X.0001448.

Suzuki, Y. and Lignos, D.G. (2015), "Large Scale Collapse Experiments of Wide Flange Steel Beam Columns," *Proceedings of the 8th International Conference on Behavior of Steel Structures in Seismic Areas (STESSA)*, Shanghai, China, July 1–3.

Tremblay, R., Archambault, M.-H., and Filiatrault, A. (2003), "Seismic Response of Concentrically Braced Steel Frames Made with Rectangular Hollow Bracing Members," *Journal of Structural Engineering*, Vol. 129, No. 12, pp. 1,626–1,636.

Wakabayashi, M., Matsui, C., Minami, K., and Mitani, I. (1974), "Inelastic Behavior of Full-Scale Steel Frames With and Without Bracings," *Bulletin of the Disaster Prevention Research Institute,* Kyoto University, Vol. 24, No. 216, pp. 1–23.

Technical Note

Notes on Determining Required Connector Strength in Built-up Compression Members

LOUIS F. GESCHWINDNER

INTRODUCTION

TC-4, the Member Design task committee of the AISC Committee on Specifications, was asked to provide guidance to the profession on determining the required strength of connectors in built-up compression members. The following, presented on behalf of the task committee, is based on material presented to the committee by Todd Helwig and derived in large part by Joseph Yura.

Connections between individual components of a built-up compression member carry no force when the member is perfectly straight in the unbuckled configuration under load. Yet AISC *Specification for Structural Steel Buildings* (AISC, 2016), hereafter referred to as the AISC *Specification*, Section E6.1, requires that the end connection of these built-up members be welded or connected by means of pretensioned bolts with Class A or B faying surfaces. Nothing is provided in the AISC *Specification* or *Commentary* to help the designer determine the required strength of these connectors. This paper suggests one way of determining these required strengths and provides two LRFD examples. Other assumptions may be used to derive different, but equally acceptable, required strengths.

REQUIRED CONNECTOR SHEAR FORCE

To determine the required connector shear force, the built-up compression member will be assumed to be out-of-straight by an amount equivalent to that for a rolled compression member and in the form of a sine curve. That out-of-straightness will be amplified to account for second-order effects and the shear force distribution will be determined based on that amplified out-of-straightness.

Louis F. Geschwindner, Professor Emeritus, The Pennsylvania University, State College, Pa., Senior Consultant, Providence Engineering Corp., and Chair of the Task Committee on Members of the AISC Committee on Specifications. Email: LFG@psu.edu

Figure 1 shows a built-up, double-angle compression member with an out-of-straightness, Δ, and an axial load, P. Figure 1(b) is a free-body diagram consisting of the left half of the member. For equilibrium in the deformed configuration, a moment, M, is necessary at the mid-point of the member. If the deformed shape is assumed to follow a sine curve, the moment equation taken about the deformed position may be written as

$$M_x = P\Delta \sin\frac{\pi x}{L} \tag{1}$$

The moment diagram is shown in Figure 1(c). Shear along the member is determined by taking the derivative of the moment so that

$$V_x = \frac{dM_x}{dx} = P\Delta \frac{\pi}{L}\cos\frac{\pi x}{L} \tag{2}$$

and the shear diagram is given in Figure 1(d). The maximum shear is at the end where $x = 0$. Thus, $V_{max} = P\Delta\pi/L$. The shear force per unit length at the interface of the connected angles is determined as

$$v_x = \frac{V_x Q_y}{I_y} = \frac{Q_y}{I_y}P\Delta\frac{\pi}{L}\cos\frac{\pi x}{L} \tag{3}$$

where Q_y is the first moment of the area of one angle about the y-axis of symmetry of the double-angle member, and I_y is the moment of inertia of the double-angle member about the y-axis.

Thus, the total shear force to be resisted between the midpoint of the compression member and its end is determined by integrating the shear force per unit length, Equation 3, from zero to $L/2$, giving

$$
\begin{aligned}
V_{Total} &= \int_0^{L/2} \frac{V_x Q_y}{I_y}dx \\
&= \frac{Q_y}{I_y}P\Delta\frac{\pi}{L}\int_0^{L/2}\cos\frac{\pi x}{L}dx \\
&= \frac{Q_y}{I_y}P\Delta\frac{\pi}{L}\Big|_0^{L/2}\frac{L}{\pi}\sin\frac{\pi x}{L} \\
&= \frac{Q_y P\Delta}{I_y}
\end{aligned} \tag{4}
$$

If there were connectors at the ends only, this would be the shear force these end connectors must be designed to resist.

However, if there are also intermediate connectors, these end connectors may not be required to provide as much resistance. Consider intermediate connectors at the third points of the length. The total shear force between midpoint and third point can be determined by integrating Equation 3 from $L/3$ to $L/2$.

$$V_{L/3} = \int_{L/3}^{L/2} \frac{V_x Q_y}{I_y} dx$$

$$= \frac{Q_y}{I_y} P\Delta \frac{\pi}{L} \int_{L/3}^{L/2} \cos\frac{\pi x}{L} dx$$

$$= \frac{Q_y}{I_y} P\Delta \frac{\pi}{L} \Big|_{L/3}^{L/2} \frac{L}{\pi} \sin\frac{\pi x}{L}$$

$$= \frac{Q_y P\Delta}{I_y}\left(\sin\frac{\pi}{2} - \sin\frac{\pi}{3}\right)$$

$$= 0.133\frac{Q_y P\Delta}{I_y} \tag{5}$$

Therefore, the connector at the one-third point only carries 13% of the total shear, and the end connector carries 87% of the total shear. For simplicity, the required strength of the end connectors is taken as the total shear, regardless of the number of intermediate connectors. Therefore,

$$V_r = V_{Total} = \frac{Q_y P\Delta}{I_y} \tag{6}$$

The displacement at the column midpoint, Δ, can be estimated by amplifying the initial out-of-straightness, Δ_o, by the second-order amplification factor, B_1, so that

$$\Delta = B_1\Delta_o \tag{7}$$

If the applied load is taken as the required strength, P_r, and Equation 7 is substituted into Equation 6, the required shear strength becomes

$$V_r = \frac{Q_y P\Delta}{I_y} = B_1\Delta_o P_r \frac{Q_y}{I_y} \tag{8}$$

The out-of-straightness tolerance for a rolled compression member, as given in ASTM A6-14 (ASTM, 2014), may be taken as $\Delta_o = 0.001L$, where L is the length of the member. Thus, Equation 8 becomes

$$V_r = 0.001 B_1 P_r \frac{LQ_y}{I_y} \tag{9}$$

The amplification factor, as given in AISC *Specification* Appendix 8, Equation A-8-3, is

$$B_1 = \frac{C_m}{1 - \alpha P_r/P_{e1}} \tag{10}$$

If the required strength is exactly equal to the available strength in the elastic region, using LRFD,

$$P_r = \phi P_n = 0.9(0.877 P_e) \tag{11}$$

Since $P_{e1} = P_e$, C_m is conservatively taken as 1.0, and $\alpha = 1.0$ (LRFD) or 1.6 (ASD), the amplification for LRFD becomes

$$B_1 = \frac{1}{1 - \dfrac{1.0(0.9)(0.877 P_e)}{P_e}} = 4.75 \tag{12}$$
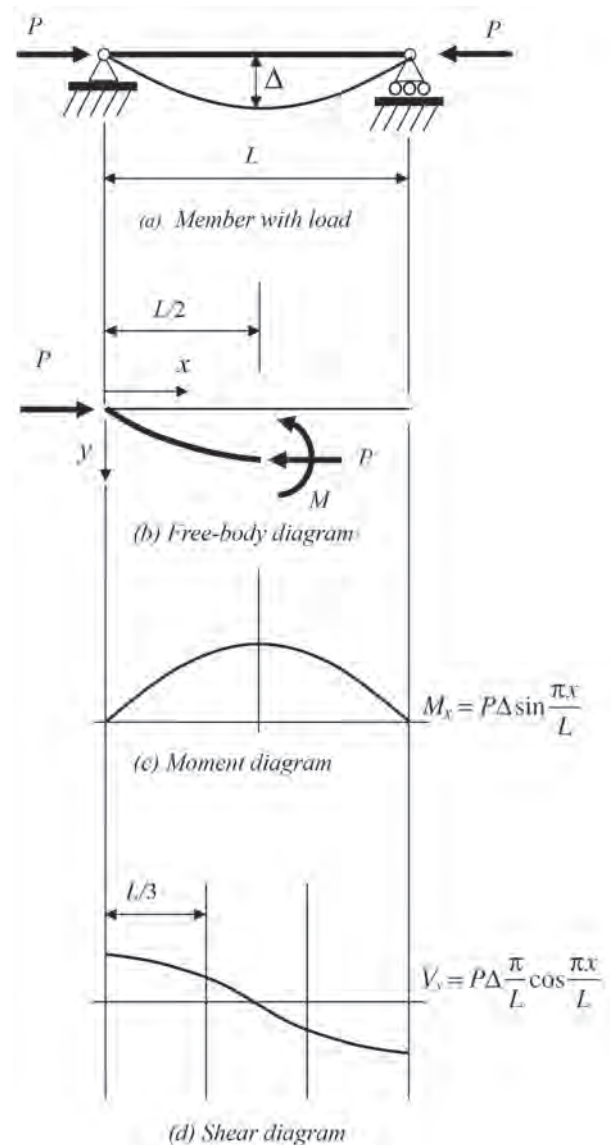

(a) Member with load

(b) Free-body diagram

$M_x = P\Delta \sin\dfrac{\pi x}{L}$

(c) Moment diagram

$V_x = P\Delta\dfrac{\pi}{L}\cos\dfrac{\pi x}{L}$

(d) Shear diagram

Fig. 1. Double-angle built-up compression member.

Thus, Equation 9 becomes

$$V_r = 0.001(4.75)P_r \frac{LQ_y}{I_y} = 0.00475 P_r \frac{LQ_y}{I_y} \qquad (13)$$

Because of the conservatism associated with the use of α to convert from ASD loads to ultimate loads for consideration of second-order effects, the amplification when required strength is exactly equal to available strength using ASD increases to $B_1 = 6.26$. Example 2 will show that it is not necessary to use these extreme B_1 values when the actual required strength is known and a better measure of second-order effects can be determined.

EXAMPLE 1

Given:

Determine the required end connectors for an ASTM A36 2L5×3×7⁄16 LLBB (3⁄8-in. separation) double-angle compression member, with length of 10 ft, using maximum second-order amplification. Use 3⁄4-in.-diameter Group A slip-critical bolts in standard holes. The required axial force is $P_u = 100$ kips (LRFD) and $P_a = 66.7$ kips (ASD).

Solution:

From the AISC *Steel Construction Manual* (AISC, 2017) Table 2-4, the material properties are as follows:

ASTM A36
$F_y = 36$ ksi
$F_u = 58$ ksi

From AISC *Manual* Table 1-7, the geometric properties are as follows:

L5×3×7⁄16 (single angle)
$A = 3.31$ in.^{2}
$I_y = 2.29$ in.^{4}
$\bar{x} = 0.722$ in.

The available strength in axial compression is taken from the bottom (*y-y* axis) portion of AISC *Manual* Table 4-9:

LRFD	ASD
$\phi_c P_n = 117$ kips > 100 kips **o.k.**	$\dfrac{P_n}{\Omega_c} = 78.0$ kips > 66.7 kips **o.k.**

For buckling about the *y-y* axis (axis of symmetry), the connectors will be in shear; thus, the geometric properties for the *y-y* axis are required.

$$I_{y\,double} = \sum (I_y + Ad^2)_{single}$$

$$= (2)\left\{ 2.29 \text{ in.}^4 + (3.31 \text{ in.}^2)\left[0.722 \text{ in.} + \left(\frac{3⁄8 \text{ in.}}{2} \right) \right]^2 \right\}$$

$$= 10.1 \text{ in.}^4$$

The first moment of the area of one angle about the *y*-axis of symmetry of the double-angle member, where $\bar{x}$ is the distance to the centroid for a single angle measured from the axis parallel to the axis of symmetry, is:

$$Q_y = A\left(\bar{x} + \frac{s}{2} \right)$$

$$= (3.31 \text{ in.}^2)\left[0.722 \text{ in.} + \left(\frac{3⁄8 \text{ in.}}{2} \right) \right]$$

$$= 3.01 \text{ in.}^3$$

Determine the required shear strength of the end connectors:

LRFD	ASD
From Equation 13: $$V_r = 0.00475 P_r \frac{LQ_y}{I_y}$$ $$= 0.00475(100 \text{ kips})\frac{(10 \text{ ft})(12 \text{ in./ft})(3.02 \text{ in.}^3)}{10.1 \text{ in.}^4}$$ $$= 17.0 \text{ kips}$$	From Equation 9, with $B_1 = 6.26$: $$V_r = 0.001 B_1 P_r \frac{LQ_y}{I_y}$$ $$= 0.001(6.26)(66.7 \text{ kips})\frac{(10 \text{ ft})(12 \text{ in./ft})(3.02 \text{ in.}^3)}{10.1 \text{ in.}^4}$$ $$= 15.0 \text{ kips}$$

Determine the required number of ¾-in.-diameter Group A slip-critical bolts in standard holes:

LRFD	ASD
From *Manual* Table 7-3: $$\phi r_n = 9.49 \text{ kips}$$ The required number of bolts is: $$\frac{V_r}{\phi r_n} = \frac{17.0 \text{ kips}}{9.49 \text{ kips}}$$ $$= 1.79$$ Use two ¾-in.-diameter Group A slip-critical bolts at each end in standard holes with a Class A or B faying surface.	From *Manual* Table 7-3: $$\frac{r_n}{\Omega} = 6.33 \text{ kips}$$ The required number of bolts is: $$\frac{V_r}{r_n/\Omega} = \frac{15.0 \text{ kips}}{6.33 \text{ kips}}$$ $$= 2.37$$ Use three ¾-in.-diameter Group A slip-critical bolts at each end in standard holes with a Class A or B faying surface.

EXAMPLE 2

Given:

Reconsider the problem of Example 1 if the second-order amplification is determined based on the actual required strength, Equation 10, rather than the maximum strength in the elastic region, as was done in Example 1.

Solution:

The elastic critical buckling strength is determined from AISC *Specification* Appendix 8, Equation A-8-5. From Example 1, $I_{y\ double} = 10.1 \text{ in.}^4$

$$P_{e1} = \frac{\pi^2 EI}{L_c^2} \qquad \text{(from \textit{Spec.} Eq. A-8-5)}$$

$$= \frac{\pi^2 (29{,}000 \text{ ksi})(10.1 \text{ in.}^4)}{[(10 \text{ ft})(12 \text{ in./ft})]^2}$$

$$= 200 \text{ kips}$$

The amplification factor, as given in AISC *Specification* Appendix 8, Equation A-8-3, is

LRFD	ASD
$$B_1 = \frac{C_m}{1 - \alpha P_r / P_{e1}}$$ $$= \frac{1.0}{1 - \frac{1.0(100\text{ kips})}{200\text{ kips}}}$$ $$= 2.00$$	$$B_1 = \frac{C_m}{1 - \alpha P_r / P_{e1}}$$ $$= \frac{1.0}{1 - \frac{1.6(66.7\text{ kips})}{200\text{ kips}}}$$ $$= 2.14$$

Determine the required shear strength of the end connectors using Equation 13:

LRFD	ASD
$$V_r = 0.001 B_1 P_r \frac{LQ_y}{I_y}$$ $$= 0.001(2.00)(100\text{ kips})\frac{(10\text{ ft})(12\text{ in./ft})(3.02\text{ in.}^3)}{10.1\text{ in.}^4}$$ $$= 7.18\text{ kips}$$	$$V_r = 0.001 B_1 P_r \frac{LQ_y}{I_y}$$ $$= 0.001(2.14)(66.7\text{ kips})\frac{(10\text{ ft})(12\text{ in./ft})(3.02\text{ in.}^3)}{10.1\text{ in.}^4}$$ $$= 5.12\text{ kips}$$

Determine the required number of ¾-in.-diameter Group A slip-critical bolts in standard holes:

LRFD	ASD
From *Manual* Table 7-3: $$\phi r_n = 9.49\text{ kips}$$ The required number of bolts is: $$\frac{V_r}{\phi r_n} = \frac{7.18\text{ kips}}{9.49\text{ kips}}$$ $$= 0.757$$ It would be acceptable to use one ¾-in.-diameter Group A slip-critical bolt at each end in standard holes with a Class A or B faying surface.	From *Manual* Table 7-3: $$\frac{r_n}{\Omega} = 6.33\text{ kips}$$ The required number of bolts is: $$\frac{V_r}{r_n/\Omega} = \frac{5.12\text{ kips}}{6.33\text{ kips}}$$ $$= 0.809$$ It would be acceptable to use one ¾-in.-diameter Group A slip-critical bolt at each end in standard holes with a Class A or B faying surface.

If the intermediate bolts at the one-third points only carry 13% of the total shear, it is clear that any high-strength bolt will be acceptable. Although these intermediate bolts appear to resist very little force in these calculations, they are critical in determining the overall column strength because of their impact on determining the built-up member effective length as specified in AISC *Specification* Section E6.1.

When the end connection of a built-up compression member is also required to transfer the full compressive load to the remainder of the structure, such as a double-angle compression member in a truss, the end connection may be designed to transfer the load through a bearing connection but the bolts must be pretensioned.

CONCLUSIONS

The 2016 AISC *Specification* requires that the connectors at the ends of built-up compression members be designed as welds or slip-critical bolts with Class A or B faying surfaces. However, it does not provide guidance on the required strength of those connectors. This paper provides one approach to determining the required strength of these end connectors based on the initial out-of-straightness specified in ASTM A6-14 and the second-order amplification given in AISC *Specification* Appendix 8. It further recommends that the end connectors be designed for the entire shear force, regardless of the number of intermediate connectors because these intermediate connectors take only a small portion of the total shear force.

Other assumptions may lead to different required shear strength, but because the number of required connectors is fairly small, a significant change in the number of slip-critical bolts is unlikely.

REFERENCES

AISC (2016), *Specification for Structural Steel Buildings*, ANSI/AISC 360-16, American Institute of Steel Construction, Chicago, Ill.

AISC (2017), *Steel Construction Manual*, 15th Ed., American Institute of Steel Construction, Chicago, Ill.

ASTM (2014), *Standard Specification for General Requirements for Rolled Structural Steel Bars, Plates, Shapes, and Sheet Piling*, ATSM A6/A6M-14, ASTM International, West Conshohocken, Pa.

Guide for Authors

Scope *Engineering Journal* is dedicated to the improvement and advancement of steel construction. Its pages are open to all who wish to report on new developments or techniques in steel design, research, the design and/or construction of new projects, steel fabrication methods, or new products of significance to the uses of steel in construction. Only original papers should be submitted.

General Papers intended for publication should be submitted by email Margaret Matthew, editor, at **matthew@aisc.org**.

The articles published in the *Engineering Journal* undergo peer review before publication for (1) originality of contribution; (2) technical value to the steel construction community; (3) proper credit to others working in the same area; (4) prior publication of the material; and (5) justification of the conclusion based on the report.

All papers within the scope outlined above will be reviewed by engineers selected from among AISC, industry, design firms, and universities. The standard review process includes outside review by an average of three reviewers, who are experts in their respective technical area, and volunteers in the program. Papers not accepted will not be returned to the author. Published papers become the property of the American Institute of Steel Construction and are protected by appropriate copyrights. No proofs will be sent to authors. Each author receives three copies of the issue in which his contribution appears.

Manuscripts Manuscripts must be provided in Microsoft Word format. Include a PDF with your submittal so we may verify fonts, equations and figures. View our complete author guidelines at **aisc.org/ej**.